PHOTONIC CRYSTAL CAVITY BASED OPTICAL INDUCED TRANSPARENCY

Changyu Hu

A Thesis Submitted for the Degree of PhD
at the
University of St Andrews

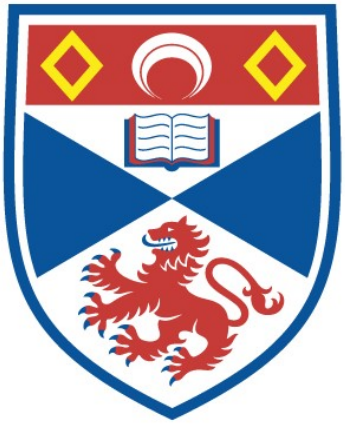

2020

Photonic crystal cavity based optical induced transparency

Changyu Hu

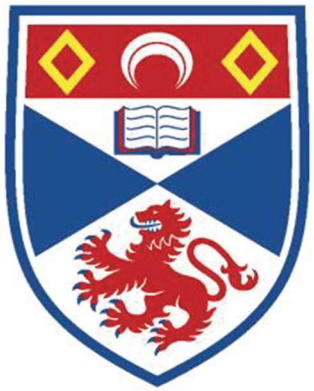

University of St Andrews

This thesis is submitted in partial fulfilment for the degree of PhD

at the

University of St Andrews

September 2018

Candidate's declaration

I, Changyu Hu, do hereby certify that this thesis, submitted for the degree of PhD, which is approximately 30,000 words in length, has been written by me, and that it is the record of work carried out by me, or principally by myself in collaboration with others as acknowledged, and that it has not been submitted in any previous application for any degree.

I was admitted as a research student at the University of St Andrews in September 2014.

I confirm that no funding was received for this work.

Date 27/08/2018 Signature of candidate

Supervisor's declaration

I hereby certify that the candidate has fulfilled the conditions of the Resolution and Regulations appropriate for the degree of PhD in the University of St Andrews and that the candidate is qualified to submit this thesis in application for that degree.

Date 27/08/2018 Signature of supervisor

Permission for publication

In submitting this thesis to the University of St Andrews we understand that we are giving permission for it to be made available for use in accordance with the regulations of the University Library for the time being in force, subject to any copyright vested in the work not being affected thereby. We also understand, unless exempt by an award of an embargo as requested below, that the title and the abstract will be published, and that a copy of the work may be made and supplied to any bona fide library or research worker, that this thesis will be electronically accessible for personal or research use and that the library has the right to migrate this thesis into new electronic forms as required to ensure continued access to the thesis.

I, Changyu Hu, confirm that my thesis does not contain any third-party material that requires copyright clearance.

The following is an agreed request by candidate and supervisor regarding the publication of this thesis:

Printed copy

No embargo on print copy.

Electronic copy

No embargo on electronic copy.

Date 27/08/2018 Signature of candidate

Date 27/08/2018 Signature of supervisor

Underpinning Research Data or Digital Outputs

Candidate's declaration

I, Changyu Hu, understand that by declaring that I have original research data or digital outputs, I should make every effort in meeting the University's and research funders' requirements on the deposit and sharing of research data or research digital outputs.

Date 27/08/2018 Signature of candidate

Permission for publication of underpinning research data or digital outputs

We understand that for any original research data or digital outputs which are deposited, we are giving permission for them to be made available for use in accordance with the requirements of the University and research funders, for the time being in force.

We also understand that the title and the description will be published, and that the underpinning research data or digital outputs will be electronically accessible for use in accordance with the license specified at the point of deposit, unless exempt by award of an embargo as requested below.

The following is an agreed request by candidate and supervisor regarding the publication of underpinning research data or digital outputs:

No embargo on underpinning research data or digital outputs.

Date 27/08/2018 Signature of candidate

Date 27/08/2018 Signature of supervisor

Acknowledgements

First of all, I would like to extend my sincere appreciation to my supervisor, Dr Liam O'Faolain (William Whelan-Curtin) for giving me the opportunity to work in his research group. He is always willing to discuss and share his idea about any research work. His passion, energy and enthusiasm inspired me for the last four years. I have learned a lot from all aspects as both a scientist and a group leader. In addition, I am highly indebted to Dr Kapil Debnath and Dr Athanasios-Alexandros Lies for sharing their technological expertise and innovative ideas and thank them for spending an enormous amount time in the lab and cleanroom with me and help me when I started my PhD study. A special thanks goes to Dr Sebastian Andreas Schulz for helping me with slow light measurement and discussions in Cork Institute of Technology. I would like to thank my colleagues and friends in the School of Physics and Astronomy of University of St Andrews for creating a pleasant working environment and helping me quickly adapt to life in St Andrews as an overseas student. I have to particularly thank everyone in the Nanophotonics and Syntheic optics groups- particularly Dr Andrea Di Falco, Dr G. R. Chinna Devarapu, and Simone Iadanza, and Praveen Singarevelu for helping me to build up the set-up measurement and life at Cork Institute of Technology. My special appreciations go to Mr Callum Smith, Mr Graeme Beaton, and Mr Chris Watson for keeping the clean room and the equipment running.

I am grateful to a number of people for their guidance and assistance during my PhD and here. I would like to take this opportunity to express my sincere gratitude to them.I would like to thank my parents for their love and support, as well as my sister and my lovely nephew.Last but not the least, a special gratitude to my wife Jieling, for encouraging me and believing me in all my life.

Publications arising from this work

Journal paper

1. **C. Hu**, S.A. Schulz, A. A Liles and L. O' Faolain, "Tunable optical buffer through an analogue to electromagnetically induced transparency in coupled photonic crystal cavities", ACS photonics, 5, 5, p. 1827-1832, 2018

2. A. P. Bakoz, A. A. Liles, A. A. Gonzale-Fernandez, T. Habruseva, **C. Hu**, E. A. Viktorov, S. P. Hegarty, L. O' Faolain, "Wavelength stability in a hybrid photonic crystal laser through controlled nonlinear absorptive heating in the reflector", Light: Science& Application, 7,7 p. 38, 2018

3. V. V. Kotlyar, A. G. Nalimov, S. S. Stafeev, **C. Hu**, L. O'Faolain, M. V. Kotlyar, D. Gibson and S. Song, " Thin high numerical aperture metalens", Optical Exprees, vol. 25, p 8158- 8167, 2017

Proceeding

1. S.A Schulz, **C. Hu**, J. Upham, R.W. Boyd, and L. O'Faolain, "Controllable low-loss slow light in photonic crystals", Steep Dispersion Engineering and Opto-Atomic Precision Metrology XI, 2018

2. **C. Hu,** A. A. Liles, S.A Schulz, and L. O' Faolain, "Tunable optical buffer through an analogue to Electro-magnetically Induced Transparency in coupled Photonic Crystal cavities", IEEE nano, 2018

3. **C. Hu** and Liam O' Faolain, "All-optical analog to electromagnetic induced transparency effects based on vertical coupling photonic crystal cavities" Group IV photonics (GEP), 2016

Conferences attended

PEIRS, 2014, Guangzhou

12th International Symposium on Photonic and Electromagnetic Crystal Structures

(PECS XII), 2016, York

IEEE 13th International Conference on Group IV Photonics (GFP), 2016, Shanghai

IEEE 18th International Conference on Nanotechnology (NANO), 2018, Cork

Abstract

Nowadays, information technology has been deeply integrated in our daily life. However, within its rapid development, it faces a serious bottleneck due to the prohibitive power consumption and limited transmission bandwidth of electrical interconnects. Silicon photonics introduces a potential solution for information technology based on optical communication. In this field, delay-bandwidth devices offer a high bandwidth optical interconnection and low power consumption for the next generation information communication technology. Through introducing the slow light effect, I can realise time domain control and store the light to achieve a new functional component, which is the optical buffer for optical information processing. The optical buffer allows us to control and store the light, using as the optical information process and transit. However, the current optical buffer devices are limited by high optical loss and the ability to produced tunable group delay of the light. In this thesis, I examine different configurations of the coupled photonic crystal resonator system and then introduce a novel tuneable delay line, based on photonic crystal cavity structures. Through the optical analog to electromagnetically induced transparency (EIT), an EIT-like transmission spectrum has been achieved in coupled photonic crystal cavities. By tuning the phase difference between two coupled resonators and resonance wavelength, I can achieve the desired analog conditions and reach to a maximum group delay of 360 ps. By adding thermal tuning pattern, I have demonstrated a tuning of the group delay of over 120 ps range at a low input power and a maximum delay of 300 ps group delay in coupled photonic crystal cavities system. All devices are with a footprint at only 200 μm^2, and with integrated compatibles as well. By employing a new vertical coupling technique, a record low loss 15 dB/ns is presented making this system very promising for practical optical information applications.

Table of Contents

Chapter 1 Introduction

1.1 Silicon photonics

Transistors [1, 2], one of the greatest inventions of the 20th century, have changed our daily life and communication technology. Microelectronic devices based on semiconductor material, have quickly occupied most of the electronic market due to their outstanding advantages, such as low power consumption, low cost, and ease of integration. Silicon microelectronics has become an important pillar of modern industry. From the invention of transistors, to the emergence of integrated circuits, and then the continuous updating of computer performance and the rapid development of communication networks, all aspects of human life have been influenced with microelectronics. Microelectronics design and production methods have been widely used in different disciplines and social fields.

In 1965, Dr Gordon Moore, the co-founder of Fairchild Semiconductor, proposed the famous "Moore's Law", which indicated that the embedded density of the integration circuit chips increases four times every three years and the size of the processing chips decreases to half every three years [3]. Microelectronics has become the fastest growing technology of past 50 years, and the number of transistors produced and used in our daily life is massive, as presented in Fig 1.1. However, further miniaturization of electronics chips, the interconnect and power consumption of integrated circuits becomes an insurmountable obstacle. Compared with electrons, photons have great advantages as information carriers, such as zero rest mass, no interference between each photon and different wavelengths of light can be used for multi-channels simultaneous communication. Therefore, information transfer using photons has broader bandwidth and greater data transmission rates [4, 5, 6]. In order to meet the technical

requirements of high-speed computer development, on-chip optoelectronics becomes a key technology that needs to be advanced urgently. Therefore, by combining microelectronics and optoelectronics, silicon optoelectronics [7-10] becomes an inevitable development by the general consensus of industry, due to an advanced mature fabrication technology, high density integration, low cost, high optical bandwidth, ultra-fast transmission rate and low crosstalk. The goal of silicon optoelectronics is to research and develop silicon-based large-scale integration technology, that combines photons and electrons as information carriers. The core content is to study "small" and "on-chip" photonic devices and integrate them with nanoelectronics devices. By using silicon or silicon compatible materials, a larger number of micro or nano scale devices based on photons and electrons can be simultaneously fabricated on the same silicon substrate to form a completely, new large-scale integrated chip.

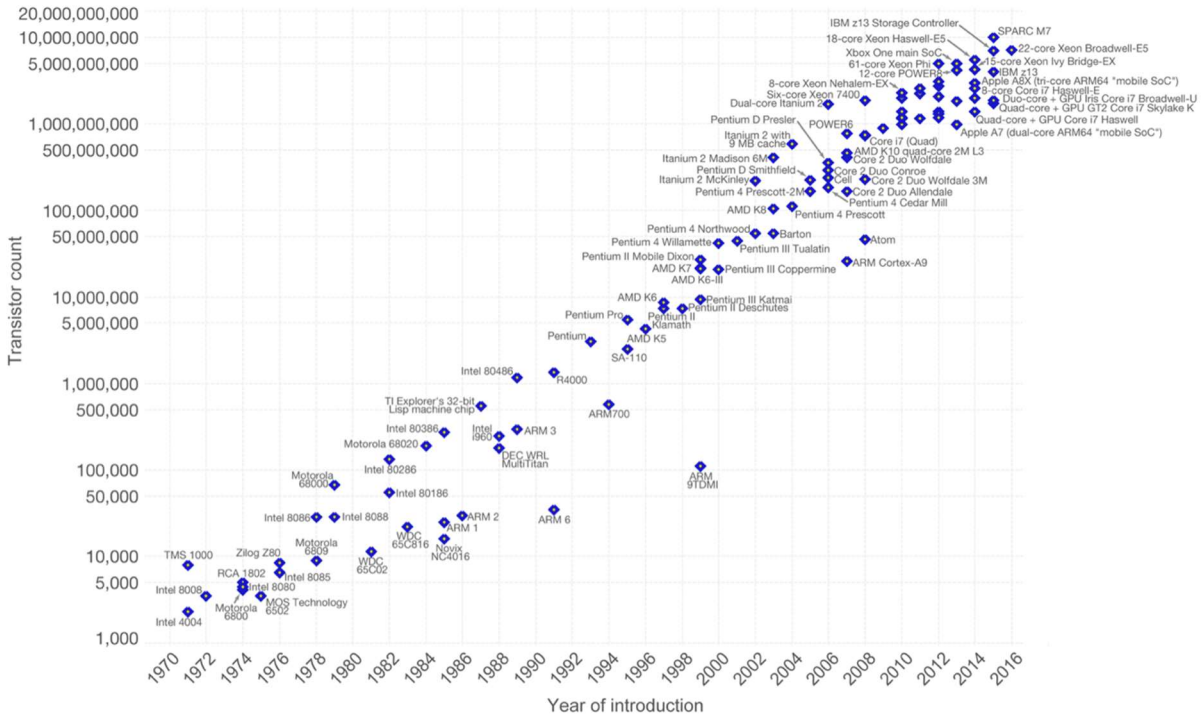

Fig 1.1 Data source from Transistor_Count of Wikipedia. The figure shows the growth of the number of the transistors since 1970, respectively.

In the study of optical communications, each milestone has depended on breakthroughs in the fundamental function devices and components. In 2004, Intel has demonstrated a high speed optical modulator based on metal-silicon substrate, with over 1 GHz modulation bandwidth [11]. In 2005, a continuous-wave Raman laser based on silicon was realised by Intel [12]. They demonstrated a stable single mode laser output with side-mode suppression over 55db and linewidth less than 80 MHz. In 2006, Brian (et al) of University of California demonstrated the first electrically pumped mode-locked laser based on silicon [13]. In 2007, Intel proposed a 40 Gbits/s transmission rate and 30 GHz bandwidth silicon optical modulator, based on the free carrier plasma dispersion [14]. In 2008, The first fully integrated 4x10 Gb/s dense wavelength division multiplexing (DWDM) optoelectronic transceiver chip was realized by a standard 130 nm complementary metal oxide semiconductor (CMOS) silicon-on-insulator (SOI) technology [15]. In 2012, Doerr et al [16] and Dong et al [17] demonstrated a monolithic 112 Gb/s quadrature phase-shift keying (QPSK) modulator based on SOI. In 2013, IBM proposed a 25 Gb/s multi-channel wavelength division multiplexing (WDM) on-chip optical transceivers based on 90 nm CMOS fabrication technology [18]. This is the first time to realize one single optical integration chip based on CMOS fabrication technology.

Despite these rapid developments of silicon photonics, there are still fundamental device constraints in optical communications. In the next generation of chip-based information networks, the ultrafast transmission speed and path switching of optical packets become two important goals [19, 20]. Meanwhile, optical information processing needs a high transmission data rate, high output and low power consumption. Thus, a core technology in optical communication is the optical delay line, reflecting the capacity to delay or advance a signal with a broad bandwidth, in other words. The delay-bandwidth products provide not only large capacity for data transmission, but also improves the ability of data connection and processing.

However, realising a tuneable long delay lines with a broad bandwidth in a small footprint remains challenging due to the existence of the fixed time-bandwidth product. Therefore, achieving slow light effect on-chip with a broad bandwidth is a key fundamental technology for delay-bandwidth products to store optical information and adjust the information processing time to improve optical information communication in the next generation information communication system. Slow light is the propagation of the light through a medium at a lower group velocity than the speed of light ($\approx 3 \times 10^8$). Slow light happens when the light is slowed down through an interaction with the medium. Slow light has been widely observed and studied in different media and structures, such as Bose-Einstein condensates [21], low-pressures metal vapors [22] and optical fibers [23, 24]. If slow light can be controlled with a faster response speed, relative to mechanical methods, it could be a solution not only for buffering but also different types of time processing, such as re-timing, performing convolution integrals and multiplexing. Further, such a tunable delay line could also improve the phase control in modulators and phased-array beam shapers. As we know, light-matter interaction is generally very weak in nonlinear optical devices, which is a fundamental obstacle for many photonic applications. Additionally, due to the strong light-matter interactions, slow light devices offer the opportunity for compressing optical signals and enhancing nonlinear processes, such as Raman scattering [25], third harmonic generation [26] and four-wave mixing [27, 28]. As the slow light effect is introduced into the system, we can control the slow light effect in different functional components. For example, we can apply slow light effect in switches, amplifiers and transistors components, and a regular transmission system for the signal transmission. In additional, the slow light effect enables the reduction in the size of photonic circuits and components [29]. Driven by the above goals, slow light devices are important components for next generation information communication and on-chip photonic circuit.

1.2 Slow light in photonic crystal cavities structures

In 1998, L. V. Hau et al demonstrated slow light in ultracold atom system by using quantum interference effect [26], which the light was slowed down to 17 m/s. Later, L.V. Hau and her colleagues succeeded in stopping and storing light in Bose-Einstein condensates and retrieved the information light from a different condensate [30]. The revived light pulse recorded the pervious amplitude and phase information, which can be used in quantum information processing and wavefunction sculpting applications. Even though these technologies can achieve huge group delay of light, up to 17 m/s, the narrow operational bandwidth and the strict experiment environment limit further applications. In last 20 years, slow light has also been demonstrated in photonic crystal structures [31-35], which offers a promising approach for the on-chip integration of optical communication devices. Photonic crystals are multidimensional periodic structures that can confine light using the photonic band gap. Since the 1980s, photonic crystals have been widely explored for various optical communication applications [36-40]. Localized defect effects have been one subject of tremendous research interest in many photonic crystal structure, especially as photonic crystal cavities (point defect) [41-49] and photonic crystal waveguides (line defect) [50-60]. When light propagates through the defects, it is confined in the defect region due to Bragg reflection in the lateral direction and total internal reflection in the vertical direction. For example, in Fig 1.2, the light pulse injected into the input waveguide and propagates through an ultrahigh quality factor photonic crystal cavity (the quality factor is around 7.4×10^5). The light pulse gets coupled into the cavity and released into the output waveguide. The temporal response of the light was measured from the output waveguide. 1.45 ns of group delay had been observed, compared with the reference waveguide, as in Fig 1.2 (b).

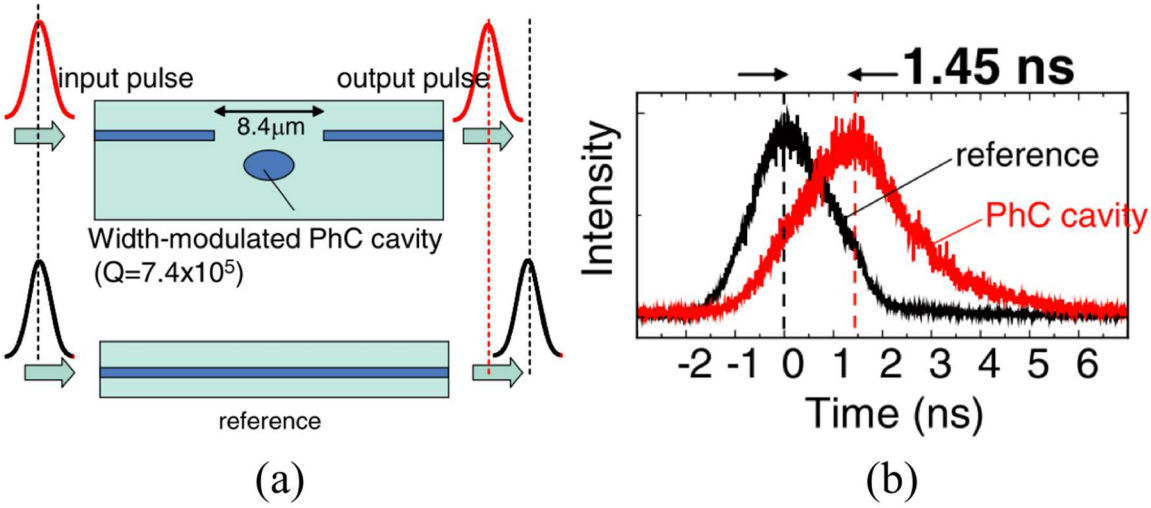

Fig 1.2 Figures from Ref [45]. (a) Schematic of light propagation via a photonic crystal cavity and a reference waveguide, respectively. (b) Time-resolved light intensity from the output waveguide with an ultrahigh quality factor cavity and a reference waveguide.

In this case, the important thing is that slow light has been achieved in a very short physical length using the photonic crystal structure and measured at room temperature. However, the slow light effect in a single cavity has fundamental limitations for practical applications. This is because the maximum delay is restricted by the quality factor of the cavity, and the bandwidth of an optical pulse is also limited by the cavity resonance bandwidth. To overcome this limitation, employing multiple coupled resonators can be employed to realise a broader bandwidth slow light device. However, it is a challenging task to fabricate large-scale arrays of high-quality factor cavities at the nano-scale.

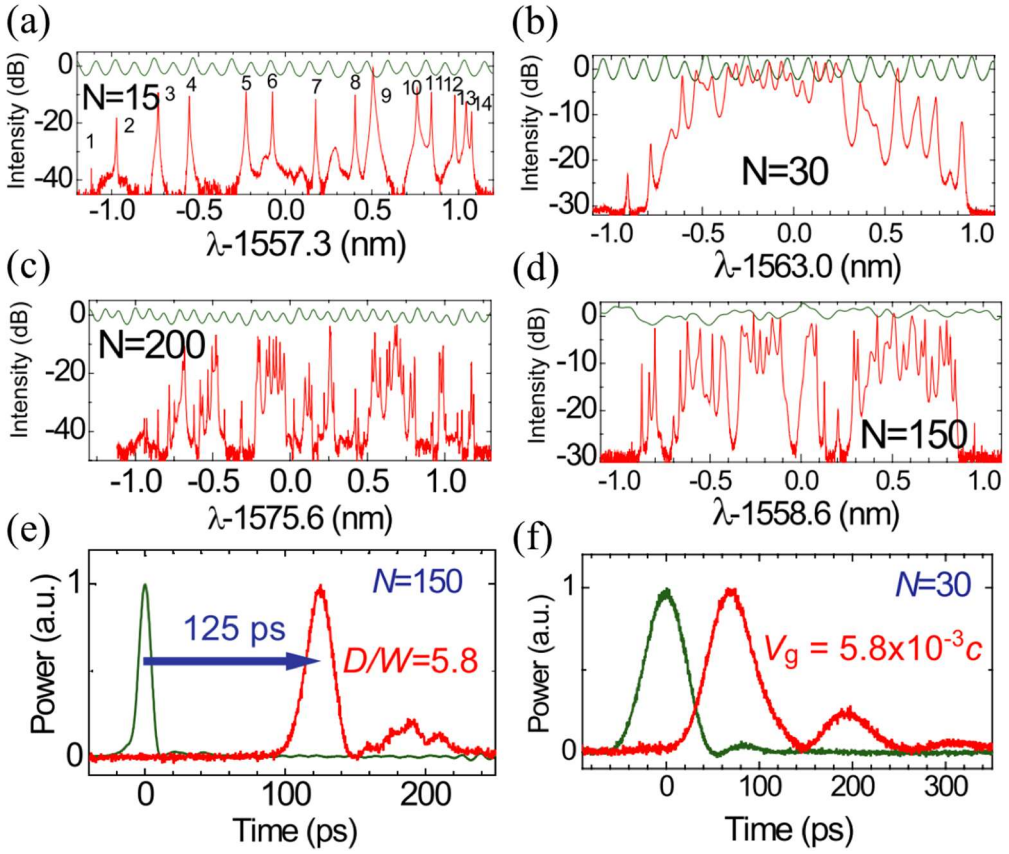

Fig 1.3 Figures from Ref [65]. (a)-(d) Transmission spectrum for different number arrays of coupled photonic crystal cavities. (a) N=15, (b) N=30, (c) N=200, (d) N=150. (e) Time-resolved light pulse intensity for N=150 device and the delay verse plus width is shown. (f) Time-resolved light pulse intensity for N=30 device and the group velocity are shown.

Numbers of studies have realized slow light in this type structure, such as multilayer stacks, microsphere arrays, polymer coupled rings, silicon coupled rings and photonic crystal coupled cavities [61-71]. However, due to insufficient quality factors and a large device sizes, slow light performance is limited. In Fig. 1.3, different large array (N=15, 30, 150, 200) of photonic crystal cavities has been fabricated and measured [65]. A larger group delay has been observed, when compared with a single cavity structure, as shown in Fig 1.3 (e) and (f). However, when the number of coupled cavities was increased, the transmission loss massively increased. The coupling loss will become substantial when slow light occurs, and light is stored in the

waveguide. This is because the impedance mismatch between slow light waveguide and conventional waveguide, which is inversely proportional to the group velocity. Meanwhile, due to the cavity size fluctuation, finite disorder in periodic systems leads to localized states and results in an increasing propagation loss. Those issues will become an obstacle when a slower group velocity is needed in practical applications.

1.3 Slow light in photonic crystal waveguide structure

As we known, the photonic crystal can be considered as a perfect photonic insulator, due to the photonic band gap. Much important information that can be inferred from the band diagram, in particular is the group velocity v_g of light. The group velocity is given by the slope of the ω-k dispersion curve:

$$v_g = \frac{\partial \omega}{\partial k} \tag{1.1}$$

which is also can be expressed by the group index,

$$v_g = \frac{c}{n_g} \tag{1.2}$$

which can be seen from Fig 1.4 (a). The group velocity v_g of these modes approaches to zero, when the bands flatten as they approach the band edge. Thus, due to the photonic band edge, slow light can also be realized in photonic crystal waveguide structures [72-85]. The two important properties of slow light photonic crystal devices are the frequency bandwidth and high-order dispersion. By optimizing and engineering the PhC waveguide [86-92] dispersion, a broad operation bandwidth and flexible operation wavelength are achieved. A flattened dispersion curve has been shown in Fig 1.4 in a modified slow light photonic crystal waveguide

[92]. A maximum group index ~93 can be obtained to achieve slow light effect in the modified photonic crystal waveguide structure [92]

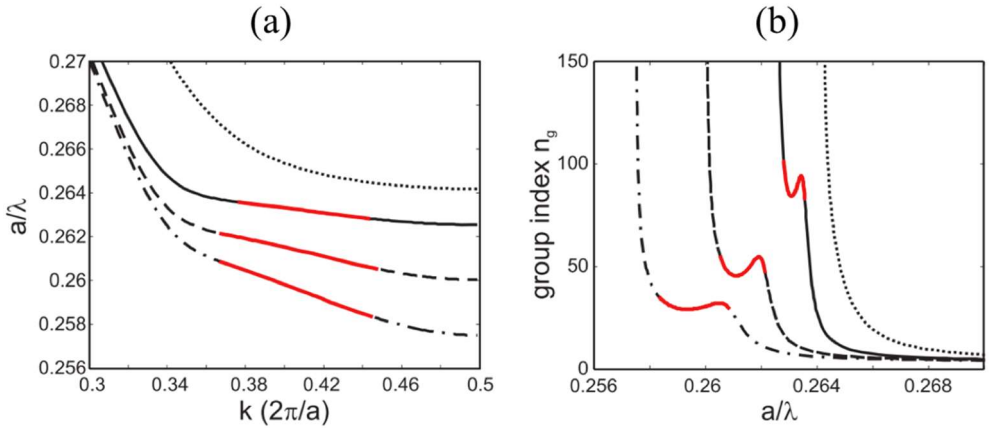

Fig 1.4 Figures from Ref [92]. (a) calculated dispersion curves and (b) group indices for three different photonic crystal design, respectively. The thick red line represents the slow light regions.

However, the band-edge is not the best operating region, as the band structure near the band edge is parabolic and the group velocity changes rapidly within changing frequencies, thus the narrow bandwidth of slow light will decay in a short time. Furthermore, from an engineered point view, a lossy propagation mode is caused by any fabrication tolerance. The engineered slow light photonic crystal waveguides were studied to overcome those concerns, for instance, by chirping the waveguide properties [94], changing the waveguide width [95, 96], or the position [97] and size hole [98] of the photonic lattice adjacent to the line defect waveguide. the modes at frequencies inside the PBG can be separated by their lateral symmetry of magnetic field (with respect to a plane along the propagation direction and vertical to the slab) to even and odd modes. The even mode of such waveguides can be categorized with respect to their field distribution as “index guided” or “gap guided”. An index guided mode has its energy concentrated inside the defect and interacts only with the first row of holes adjacent to the defect. Its behavior can be simply represented by a dielectric waveguide with periodical

corrugation. However, a gap guided mode interacts with several rows of holes, thus it is dependent on the symmetry of the PC and its PBG. Most of these slow light waveguide configurations operate by manipulating the gap-guided mode with respect to the index-guided mode, except the chirping waveguide. Due to the refractive index difference between the waveguide and the surrounding lattice, the even guided mode contains these two types, resulting from an anti-crossing between a gap-guided mode and a folded index-guided mode as shown in Fig. 1.5. The waveguide mode is determined by the interaction between the gap-guided mode with the index-guide mode, which mainly affected by the first and second row holes.

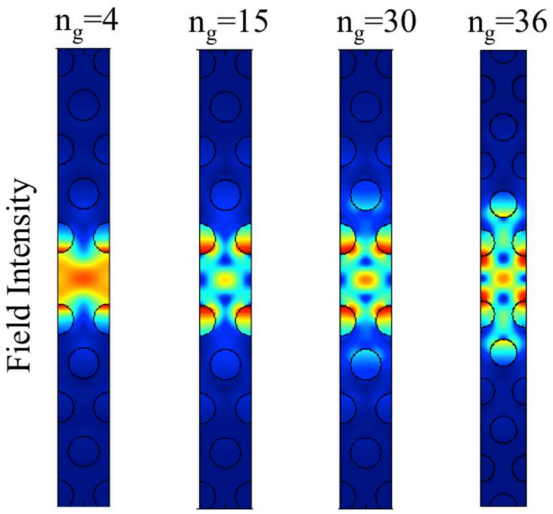

Fig 1.5 Field intensity with respectively group indices are shown, which are calculated in the eigenfrequency module in Comsol. The filed distribution shows the interaction between a gap-guided mode and a folded index-guided mode

After understanding this, it provides a flexible operation space on the dispersion curve and achieves a region with an almost linear dispersion curve with low slope, known as a flat band slow light region. For instance, the interaction of the two modes distorts each other when the corresponding bands approaches to the band of the topmost lattice mode. Shifting the

dispersion curve of the waveguide down in the band structures by changing the waveguide width, due to the increased effective mode index of the defect mode. Thus, a flat region of constant slope can be obtained, which provides a board operation bandwidth for slow light. As presented in Fig. 1.6, shifting the first row of holes outwards (S_1 negative) and the second-row inwards (S_2 positive) makes the anti-crossing happens in a lower frequency region, and achieve a larger flat band slow light region, in which the group index is high and almost constant.

A low group velocity dispersion of flat band slow region, with a high group index, is generally regarded as an advantage of slow light waveguides with respect to optical cavities [97] and allows the device to be less influenced by temperature and fabrication fluctuations. A broad useful bandwidth with lower group indices is shown in Fig. 1.6.

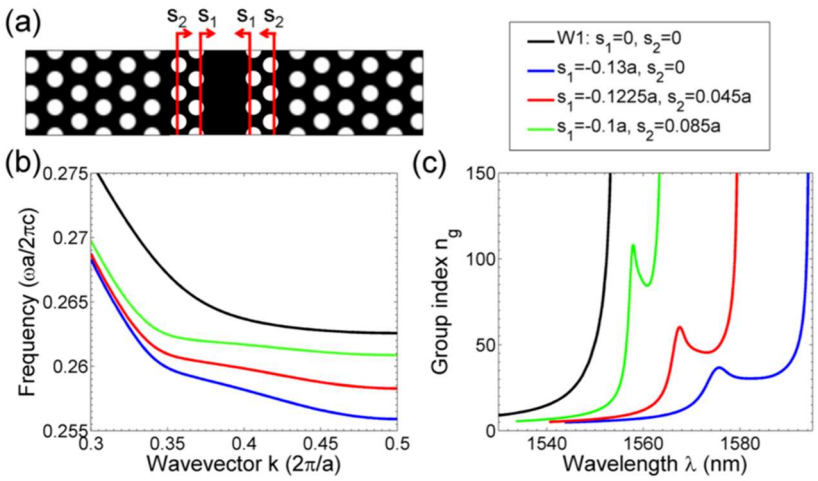

Fig 1.6 Engineered slow light waveguide (Pictures take from Ref. [97]). (a) Schematic design of optical engineered W1 photonic crystal waveguide: the first and the second rows of holes are modified symmetrically about the waveguide axis. The displacements are represented as s1 and s2, where move to the waveguide center is defined to the positive value. (b) the dispersion curves and (c) group indices for t optical engineered W1 photonic crystal waveguide. The mode of an unmodified W1 photonic crystal waveguide (black) is also included for a comparison.

Photonic crystal line defect waveguides can provide a powerful platform for this study and exploitation of slow light effects. Meanwhile, the optimized engineered waveguide offers a large operation bandwidth and flexibility operation wavelength. A lot of possibilities to tune the slow light properties changing the size of hole, the bandwidth of waveguide, and the lattice constant, such as bandwidth and slow factor. The disadvantage of the photonic crystal waveguide approach is that tuning of the slow factor and high propagation loss remain a challenge, comparing with coupled resonators system, which will be discussed in the following section.

1.4 Slow light in optical analog electromagnetically induced transparency system

In the previous section, slow light has been achieved through photonic crystal cavity or photonic crystal waveguide. By adjusting the geometric parameters, such as shifting the position, size of the hole and the lattice constant, we can achieve high Q-mode to trap light pulses as a slow light component. The inspiration of coupled resonators system to achieve slow light is based on previous researches on slow light in atomic gases using electromagnetically induced transparency (EIT) [21], in which light is captured in dark states of the atomic system via adiabatic tuning [22]. Classical analogs of EIT have already been demonstrated in both mechanical and electrical oscillators system, where the quantum destructive interference between excitation pathways from the lower level to the upper level in three-level systems, as shown in Fig 1.7. In 1999, L. Hau et al experimentally demonstrated in an ultracold gas of sodium atom, that optical pulses can be slowed down to 17 m/s due to the quantum interference effects. They firstly cooled the atom to the transition temperature into Bose-Einstein condensation. Then, a probe laser was applied to tune the atom states from $|1\rangle \rightarrow |3\rangle$,

which $|1\rangle$ is the ground state. Later, a coupling pump laser was applied to tune the transition from the unpopulated states $|2\rangle \rightarrow |3\rangle$. Thus, the quantum interference occurred in between $|2\rangle$ and $|3\rangle$, and generated a new transition state in the system, as shown in Fig 1.7 (b). Due to a small doppler broadening of the two transition states $|2\rangle \rightarrow |3\rangle$, the system presented a transparency peak with a smaller bandwidth, compared to the $|1\rangle \rightarrow |3\rangle$, and huge slow light delay observed in the system.

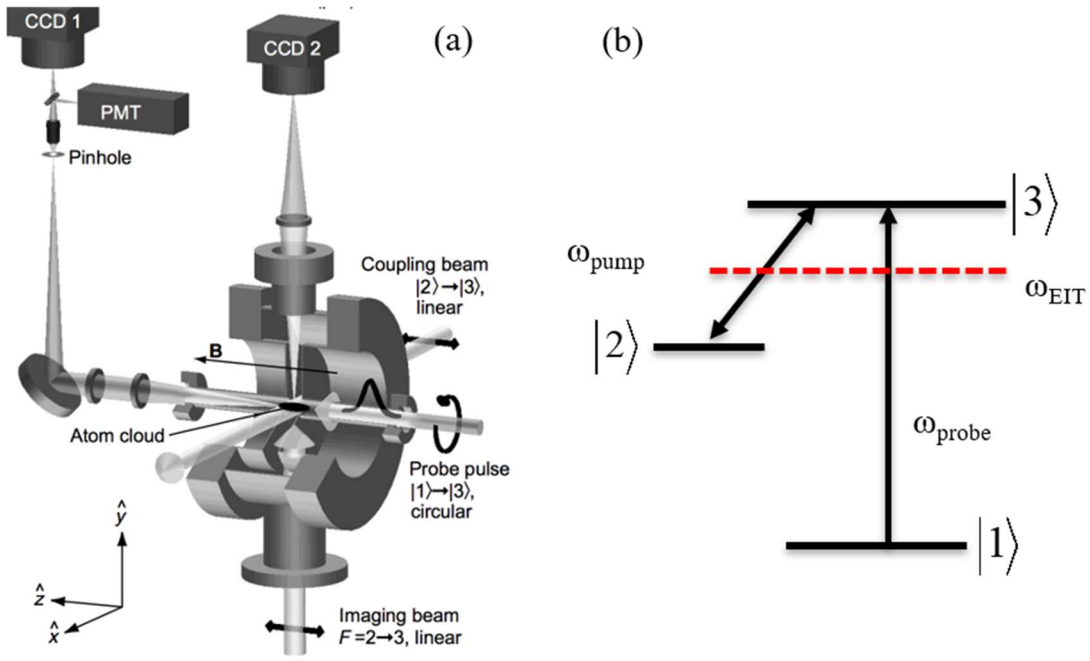

Fig 1.7 Figures reproduced from Ref [22] (a) A experiment set-up to realize electromagnetically induced transparency in ultracold atom gas system. (b) Schematic diagram of quantum interference effect in three energy levels of the same system in (a).

However, the operating bandwidth was very narrow and only certain wavelengths, for which there are suitable atomic resonances, can be used in atomic system limiting the potential applications Since the EIT phenomenon appears when resonators interference between excitation pathways, it has been recently numerical analyzed and experimental realized using

optical resonators. Resonant dynamic control using the photonic crystal through the localized defect mode has been theoretical analyzed [98, 99]. Additionally, a channel add-drop filter based on multiple coupled cavities systems in a photonic crystal was studied to achieve light trapping [100, 101]. Under specific symmetry and degeneracy phase conditions, optical signals can be completely transferred from one waveguide to another one as a time delay system. A theoretical coupled resonators system [99] has been studied to achieve a large delay-bandwidth and zero group velocity of the optical pulse. In the past few years, an optical analog to EIT system has been proposed and experimentally realized using in in-plane coupling photonic crystal structure [102] and ring resonators [103] and gain a great interest for next-generation on-chip optical communication.

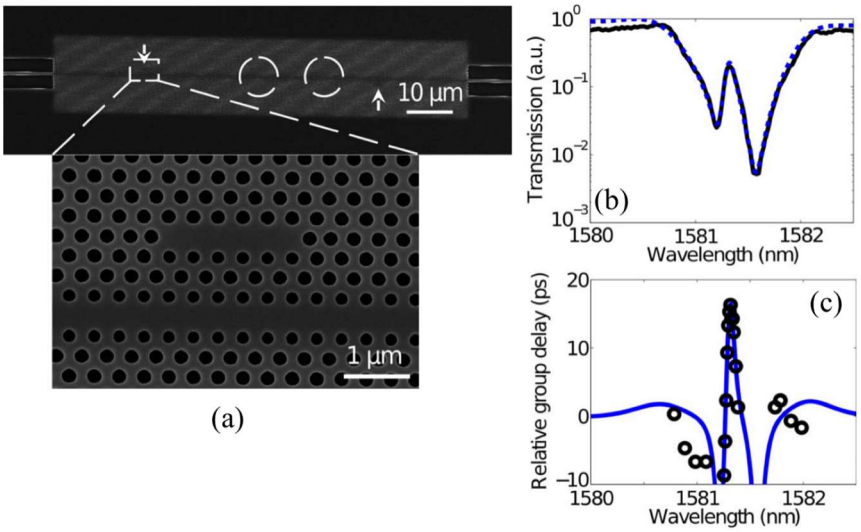

Fig 1.8 Figure reproduced from Ref [102]. (a) a SEM image of in-plane coupling system to realize the optical analog to EIT system. Two coupled Ln defect cavities are siding coupling to a photonic crystal waveguide. (b) the experimental EIT-like transmission spectrum has been presented within a theoretical fitting (black dashed curve). (c) the corresponding group delay has been measured with a theoretical fitting (black dots).

For example, in 2011, Y. Huo et al demonstrated optical analog to EIT system by using Ln defect cavity in in-plane coupling system [102], as shown in Fig 1.8. Two Ln cavities are coupled each other through a photonic crystal waveguide, as presented in Fig 1.8 (a). By achieving phase difference between two coupled cavities, engineered design can achieve EIT-like transmission spectrum in this device as shown in Fig 1.8 (b), and they also demonstrated that the device can realize a tuning of the group delay from 5 ps to 16 ps. When the device reaches the maximum 16 ps, the device presents over a bandwidth of 20 GHz. The group delay can be tuned by controlling the propagation phase of the waveguide or the resonator frequency through thermal optic tuning. A 532 nm green laser is applied to achieve thermal optical tuning.

Another experimental demonstration of the optical analog to EIT system was developed in the coupled ring resonators structure [103]. By changing the distance between two ring resonators, the EIT-like transmission spectrum can be observed in this system, as shown in Fig 1.9. From Fig 1.9 (c), the EIT-like peak is determined by the propagating phase between two ring resonators. Moreover, a top-view image of the optical modes at the EIT-like transparency resonance is shown in Fig 1.9 (b). A clear optical excitation of both rings can be seen, which indicates a strong coupling between two cavities, as well as a constructive interference in the waveguide, which indicates a strong slow light effect happened in the system. High quality factor cavities in coupled resonators system enables to an optical analog EIT system to achieve bigger group delay, compared with other couple resonators system, as it increases the effective reflectivity of each ring.

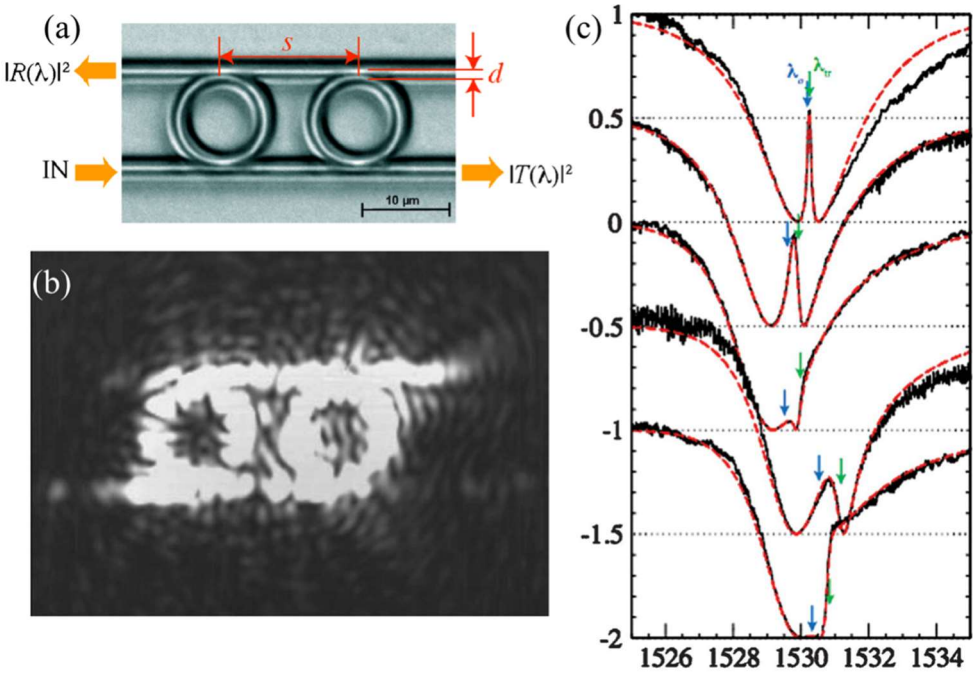

Fig 1.9 Figure reproduced from Ref [103]. (a) a microscope picture of two ring resonator, with a varying distance s. (b) a top-view camera collected image of optical mode at the EIT-like transparency resonance wavelength (c) the experimental EIT-like transmission spectrum has been presented within a theoretical fitting (black dashed curve).

1.5 Aim of the thesis

In the previous section, I have introduced different methods to achieve slow light in photonic crystal structures. The photonic crystal waveguide can provide a wider bandwidth slow light, compared with a single photonic crystal cavity structure, however v_g can achieve to only ~c/20 to c/40. The cavity-based photonic crystal structure has already demonstrated a v_g value lower than c/100 but with a limited bandwidth. In order to improve the fundamental limitation of a single cavity system, coupled resonator system is introduced, however, it brings a higher propagation loss and coupling loss, also a larger-scale device size into the system. However, a good delay-bandwidth device should have not only a large delay, but also a broad bandwidth with low insertion loss. In order to overcome these obstacles, in this thesis, I will demonstrate

a new slow light system [99, 100, 104] by analog EIT system in coupled photonic crystal cavities [105] through vertical coupling technique [106, 107]. Besides, designs to slow light and the fundamental limits on the storage of light will be studied. A conceptual design of the proposed system is shown in Fig 1.10.

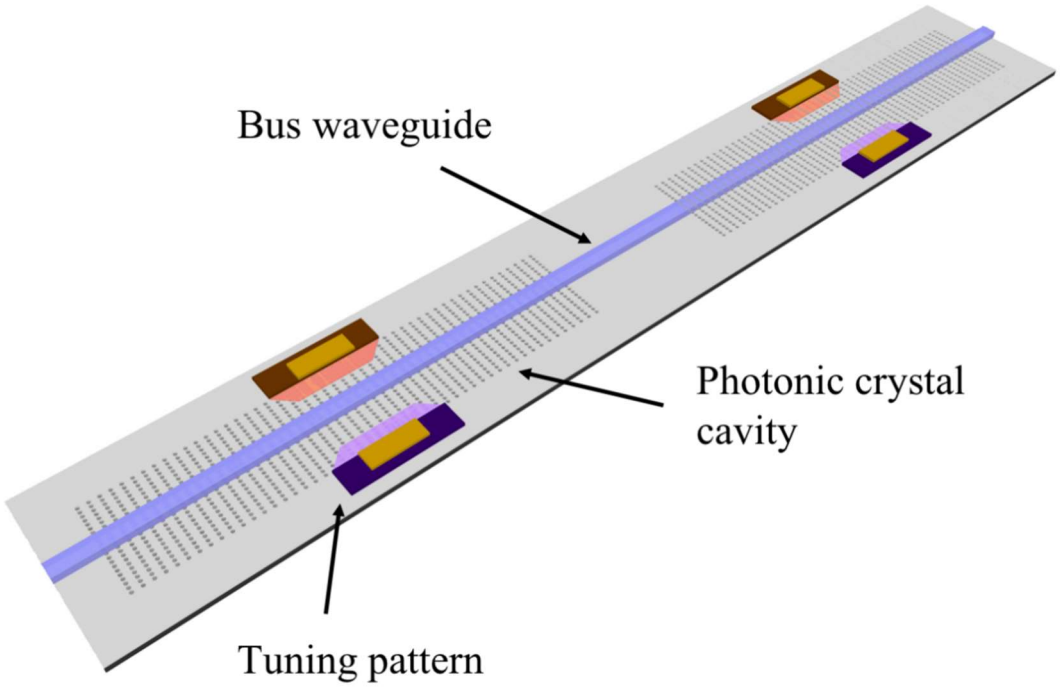

Fig 1.10 A schematic of optic analog to EIT system in coupled photonic crystal cavities with a bus waveguide and tuning patterns, such as ohimic heating pattern and p-n junctions.

The system is based on an optical analog to electromagnetically induced transparency (EIT) [93, 94, 95]. Through the all optical analog to EIT, I will achieve a better delay-bandwidth device, compared with a single cavity and coupled cavities system. Additionally, this design has a smaller geometric size and good CMOS integration properties when compared with other coupled cavities system. Moreover, due to our unique vertical coupling scheme, a low propagation loss can be obtained in the connecting waveguide, which helps reduce the overall

loss of the system. Furthermore, by applying tuning mechanisms, such as micro-heaters and P-N junctions, I can control the propagation phase and the resonance wavelength of coupled cavities to tune the slow light performance.

1.6 Thesis content

This thesis is organized as follows: Chapter 2 gives an overview on the theory of photonic crystal and photonic crystal structures. The vertical coupling system and oxide-cladding photonic crystal cavity are introduced as the fundamental components to realize the optical analog to EIT in coupled photonic crystal cavities system. In addition, the concept of EIT for slow light will be introduced. Chapter 3 gives a brief description of fabrication tools and techniques used in this thesis. In Chapter 4, I will discuss different configurations of coupled resonators to realize slow light. Theoretical demonstration of all optical analog to EIT system in coupled resonators will be presented. In chapter 5, two methods to achieve optical analog to EIT system in photonic crystal cavities have been demonstrated. The performance of slow light system will be explored. Finally, chapter 6 will give a brief summary of this thesis and further work.

Chapter 2 Background

2.1 Introduction

Photonic crystals emerged in the past few decades and are an exciting tool to control light in an integrated format. The initial purpose of promoting photonic crystals was to control the spontaneous emission of the light emission and investigate Anderson localisation in disordered crystals respectively[108-110]. The existence of 3D photonic band gap has been demonstrated theoretically [111], and many theoretical concepts were demonstrated at microwave frequencies in the 1990s. Photonic crystals were realized at optical frequencies by using semiconductor nanofabrication technologies [112]. Since then, the photonic crystal research field has been explored and expanded continuously. Several reviews are available that cover the entire history of the photonic crystal research [113-114]. The rapid research development of photonic crystals then led to innovations in light-matter interaction, in fields such as optical communication [115,116,117], optical signal processing [118,119] and quantum computing [120-128]. One of the most promising features enabled by photonic crystals is slow light [129-133], which promotes a stronger light-matter interaction and offers additional possibilities to control optical communication and to temporarily store light for optical memories [30, 31]. The field of slow light studies has developed from a fundamental science to one in which there are numerous potential applications. Some of these have been made possible with rapid development of the technologies required for practical implementation of slow light. This chapter gives some fundamental concepts of photonic crystals in general and different defect configurations in photonic crystal structures that provide the platform that the following chapters are based on.

Then I will focus on the realisation of slow light in photonic crystal structures, i.e. waveguides and coupled resonator systems. Further, I will introduce the electromagnetically induced transparency (EIT) system and discuss general configurations for all optical analog to EIT system, including ring resonators and photonic crystal cavities.

2.2 Photonic crystal

2.2.1 Photonic band gap in photonic crystal structure

The dynamics of electromagnetic fields are governed by Maxwell's equations, which in a dielectric medium with dielectric function $\varepsilon(\mathbf{r})$ can be solved to determine the electric ($\boldsymbol{E}$) and magnetic ($\boldsymbol{H}$) field respectively. In general, both $\boldsymbol{E}$ and $\boldsymbol{H}$ are complicated functions in both time and space. Due to the linearity of Maxwell's equation [36], the time dependence can be separated from the space dependence by expanding the fields into a set of harmonic modes. i.e. as a spatial mode profile with a complex exponential:

$$\boldsymbol{E}(\boldsymbol{r},t) = \boldsymbol{E}(\boldsymbol{r})e^{-i\omega t} \tag{2.1}$$

$$\boldsymbol{H}(\boldsymbol{r},t) = \boldsymbol{H}(\boldsymbol{r})e^{-i\omega t} \tag{2.2}$$

with ω the angular frequency. In order to find the governing modes by the equations at a given frequency, based on the boundary condition, the two divergence equations are given:

$$\nabla \cdot \boldsymbol{H}(\boldsymbol{r}) = 0 \qquad \nabla \times \mathbf{E}(\mathbf{r}) - \mathrm{i}\omega\mu_0\boldsymbol{H}(\boldsymbol{r}) = 0 \tag{2.3}$$

$$\nabla \cdot [\varepsilon(\boldsymbol{r})\boldsymbol{E}(\boldsymbol{r})] = 0 \qquad \nabla \times \mathbf{H}(\mathbf{r}) + \mathrm{i}\varepsilon\varepsilon(\mathbf{r})\boldsymbol{E}(\boldsymbol{r}) = 0 \tag{2.4}$$

where ε_0 and μ_0 is the vacuum permittivity and permeability, respectively. Then when $\boldsymbol{E}(\boldsymbol{r})$ is eliminated the equation for $\boldsymbol{H}(\boldsymbol{r})$ becomes:

$$\nabla \times \left(\frac{1}{\varepsilon(\boldsymbol{r})} \nabla \times \boldsymbol{H}(\boldsymbol{r}) \right) - \left(\frac{\omega}{c} \right)^2 \boldsymbol{H}(\boldsymbol{r}) = 0 \qquad 2.5$$

From Eq. 2.5, for a given $\varepsilon(\boldsymbol{r})$, I just need to solve the mode $\boldsymbol{H}(\boldsymbol{r})$ with the corresponding frequency, which can be treated as a typical series of eigenvalue problem.

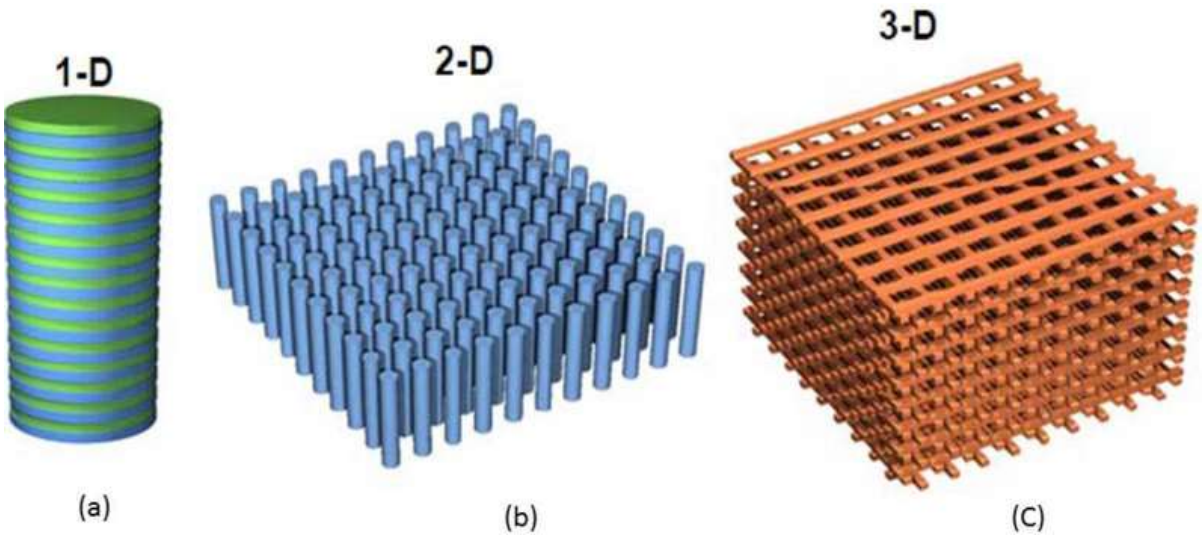

Fig 2.1 Figures from ref [36]. Schematics of (a) one-, (b) two-, and (c) three-dimensional crystals. (a) a multilayer film; (b) a square lattice of dielectric rods; (c) a woodpile crystal

Photonic crystals are characterized by discrete periodic changes of ε(r) in one, two or three dimensions, as illustrated in Fig. 2.1. The method acts on photons which is analogous to the way in which an atomic crystalline potential act on electrons: the discrete periodicity of $\varepsilon(\mathbf{r})$ in one direction results in a dependence of $\boldsymbol{H}(\boldsymbol{r})$ in that direction that is a plane wave modulated with a function $\boldsymbol{u_k}(\boldsymbol{r})$ that has the periodicity of the lattice:

$$\boldsymbol{H_r}(\boldsymbol{k}) = e^{i(\boldsymbol{k}\cdot\boldsymbol{r})} \times \boldsymbol{u_k}(\boldsymbol{r}) \qquad 2.6$$

where $\boldsymbol{k}$ is the wavevector. In solid-state physics, Eq. 2.6 is known as a Bloch state [36]. For each respective $\boldsymbol{k}$, there has a corresponding band index n in a series of eigenmodes with

discretely spaced frequencies. The band diagram or dispersion curve can be calculated, as each $\omega_n(\boldsymbol{k})$ changes continuously with $\boldsymbol{k}$. In fact, a limited region only needs to be considered, known as the first Brillouin Zone. For example, in Fig. 2(b), the first Brillouin zone of a hexagonal lattice is shown between the red dashed lines area. Studying the band structure of photonic crystals explains us how the structure confines and transports light in the corresponding frequency region.

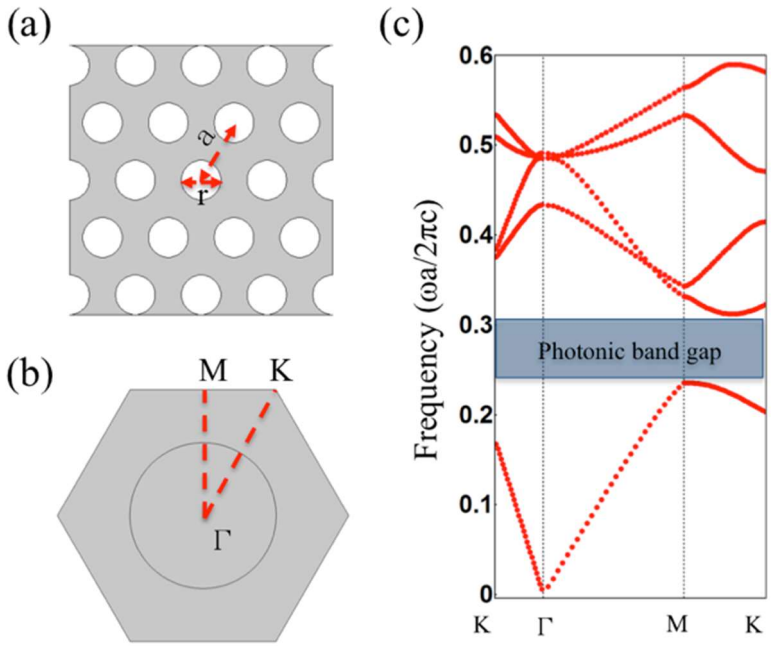

Fig 2.2 (a) a plan view for a triangle lattice of air holes in Silicon (n =3.47), with period (a) is 420 nm, and radius (r) is 0.29*a. (b) shows the first Brillouin zone, with the irreducible Brillouin zone highlighted in red dashed line area. (c) presents two-dimensional photonic band structure of TE mode for the triangle lattice. The blue dark area shows the photonic band gap.

In practice, the band structure is calculated numerically through the eigenfrequency module of COMSOL simulation software. The eigenfrequency problem therefore turns into a set of linear equations about Fourier coefficients, which are solved with an iterative method. Using the

eigenfrequency calculation module of COMSOL, I started with the eigenfrequencies at $\boldsymbol{k} = 0$ and used them as the initial inputs to iteratively compute the eigenmodes for small increments of $\boldsymbol{k}$. An example of photonic band diagram calculated with COMSOL is illustrated in Fig. 2.2, representing a two-dimensional triangular lattice photonic crystal structure. Fig 2.2 (c) represents the transverse electric polarization (TE), i.e. with the electric field confined to the plane of symmetry and the magnetic field normal to the plane. As shown in Fig. 2.2 (c), the TE polarization band diagram of triangular lattice crystal is characterized with a frequency region in which no mode can propagate through, in which the density of states is zero. This region of forbidden frequencies is called a photonic band gap, in analogy to electronics band gap in solid-state physics [134].

2.2.2 Localization light using defects

In the previous section, I saw that for the TE polarization I can achieve a complete photonic band gap using a triangular lattice structure. There is no mode allowed to propagate in any direction in the x-y plane and density of states is zero in the band gap region. In conventional insulators or semiconductors, it is well known that defects (such as vacancies, impurity doping, dislocations and stacking faults) in a periodic lattice create additional electronic states within the electronic band gap [27]. Similarly, by introducing defects into a photonic crystal structure we can create new photonic states within the band gap region. By perturbing the symmetry of a photonic crystal structure, such as by removing a hole from a triangular lattice (point defect), a localized mode can be created inside the frequency region of the forbidden gap of the photonic crystal. As the localized mode frequency falls within the band gap, the related photonic mode cannot propagate in the rest of the crystal. Thus, the physical defect spatially defines the localized mode and the mode decays exponentially away from the defect. The

boundaries around the defect act as totally reflecting mirrors for the defect mode and the structure of the defect behave as a well-confined optical cavity, from which light cannot escape. Fig 2.3 (a) shows the band structure of a triangular lattice after the introduction of the point defect. Without the defect, a complete band gap is present in the frequency range of $0.25<a/\lambda<0.3$ for TE polarization, as shown by the green curves. After creating a point defect in the middle, as presented in Fig 2.3 (b), an optical mode appears inside the band gap frequency region. This suggests the light will confine in the cavity and cannot propagate in any direction. The optical mode will be forced to localize in the cavity, as shown in Fig 2.3 (c).

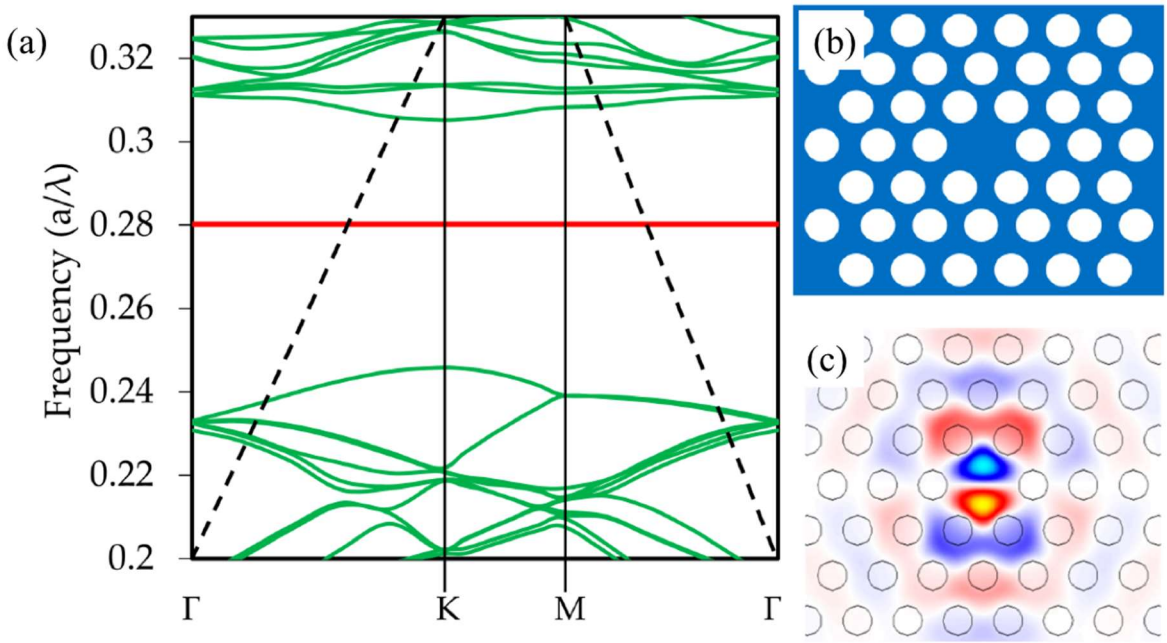

Fig 2.3 Figures from ref [36] (a) a new photonic state is located at the photonic band gap after the introduction of the defect. The bands of the perfect lattice are shown in green and the corresponding defect mode is shown in red. The light lines are presented in dashed curves, as the boundary between bound modes and radiation modes in a three-dimensional structure. (b) a point defect is introduced by removing a hole from a two-dimensional triangular lattice structure. (c) the related optical mode is shown by Rsoft software simulation. The defect cavity has three trivial degenerate modes, due to the three symmetry axes of the triangular lattice.

So far, I have introduced the point defect in two-dimensional photonic crystal structure, which achieve light confinement in the photonic crystal structure. It is important to note that this photonic band gap reflection can be perfect, as compared to plasma reflections which are typically in the 95-98% range. In addition, due to the definition of photonic band gap, this confinement method is fundamentally different from total internal reflection (TIR). Total internal reflection occurs when a plane wave is incident on a medium boundary at an angle larger than a particular critical angle with respect to the normal to the surface. TIR can exhibit perfect reflection theoretically, but satisfied only within certain limited propagation angles, which means TIR can works only in a limited range of the *k*-space region. However, when the cavity size is small enough that is comparable with the optical wavelength, the *k*-space becomes comparable to the amplitude of the wavevector of light itself. This makes it difficult to apply TIR to wavelength-size cavities. In order to achieve high Q/V (V is the cavity mode volume) value cavities, diverse kinds of defect modes based on photonic band gap method have been studied. In general, defect in photonic crystal structure can be divided into point defect and line defect. The point defect acts as a high quality factor cavity, and strongly confine the light in the structure. The line defect behaves as a thin waveguide, which can bring us a board operation wavelength range to achieve light-mattering interaction. In the next section, I will discussion several different kinds of high quality factor photonic crystal cavity based on both point and line defect configurations.

2.3 High quality factor photonic crystal cavity

2.3.1 Gentle mode confinement principle

As mentioned in Section 2.2.2, optical modes can theoretically be omnidirections confined and localized by the defect method, due to the photonic band gap. In other words, the defect localizes larger number of plane waves, which appears as a broad distribution in *k*-space. Thus, the general rule to design a high quality factor cavity is to keep the plane wave components out of the defect.

Considering a cavity of a dielectric material in the x-y plane, the cavity stands between two perfect mirrors which can confine light in the x-direction. And along the y-direction, light is confined due to the refractive index contrast, as shown in Fig 2.4 (a). Assuming the dielectric material with refractive index n_{clad}, and the vertical component of wave vector i.e, k_z is imaginary outside the structure, the optical components can be confined when

$$k_{in-plane} = \sqrt{k_x^2 + k_y^2} > n_{clad}\omega/c \qquad 2.7$$

This condition is shown as the dashed line in Fig 2.3(a), which is also called the light line. It indicates that the modes inside the light line are able to radiate into the surrounding structure and the modes outside the light line can be guided in the structure. According to Eq. 2.7, if I have a tangential component of the wave vector k_x, of any plane waves, such that $0 < k_x < n_{clad}\omega/c$), the wave can escape into the surroundings, due to weak confinement. In Fig 2.4 (b) and (d), the blue area indicates the leaky region. The electric field distribution of the cavity can be described as a unit of the fundamental sinusoidal wave with resonance frequency ω_0 and an envelope function $F(x)$ which is determined by the structure of the cavity. In this configuration,

in Fig 2.4(a), the envelope function is related to a unit rectangular function. Thus, the Fourier transform of the electric field is a superposition of two sinc function at $k_x = \pm n_{mode}\omega_0/c$. In Fig 2.4(b), large radiation loss occurs even though the high intensity plane wave component is outside the leaky region. This is due to the abrupt change of the envelope function at the boundary of the cavity. Therefore, in order to prevent the radiation loss in the leaky region, the envelop function should apply a gentler profile at the edges rather an abrupt one. For example, if the envelop function resembles a Gaussian profile, the Fourier transform of the electric field will remain the superposition of two sinc function at $k_x = \pm n_{mode}\omega_0/c$, but the plane wave components inside the leaky region have very small intensity distribution, as shown in Fig 2.4 (c) and (d). Thus, tailoring the structure of the cavity will help us to improve the quality factor of the cavity and reduce the radiation loss of the cavity while maintaining a small mode volume.

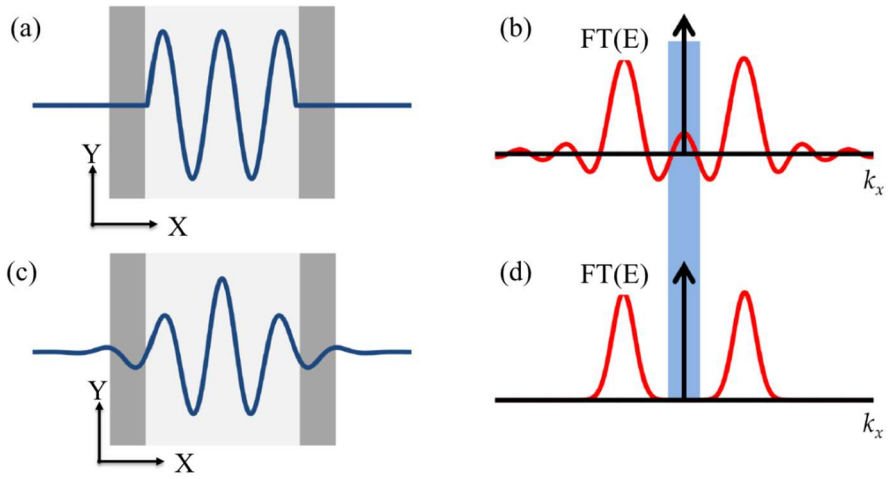

Fig 2.4 (a) Electric field distribution of the cavity is the rectangular envelop function. (b) Spatial Fourier transform of the electric field related to Fig (a). (c) Electric field distribution of the cavity is the Gaussian envelop function. (d) Spatial Fourier transform of the electric field related to Fig (c). The blue area represents the leak region ($0 < k_x < n_{clad}\omega/c$). Figures from Ref [36].

2.3.2 Ln type defects Photonic crystal cavity

Ln defect type cavities in two-dimensional photonic crystal structure are designed to achieve an extreme high quality factor, and still remain nano-scale mode volume. The high cavity quality factor per mode volume (Q/V), provides strong light-matter interactions in the cavity, which brings a variety of scientific and engineering applications, such as nano-optical filters [135,136], low-threshold lasers [137,138], and quantum information communication [128,139]. Ln type defect cavities can be realized by removing numbers (n) of holes along the $\Gamma - K$ direction in the triangular lattice. In section 2.2.2, the point defect has been discussed and a L1 type cavity is presented in Fig 2.2 (b). Due to its small mode volume, I cannot avoid large amount of plane wave components in the leaky region. Thus, a high quality factor cannot be achieved in an L1 type cavity.

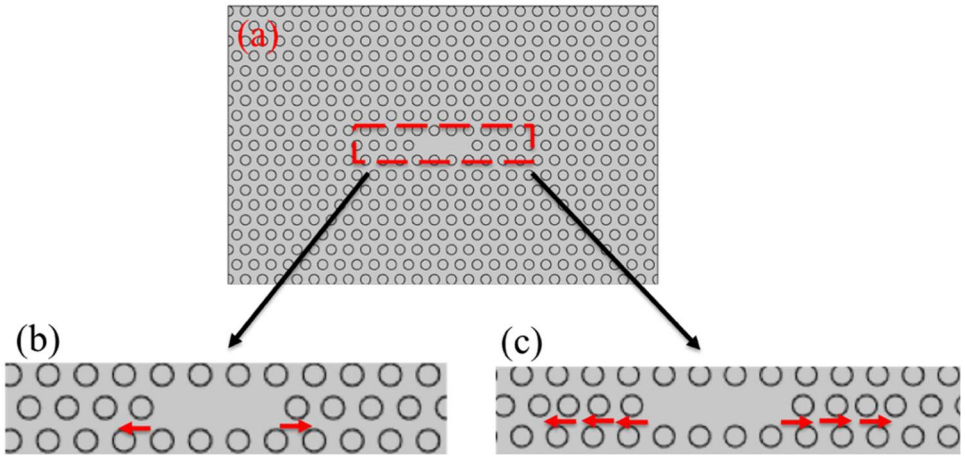

Fig. 2.5 Figures reformed from Ref [145] (a) Schematic of a L3 defect type cavity in two-dimensional photonic crystal structure. (b) The designed high quality factor L3 cavity by displacing 10 nm of two holes near the cavity edges. (c) The engineered cavity structure by fine-tuning six holes at both edges to obtain a higher quality factor, changing 40 nm, 60 nm, 80 nm, respectively.

As been discussed in Section 2.3.1, by changing the geometry structure of the cavity, the electric field of the plane wave experiences less of an abrupt transition at the edges of the cavity. The most efficiently way to improve is to remove a few more holes, such as in the L3 type cavity in Fig 2.5 (a). Removing more holes brings a larger mode. However, the dramatic increase in the quality factor of the cavity more than makes up for the increase in the mode volume. Therefore, high quality factor L3 cavity and similar structure became a popular type of PhC cavity and are topics of huge interest in the field [139-146].

By tailoring the envelope function of the electric field profile in the cavity by fine tuning the parameters (positions and size) of holes at edges of the cavity, the Ln cavity can be engineered to achieve even higher quality factors, as shown in Fig. 2.5 (b) and (c). The concept of gentle confinement adjustment was proposed by Akahane et al. [145], where two holes at the edges of the cavity have been tuned to achieve a more Gaussian-like electric field profile and decrease the amount of light in the leaky region. Fig 2.6 shows the electric field in the cavity and corresponding Fourier transform distribution, with and without fine-tuning at the cavity edges. As shown in Fig 2.6 (b), the confinement in the cavity is reduced, however the electric field is more centralized in the cavity, resulting in a more Gaussian-like envelope function (Fig 2.6 (d)), when compared to the case without air holes displacement, see Fig 2.6 (a) and (c), respectively. Thus, in Fig 2.6 (f) and (h), I can see the components of the plane wave in the leaky region have been dramatically reduced giving a 10 times larger quality factor relative to the original cavity structure (Fig 2.6 (e) and (g)). By optimizing the position of the air holes near the edges of the cavity, the quality factor can be increased from 2500 to 45000, and the mode volume is still $0.69\,(\lambda_0/n)^3$ (where λ_0 is the wavelength of light in air) [145]. Furthermore, by engineering fine-tuning more holes near the cavity edges, a quality factor of 100,000 can be reached [147].

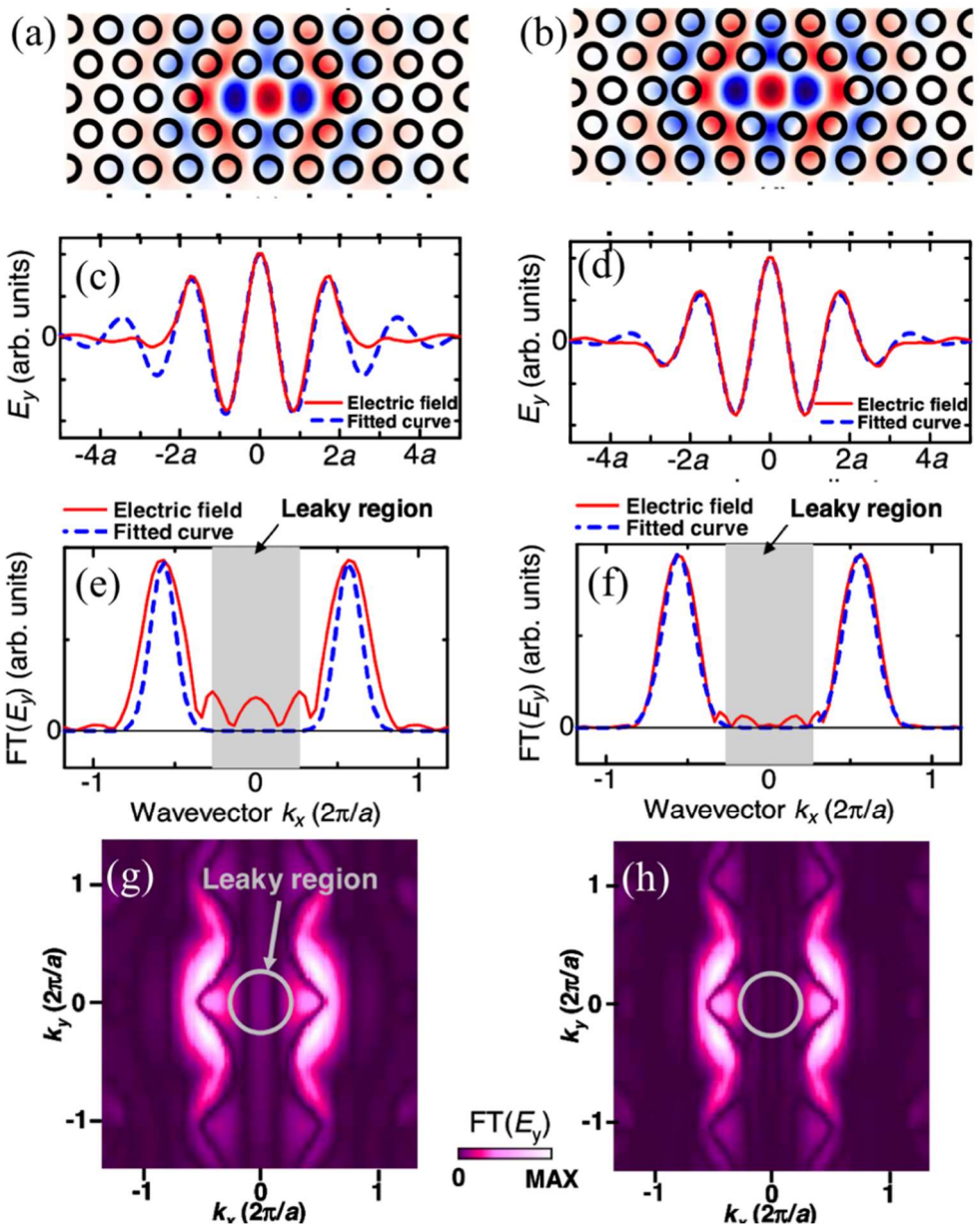

Fig 2.6 Figures from [147]. (a) and (b) The electric field of the 1st order mode of an L3 cavity, without and with fine-tuning the air holes at the cavity edges, respectively. (c) and (d) the corresponding electric field of the cavity along the centre line of the cavity (red line) and Gaussian-like theoretical fitting (blue dashed line), respectively. (e) and (f) the related one-dimensional Fourier transform of the electric field of the cavity (red line) with Gaussian-like theoretical fitting (blue dashed line). (g) and (h) the corresponding two-dimensional Fourier transform of the electric field of the cavity. The grey areas indicate the leaky region in one-dimensional Fourier transform and the grey circle indicates the leaky region in two-dimensional Fourier transform of the electric field of the cavity.

2.3.3 Heterostructure type photonic crystal cavity

In the previous section, I have discussed high quality factor cavities based on point defects in two dimensions photonic crystal structure. The key design rule is to change the electric field in the cavity to realise a perfect Gaussian-like envelope function [148, 149, 150]. However, even within fine-tuning air holes near the cavity edges, there are still plenty of plane wave components in the leaky region, which decreases the quality factor. In order to achieve a smoother profile at the cavity edges, Kyoto University proposed a double-heterostructure design in which they changed the lattice constant of the crystal based on mode gap to realize a cavity [151] (double-heterostructure cavity, as shown in Fig 2.7(b)). In 2005, they demonstrated that double-heterostructure cavities exhibit 2.8 pm linewidths and a 600,000 quality factor [152]. The photonic double heterostructure is based on a triangular-lattice structure formed by a missing row of air holes in $\Gamma - \mathrm{J}$ direction. The corresponding band diagram are illustrated in Fig 2.7 (c). The region above the blue arrow indicates the transmission region, in which photons can be propagate through the waveguide, and the red arrow indicates the forbidden region where the propagation is inhibited. The double heterostructure is carefully designed by two different lattice period a_1 and a_2 ($a_2 > a_1$), which is named as PhC-I and PhC-II respectively as shown in Fig 2.7 (b). In order to satisfy lattice-matching, the lattice period in the $\Gamma - X$ direction of PhC-I and PhC-II keeps at the area at with period a_1. These two different lattice periods create a new transmission region and mode gap region as shown in Fig 2.7 (d). Thus, when the PhC-II region is small enough, the light is strongly confined in the PhC-II region as a photonic nanocavity, giving an extremely high quality factor, up to 24,000,000 theoretically and a mode volume of $1.2(\lambda_0/n)^3$(where λ_0 is the wavelength of light in air) [153].

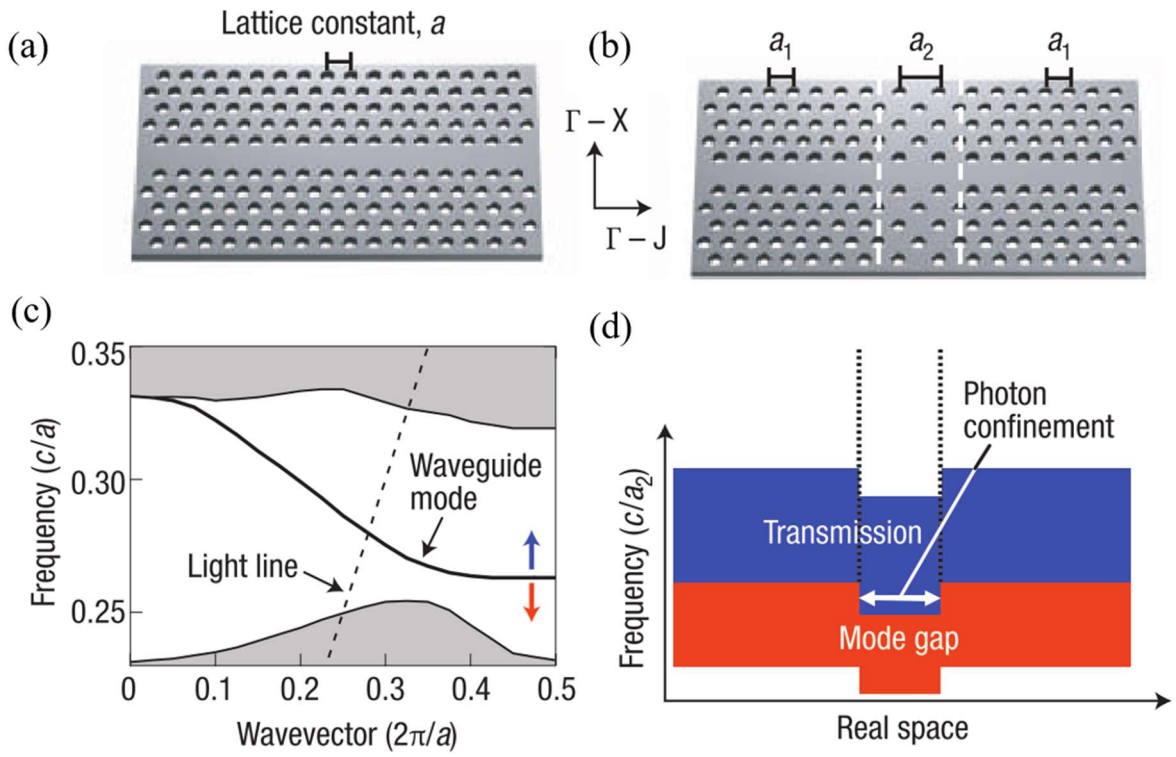

Fig 2.7 (a) The schematic of two-dimensional photonic crystal slab of triangular lattice structure with a line defect (b) The schematic of double heterostructure based on the structure in (a). The structure is formed by two different lattices, periods a_1 and a_2 (a_2>a_1). (c) the corresponding band diagram of the structure in (a). (d) the schematic of the band diagram along the waveguide direction. Only photons with specific energies can exist in the lattice period a_2 of photonic crystal structure. Figures from Ref [152].

It should be noted that the confinement of photons along the waveguide direction is not directly due to the photonic band gap effect, in contrast to the point defect in Section 2.2.3.2. It is a consequence of the mode gap effect [153] due to two different lattice periods of PhC-I and PhC-II. Photons with specific energy propagate through PhC-I waveguide and confined in PhC-II region. Furthermore, using a multistep heterostructure, the evanescent decay of the electric field stored in PhC-II into the waveguide of PhC-I can be rigorous controlled by implementing several different lattice periods. As a result, the electric field of the structure presents an almost perfect Gaussian-like envelope function, as shown in Fig 2.8. Figs (a) and (c) show the electric field distribution of a double heterostructure of photonic crystal cavity,

respectively. The more ideal Gaussian-like envelope function is presented in Fig 2.8 (c) and can be compared with the L3 mode in in Fig 2.8 (d). Therefore, it will increase the quality factor to two order of magnitude higher than that of modified L3 cavity.

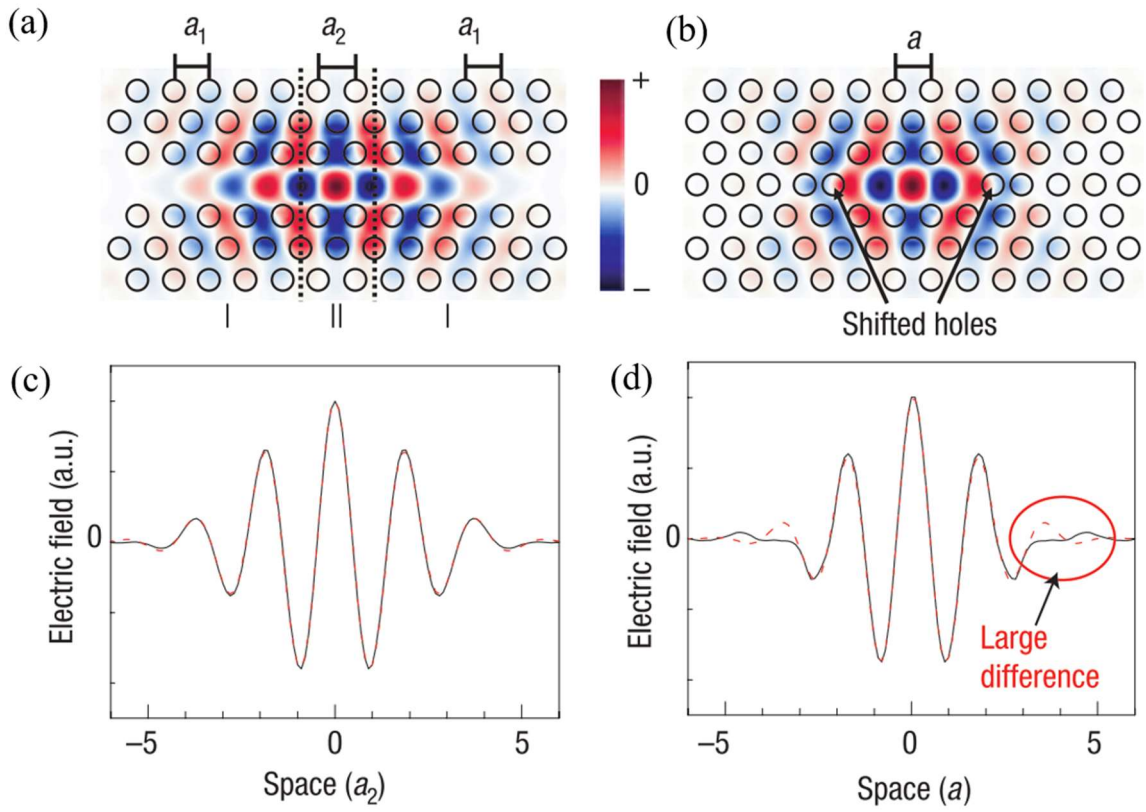

Fig 2.8 Figures from Ref [152]. (a) the electric field distribution of a double heterostructure photonic crystal cavity. (b) the electric field distribution of an L3 photonic crystal cavity. (c) the electric field profile of a double heterostructure photonic crystal cavity along the waveguide with theoretical gaussian-like envelop function (red dashed curve). (d) the electric field profile of an L3 photonic crystal cavity along the waveguide with theoretical gaussian-like envelop function (red dashed curve)

2.3.4 Linewidth modulated photonic crystal cavity

Another configuration for line defect photonic crystal cavity was proposed by Kuramochi et al. in 2006[154,155]. The linewidth modulated type cavity is formed by modulating the position of air holes near the line effect waveguide. The principle of the design is to increase the width of the waveguide at the centre of the cavity by displacement the surrounding air holes away from the waveguide. The schematic of linewidth modulated structure is shown in Fig 2.9 (a). The surrounding holes (A, B, C) have been shifted away from the waveguiding by three different distance of d_A, d_A and d_A (x, 2x/3, and x/3). The two rows of air holes near the centre waveguide is tapered to a narrow bandwidth (0.98 W), in order to get the maximum quality factor. The big difference between linewidth modulation and heterostructure is the number of displaced holes, which is less in the case of the linewidth modulated structure and the shift of air hole is based on the line defect. Fig 2.9 (b) shows the calculated resonance wavelength, quality factor, and mode volume of ***1st*** order mode as a function of shifting (x) of air holes. The calculated mode volume varied from 1.4~2.5 $(\lambda_0/n)^3$, and is only 1-6 times larger than point defect photonic crystal cavities. The quality factor is always larger than 1,000,000 for shifts of x from 3 to 30 nm. The maximum theoretical quality factor can be obtained 70,000,000 and maintain the mode volume $1.8(\lambda_0/n)^3$, as shown in Fig 2.9 (b).

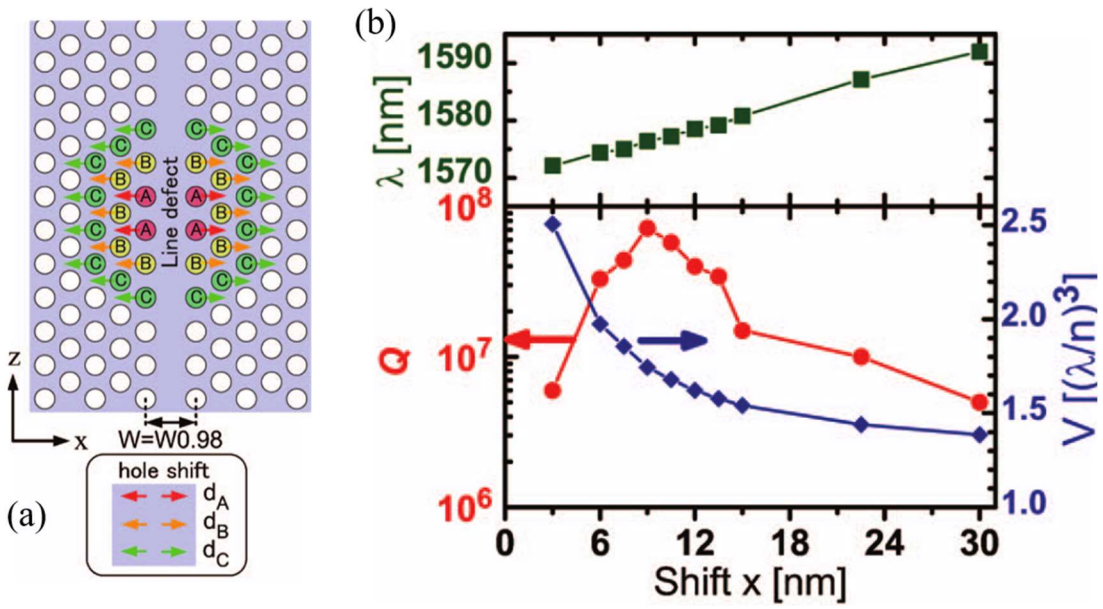

Fig 2.9 Figures reproduced from Ref [155]. (a) three configurations of mode-gap photonic crystal structure by waveguide width modulation. (b) Calculated quality factor, mode volume and resonance wavelength shifting with different value of x, respectively.

Both the heterostructure and linewidth modulated cavity can provide high quality factor photonic crystal cavity with wavelength scale mode volumes. Additionally, I can operate these cavities with one single mode at a broad wavelength range. This gives us a stronger light-matter interaction in a nanocavities for optical communication and quantum information process, relative to other cavities, such as ring resonators and micro-disc. However, one disadvantage of these cavities design is that they need very precise fabrication and electron beam lithography processes, in order to match the theoretical result. For example, in the linewidth modulated cavity, the ideal displacement of air hole ranges from 3 nm to 9 nm, which indicates that very small fabrication errors will affect the device's performance and reduce the maximum quality factor. In the next section, I will introduce a new kind of photonic crystal cavity, which improves fabrication tolerances and still gives a high quality factor at a small mode volume.

2.3.5 Dispersion adapted (DA) cavity

In 2012, Welna et al [105] proposed a new photonic crystal cavity design based on the linewidth modulation method. It follows the gentle confinement method but presents a more systematic design. The displacement of air holes is in an order of 10 nm, which gives us better fabrication tolerances, as shown in Fig. 2.10 (a). The idea is that by modifying the position of air holes, a graded potential well can be created by piecewise adapting the dispersion curve. Thus, the electric field along the waveguide direction presents a Gaussian distribution, as shown in Fig 2.10 (b). I note that the electric field profile is well matched to a Gaussian distribution. The cavity is constructed in a guiding central and surrounded by numbers of "soft" mirrors, in which the field exponentially decays. this case gives us more potential to design the cavity. I can modify the mirrors properly in order to realise a close to Gaussian-like mode shape. The most important advantage of this type cavity is to allow us to use a large range of the displacement of air hole, which ranges from 40 nm to 80 nm. This is significantly larger than any other types of gentle confinement cavities. Welna et al have proven that this type cavity to be more fabrication tolerant relative to the double heterostructure cavity, as shown in Fig 2.10 (c). This cavity can give us 2,700,000 quality factor at $1.8\,(\lambda_0/n)^3$ mode volume in theoretical calculation, and 500,000 quality factor experimentally.

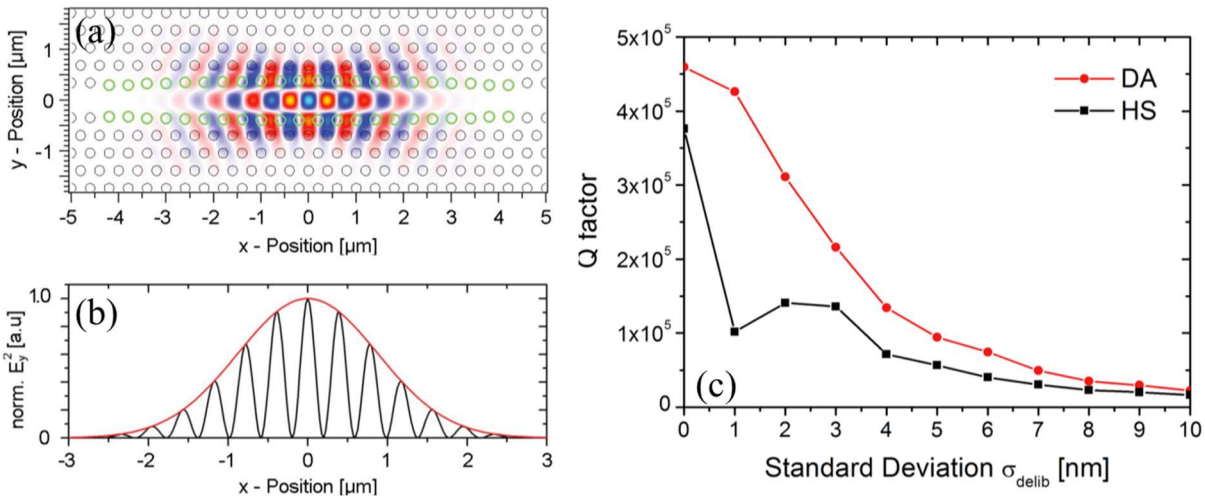

Fig 2.10 Figures reproduced from Ref [105]. (a) the electric field of the dispersion adapted (DA) cavity. The shifted holes are in green colour. The shifting has been divided into five section, starting from the centre. (b) the electric field profile of the cavity along the waveguide direction with theoretical Gaussian-like envelop function (red curve). (c) Quality factor versus the standard deviation of the fabrication disorder of DA cavity and heterostructure cavity.

2.4 Vertical coupling system

In the previous sections, I have introduced several different types of photonic crystal cavities. All these high quality factor cavities have been realised in the symmetric air-clad silicon membrane. By introducing air into the structure, the refractive index contrast to silicon is maximised, the full size of photonic band gap can be obtained. The mechanical and thermal stability of air-membrane structures have been major obstacle to their further application and integration in CMOS processes. When air-membrane structures are exposed to air, mechanical damage and continuous oxidation can affect the characteristics of devices [156, 157]. In order to improve mechanical stability of photonic crystal cavities, and preserve the high quality factor, the oxide-cladding structure and vertical coupling system have been proposed [158, 159, 160].

In the section, I will introduce oxide cladding structure cavity and vertical coupling, which are main fundamental techniques been used in this thesis.

2.4.1 Oxide-cladding structure cavity

Oxide-cladding can be either partially covering the structure (where the layer under the photonic crystal pattern is still silicon-on-insulator (SOI) remains) or by fully covering (where the layer under the photonic crystal pattern is removed) using oxide cladding or depositing SiO_2, as shown in Fig 2.11 (a) and (b). However, when the oxide-cladding has been applied, the refractive index contrast of the devices is reduced, and more light would couple to the radiation modes or the cladding modes from the photonic crystal cavity mode, reducing the quality factor. People have experimentally demonstrated that an oxide-clad L3 cavity can only reach 1000 quality factor, which is too low for most applications. However, oxide-clad line defect cavities can obtain 16, 000 quality factor in [158]. In this project, I use FO_x as the oxide-cladding layer on dispersion adapted cavities and reach 150,000 quality factor experimentally. An SEM image of such a cavity is shown in Fig 2.11 (c). Although the quality factor is decreased, those numbers are good enough to realize optical communication component function, such as filters, modulator, and laser.

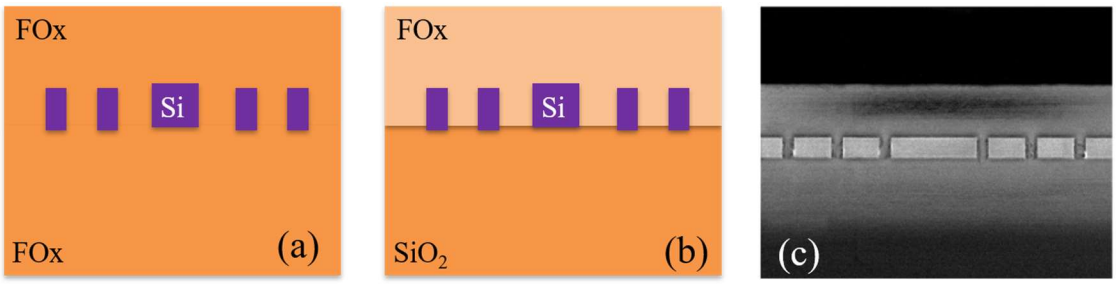

Fig 2.11 (a) Schematic of a full oxide-cladding photonic crystal cavity by using FO_x. (b) Schematic of a partially oxide-cladding photonic crystal cavity by using FO_x. (c) Cross section of a SEM image of the structure in (b).

2.4.2 Vertical coupling system

Vertical coupling is an alternative to the side coupling scheme, which consists of placing the waveguide above the photonic crystal cavity, as shown in Fig. 2.12. In this system, the waveguide mode is coupled with the cavity mode and separated by an oxide-cladding layer allowing the evanescent tails of the modes to overlap. Fig 2.12 (a) and (b) shows a schematic of a vertical coupling system with one waveguide and one photonic crystal cavity. A cross section SEM image of this configuration is presented in Fig. 2.12 (c). In most vertical coupling systems, a polymer waveguide is used as the bus waveguide. The polymer waveguide has a low refractive index contrast, which leads to a much lower propagation loss, as compared with in-plane coupling system which uses silicon waveguides. Furthermore, I can independently design the bus waveguide and the photonic crystal cavity to satisfy different optical functions. The coupling efficient between the waveguide and cavity can by precisely varied by controlling the thickness of the oxide-cladding layer. Also, by displacing the position of the waveguide, we can realise weak or strong coupling coefficients between the waveguide and the cavity. For example, I can move the position of the waveguide far away from the photonic crystal cavity region to realize a strong confinement in the waveguide. On the other hand, I can move the position of the waveguide closer to the photonic crystal cavity to achieve a strong coupling into the cavity, which can be used as modulator or for slow light components. Also, the integration of CMOS structures, such as PN junctions, is much easier as compared with in-plane coupling.

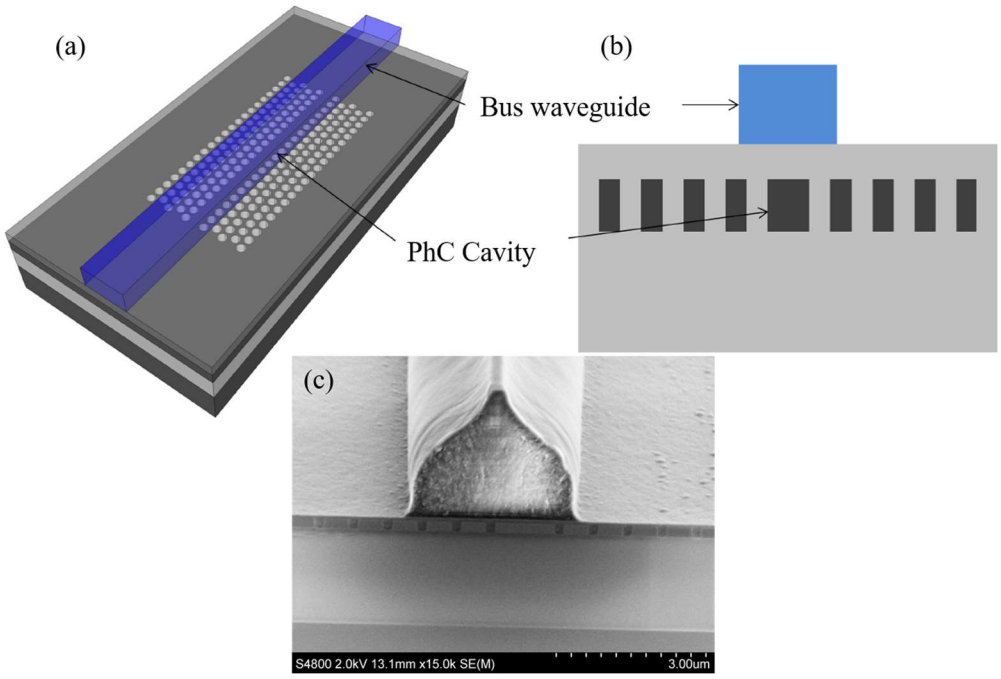

Fig 2.12 (a) Schematic diagram of the vertical coupling system. The bus waveguide is vertical coupling to a photonic crystal cavity. (b) A cross section view of the vertical coupling system at the cavity region. (c) SEM image of the structure in (c).

2.4.3 Characteristic analysis of vertical coupling

To achieve the desired coupling behaviour, the key parameters of vertical coupling is the thickness of oxide layer and waveguide dimensions. Thus, a theoretical model is built in Comsol software to demonstrate, as presented in Fig. 2.13 (a). A similar geometry shape of SU8 polymer waveguide is built up on an oxide layer (FO_x), with 3 μm × 2 μm dimensions. The thickness of the oxide layer is varied from 90 nm to 200 nm, in order to find the optimized coupling efficiency between polymer waveguide and photonic crystal cavity. Below the oxide layer, there has a silicon layer with PhC region and silica substrate. In Fig 2.13 (b) and (c) show different optical modes in different thickness of the oxide layer configurations, respectively. The thickness of the oxide layer is 110 nm and 150 nm, respectively. The optical mode is well

confined in the waveguide region as presented in Fig 2. 13 (b), compared with different thickness configurations in Fig 2.13 (c).

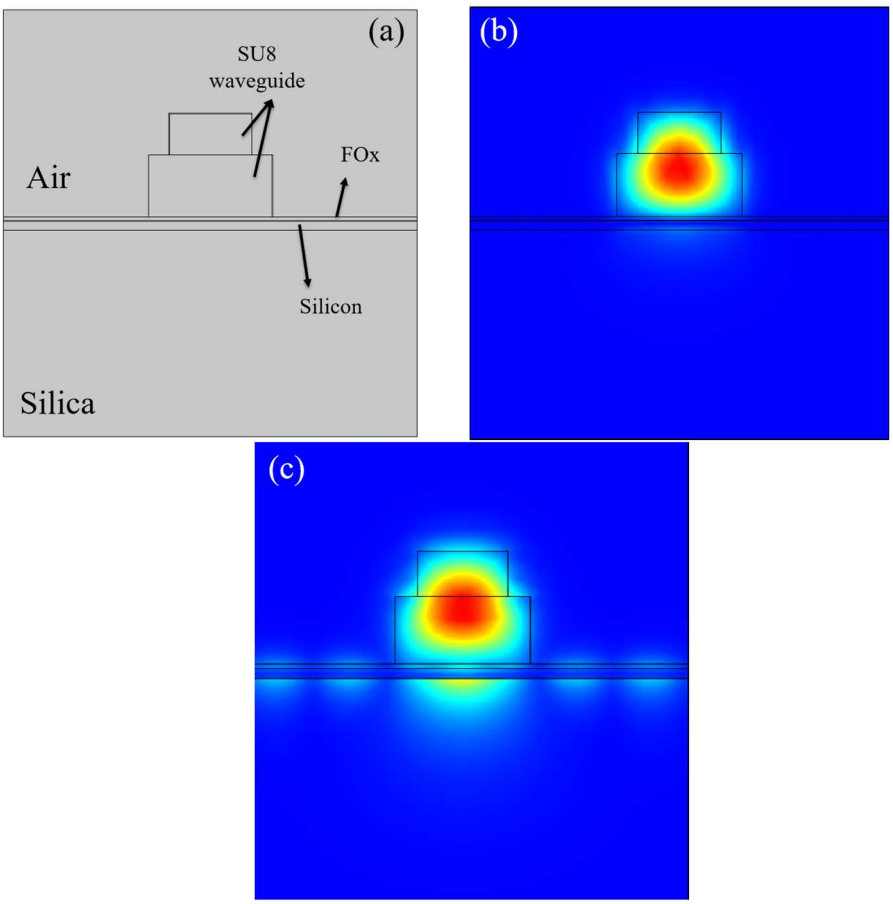

Fig 2.13 (a) Schematic diagram of the vertical coupling system in Comsol simulation software. The bus waveguide is designed as SU8 waveguide (b) optical mode with 110 nm thickness of the oxide layer. (c) optical mode with 150 nm thickness of the oxide layer

In order to study coupling coefficient (Q_c) between bus waveguide and photonic crystal cavities, the S-parameter has been calculated by using COMSOL 3D simulation. Q_c with different oxide layer thickness have been presented in Fig 2. 14. To achieve the best coupling coefficient, 110 nm thickness is the desired thickness in the design. By combining this configuration coupling system with high quality factor photonic crystal cavities, I can build a new slow light system,

which has a low propagation loss and large group delay. Within its high integrated CMOS properties, this new type of slow light system become an ideal functional component for on-chip optical communication, compared with traditional in-plane coupling system.

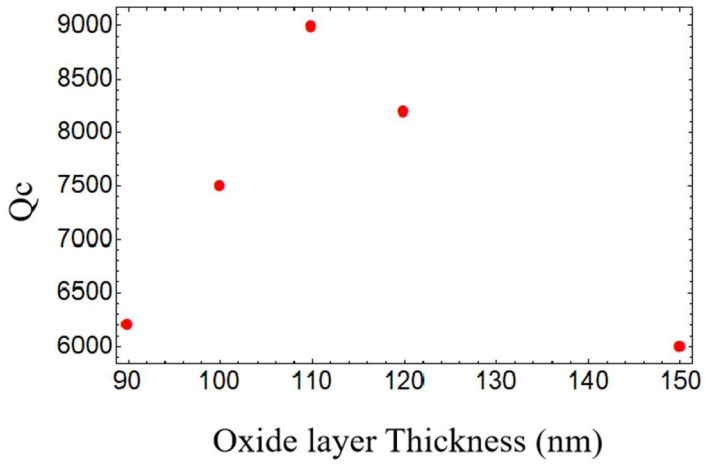

Fig 2.14 Different coupling coefficients (Q_c between SU8 polymer waveguide and photonic crystal cavities with different thickness of the oxide layer, respectively.

2.5 Discussion

In this chapter, I have introduced an overview of the two-dimensional photonic crystal band gap theory and different configurations of high quality factor photonic crystal cavities. Furthermore, the vertical coupling system is introduced as a new platform for optical communication, due to low propagation loss and high integration with CMOS.

Photonic crystal structures have been widely studied and gain great research interest as a perfect photonic insulator to confine light in a small volume. Slow light devices are important components for on-chip optical information communication, optical signal processing and quantum computing. However, there are several disadvantages to realizing slow light in

photonic crystal cavities and waveguide structures. By using one single cavity to achieve slow light effect, I can only achieve a limited slow light factor and operated at a very narrow bandwidth range. Meanwhile, the fabrication tolerance of a high quality factor photonic crystal cavity is another big problem. By using photonic crystal waveguides to obtain slow light, I can have a broader operation bandwidth, but a smaller slow light factor and losses system, compared with photonic crystal cavities structure. In order to achieve higher group delay compared with photonic crystal cavities and waveguide structures, an optical analogue of EIT system is introduced to achieve a large group delay with a broad operation bandwidth, such as ring resonator and photonic crystal in-plane coupling system. By using the vertical coupling system with oxide-cladding photonic crystal cavity, I can achieve optical analogue of EIT system within larger group delay and broader bandwidth system, while maintain a lower propagation loss, compared with any other existed system.

In Chapter 4 and 5, I will explain how to achieve optical analogue of EIT system by using coupled resonators and demonstrate the functionality of optical analogue of EIT system

Chapter 3 Fabrication tools and processes

3.1 Introduction

This chapter introduces a brief overview of the fabrication tools and techniques that were used throughout this thesis. Most of my fabrication process followed this order: initially the designed pattern was generated by lithography methods, then reactive ion etching (RIE) was used to transfer the pattern to different materials, such as silicon and silicon dioxide; subsequently, metal evaporation or hydrofluoric acid (HF) etching is applied for different device requirements. Thus, I begin this chapter by introducing the two lithography techniques, electron beam (e-beam) lithography and photolithography. Then I will continue by describing the reactive ion etching (RIE) process, and hydrofluoric acid (HF) etching process Finally, I discuss the metal contact formation using thermal evaporation.

3.2 Lithography methods

3.2.1 Photoresists

In the photolithography process, a light-sensitive material is used to form a designed patterned coating on the surface of the sample. This light-sensitive material is also known as a photoresist. In general, the photoresist can be classified into two types, a positive photoresist and a negative photoresist. The positive photoresist is degraded by light and the developer will dissolve away the regions that were exposed. In the case of the negative photoresist, the photoresist is strengthened by the light, due to the cross-linking or polymerization between molecules. The developer will dissolve away the regions that were not unexposed and remain behind the exposed area. In this work, several photoresists have been used, i.e. ZEP 520A (positive),

Polymethyl Methacrylate (PMMA, positive) and Microchem SU8 (negative) as e-beam lithography resists and S1818 (positive) as a photolithography resist. ZEP 520A has a sufficient etching resistivity to allow for a direct transfer of the pattern from the resist into the silicon without requiring a hard mask, meanwhile maintaining a high resolution. This allows us to lithographically define photonic crystal holes and sub-100nm features. SU8 is used to define the bus waveguide, and PMMA is used in the lift-off process to define the metal evaporation window. S1818 is used to define the waveguide in some initial test devices. S1818 and PMMA can also be used for the mask cover in HF etching. The photolithography procedure consists of the following steps. In the beginning, the resist is deposited on the sample by spin-coating and is then baked to drive off the solvents. After baking, the resist is exposed using the lithography system, and the exposed area is removed by using a developer. In order to avoid overdeveloping the sample, any residual developer is removed, using a suitable solvent. Once the remaining resist mask is not required any more, a resist stripper is used to clean away the rest of the resist. The exact times and chemicals used are presented in Table 3.1 and Table 3.2

Resist	Spin speed (rpm)	Thickness (nm)	Baking time (min)	Baking temperature (°C)
ZEP 520A	3000	400	10	180
PMMA	5000	600	5	180
SU8	2000	2100	3	100
S1818	5000	2000	1	100

Table 3.1 shows the spinning recipes used for ZEP 520A, PMMA, SU8 and S1818 resist

Resist	Developer	Development time (sec)	Development temperature (°C)	Developer remover	Resist stripper
ZEP 520A	Xylene	45	23	isopropan-2-ol (IPA)	1165
PMMA	De-ionized (DI) water: IPA (3:7)	60	Room temperature	IPA	Acetone
SU8	EC Solvent	20	Room temperature	IPA	1165
S1818	MF319	35	Room temperature	DI water	Acetone

Table 3.2 shows the process recipes used for ZEP 520A, PMMA, SU8 and S1818 resist

3.2.2 Electron-beam lithography

In electron beam lithography, the patterns are defined using a focused beam of electrons to expose on the surface covered with an electron-sensitive film, known as e-beam resists. To achieve high resolution patterns, e-beam lithography is preferred over photolithography, as it allows the definition of features down to a few 10 s of nm in size. The e-beam changes the solubility of the resist, enabling selective removal of either the exposed or non-exposed regions of the resist by immersing it in a solvent. In my all work, the samples were fabricated on RAITH eLINE plus nanolithography system, with a maximum acceleration voltage of 30 kV and a maximum write-field size of 1000 × 1000 μm^2. There are several factors that determine the best resolution that can be achieved with the e-beam writer, as shown below [161]:

$$d_f = 0.9(\frac{R_t}{V_b})^{1.5} \quad 3.1$$

Where d_f is the effective beam diameter at the silicon/resist interface. R_t is the resist thickness and V_b is the acceleration voltage. The equation assumes a spot size of approximately 1 nm on the top resist surface. Additionally, the proximity effect is another major issue that affects resolution in e-beam lithography writing and occurs due to the interaction of the beam electrons between the resist and the substrate. When the electrons are incident on the surface of the resist, the scattering can occur over large distances from underlying films and/or the substrate. This effect leads to a variation of the desired exposure over distance, which becomes more severe when the resist is thicker. This scattering is known as forward scattering. Besides exposing the resist, the forward scattering also leads to a broadening of the initial beam diameter. Therefore, using a thinner e-beam resist will decrease this effect. Meanwhile, by increasing the acceleration voltage, the forward scattering effect can be weakened, However, it will increase the amount of back scattering from the substrate to the resist, as shown in Fig 3.1 (a) and (b). This back scattering is caused by the electrons penetrating the substrate. These electrons can

still contribute to the resist exposure by scattering back into the resist, affecting feature sizes. This backscattering process originates from collisions with a heavy particle (i.e. substrate nucleus) and leads to a wide-angle scattering of the light electron from a range of depths (μm) in the substrate. Thus, a solution to the proximity effect is required to fabricate devices with the designed feature sizes and consequently well-defined spectral features. In my e-beam lithography design, the proximity error correction is carried out using Nanopecs. This a software package from Raith that calculates the proximity effect and adjusts the exposure dose of each object in the design pattern accordingly. An example of a photonic crystal cavity structure that used in this work, after using proximity error correction, as shown in Fig 3.1 (c). The holes far away from the center region of the photonic crystal region is given a high exposure dose. In order to compensate for the back-scattering electrons from the nearby region, the holes at the center region of the photonic crystal cavity design are assigned a relatively low exposure dose.

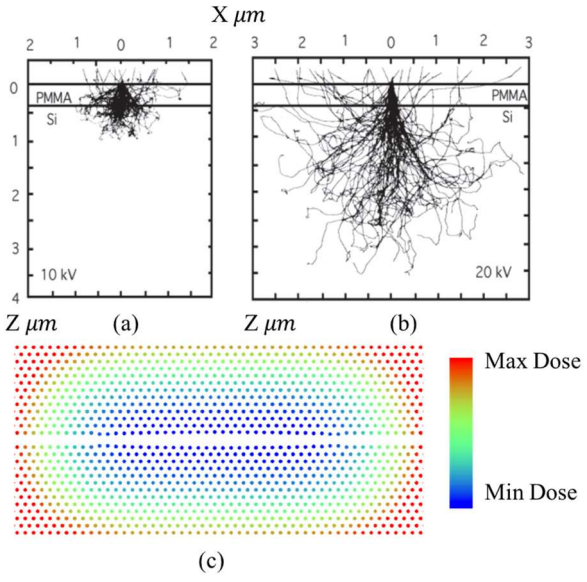

Figure 3.1: Figures taken from reference [161]. At (a) 10 kV and (b) 20kV of e-beam lithography writing, the scattering of electrons in PMMA resist and silicon substrate is presented by Monte Carlo simulation. (c) shows an example of a photonic crystal cavity design after proximity error correction by Nanopecs.

3.2.3 Photolithography

Photolithography, also known as optical lithography or UV lithography, is an efficient and fast process used in microfabrication to transfer the desired pattern to the substrate. In this work, I use an EVG620 mask aligner. The exposure wavelength of the EVG620 mask aligner is 365nm at 500W of lamp power and the exposure resolution is around 1 μm in "soft-contact" mode. In the "soft-contact" mode exposure, the substrate is brought into contact with a photomask by a preset force during exposure. The photomask is used to expose the desired patterns on the resist. This photomask consists of a quartz plate, one side of which is coated with UV blocker (iron oxide in our case) into which the required pattern has already been transferred. The exposure process is based on the photochemical reaction of the resist to UV photons. In the case of a positive photoresist exposure, the exposed areas become soluble in the developer. For a negative photoresist, the un-exposed areas become soluble in the developer. The process of lithography is depicted in Fig 3.2. For most of our photolithography steps (except the lift-off process), a single layer of the positive photoresist S1818 is used. The recipe and fabrication steps description of S1818 is presented and described in Table 3.1 and Section 3.2.1, respectively.

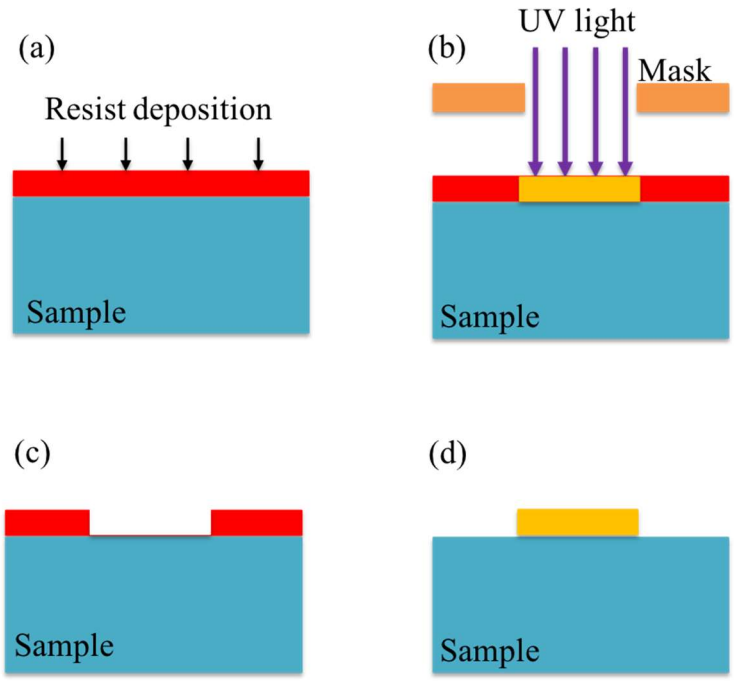

Fig 3.2 Photolithography process flow: (a) a photoresist (PR) is spin on the substrate. (b) Sample is then exposed under UV light through a photomask. (c) In the case of the positive photoresist, the exposed part is dissolved during the development. (d) For negative photoresist, the exposed part remains after development.

3.3 Reactive ion etching

Once the pattern has been generated by lithography, using RIE, it is transferred from the resist into the material of interest (in this work: silicon, silicon dioxide and Hydrogen silsesquioxane). RIE is a type of dry etching that uses chemically reactive plasma to remove desired material on the substrate. The plasma is generated by applying a strong radio frequency (RF) to the electrode. The schematic of the RIE chamber is shown in Fig 3.3. The substrate plate acts as one electrode. Another electrode is positioned above the plate, and contains a small ring, which injects gas into the chamber. The sample is placed in the middle of the bottom plate between the two electrodes. The gas pressure inside the chamber is precisely controlled by the butterfly valve. When an RF electromagnetic field is applied, creating reactive plasma by oscillating the

electric field and ionizing the gas molecules by stripping them of electrons. The RF field also generates a negative DC component and this DC bias accelerates the positively charged ions towards the sample resulting in etching. Compared with some other dry etching techniques, such as chemically assisted ion beam etching, the chemical and physical components of the RIE are interlinked. The physical component is dependent on the downward acceleration from the DC bias. This DC bias is directly dependent on the RF power, which in turn also causes the plasma formation and, therefore affects the chemical component of the etching process.

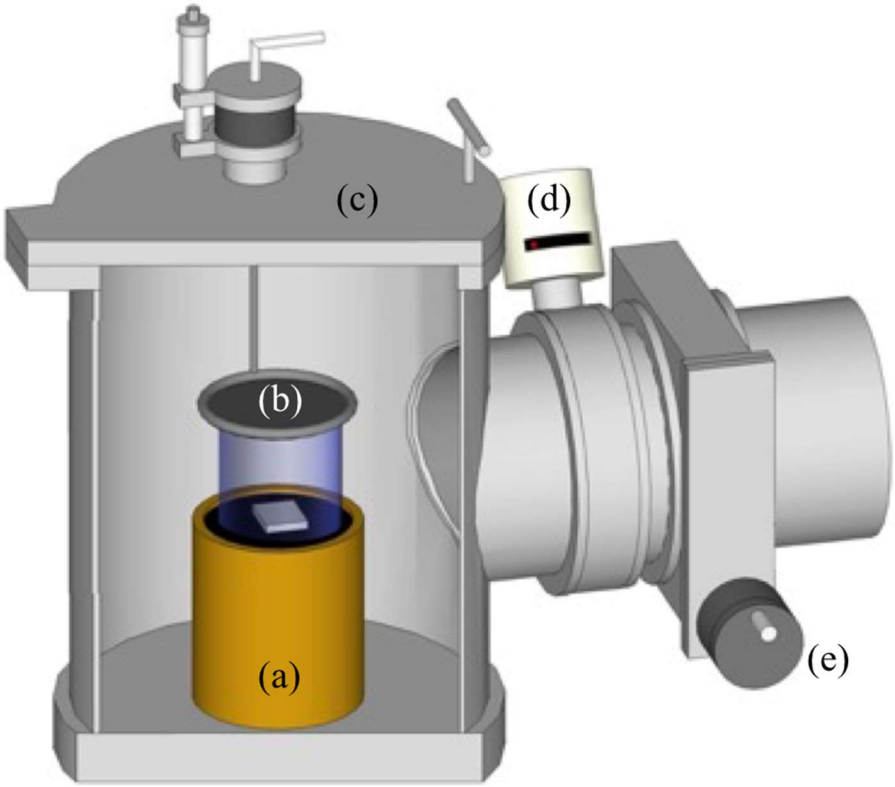

Fig 3.3 Sketch of the RIE chamber. a) and b) are the electrodes between which the sample is placed. Around electrode b) is the ring, through which the gases are injected into the camber. c) Lid for loading and unloading the sample. d) Gate valve connecting the RIE chamber to a turbo pump. e) Butterfly valve for pressure control during the etch process.

The gas mixture and etching recipes chosen depends on the corresponding substrate materials [162,163]. For silicon, an equal volume mixture of SF_6 and CHF_3 gases are used. Here, the SF_6 and CHF_3 contribute to the silicon etching in different roles. CHF_3 can polymerize on the sidewalls and thereby protects the sidewalls from being etched. This leads to the desired vertical side walls.

Substrate	Gas-mixture	Flow rate (sccm)	Etch pressure (mBar)	RF power (W)	DC bias (V)	Etch rate (nm/min)
Silicon	SF_6 CHF_3	100 100	$5e^{-2}$	19	-210	110
FOx	CHF_3	100	$4e^{-2}$	41	-500	20

Table 3.3 – RIE recipes for different substrates.

Hydrogen silsesquioxane, commercially available as FO_x (Flowable Oxide), is very similar to silicon dioxide in composition and contains mostly silicon and oxygen atoms. The reactive gas used is CHF_3 in this case. In this process, the carbon atoms from CHF_3 gas forms the protective coating on the sidewalls as etching proceeds. Table 3.3 summarizes the optimized RIE recipes used for different substrates. Two SEM images of photonic crystal after etching are shown in Fig 3.4.

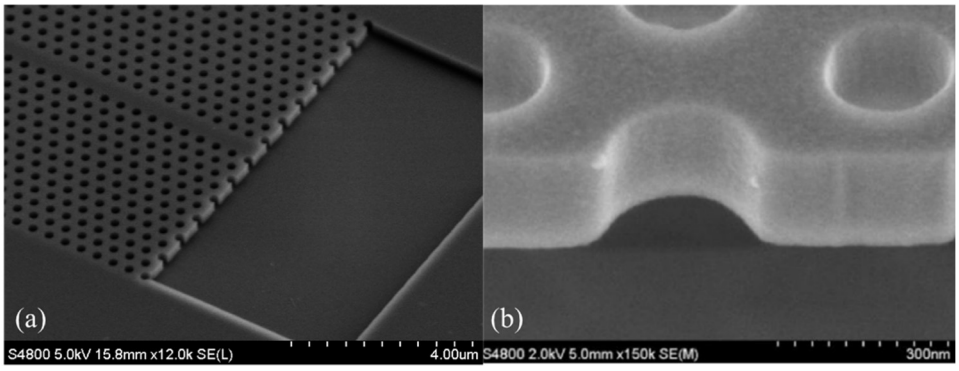

Fig 3.4 SEM images of photonic crystal after etching.

3.4 Hydrofluric (HF) acid etching

In my PhD studies, HF etching was used during the fabrication of initial test devices based on photonic crystal cavities. Additionally, the HF etching can be applied to check the etching progress after the RIE etching. In case of photonic crystal fabrication, after the RIE etching, the photonic crystal still resides on the buried oxide layer as shown in Fig 3.4 (a). This structure will lead to an asymmetry in vertical direction. The TE and TM modes will be coupled, and the bandgap also will be reduced [36]. This effect can be minimized by either depositing an oxide layer above the photonic crystal [158] or removing the buried oxide layer. An oxide layer covered photonic crystal is much more stable compared with a thin photonic crystal membrane and have a stronger tolerance from mechanical damages. However, if comparing it to the photonic crystal membrane, it has some disadvantages. The refractive index difference between the hole and the slab is reduced when the photonic crystal is covered with an oxide layer, leading to a reduced bandgap and bandwidth for slow light engineered waveguide [92, 87, 159]. Additionally, the propagation loss will increase due to a reduced refractive index contrast [158]. Therefore, the best resolution in the photonic crystal membrane fabrication is to remove the oxide layer. Here, the HF acid is used to remove only SiO_2 and leaves Si. In order to achieve optical isolation of the waveguide mode, the 1~2 μm etching thickness is required. The HF etching process is shown in Fig. 3.5

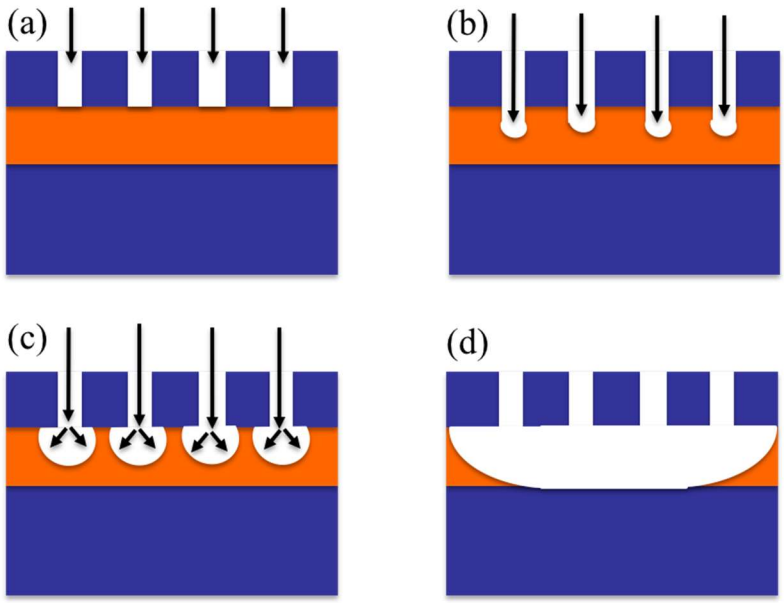

Fig 3.5 Schematic of the HF etching procedure. (a), (b) and (s) show the silica (orange) is slowly etched by HF, while silicon (blue) is not. (d) presents an undercut under the silicon membrane.

The etch leads to a 1~2 μm wider undercut under the silicon structure. This undercut will lead to the oxide under the hole removed, but also the oxide under the access waveguide removed. However, the access waveguide does not attach to both sides and have a 3~4 μm width. As a result, the structure becomes very unstable after the etching, as shown in Fig 3.6 (a). Therefore, a protective photoresist layer has been used in the etching process. The sample is covered by a polymer resist, i.e PMMA and S1818. The etching windows are opened above the photonic crystal region, and the access waveguide region is still covered by the resist. A diluted etching recipe is used to slow down the etching effect, as mixture HF with water (DI water: HF =5:1). The initial etching time is set as 10 min. After checking the undercut, if necessary, the sample is etched for an additional 5 min. This procedure is repeated, until a sufficient undercut has been achieved. A SEM image of photonic crystal waveguide after the HF etching is presented in Fig 3.6 (b). Additionally, I use the HF etching as a tool to check the silicon etching after I set up a new recipe in RIE etching. After the HF etching, I can easily identify the silicon layer

(above the oxide layer) etching deepness and indicates us to adjust the recipe of photonic crystal structure etching.

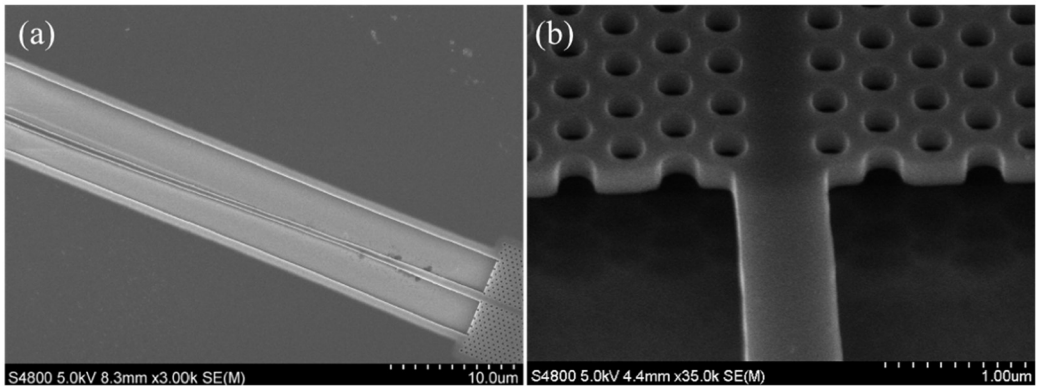

Fig 3.6 SEM images of photonic crystal after HF etching. (a) shows a) Sample etched without HF mask. The access waveguide is starting to bend. (b) Sample etched with appropriate HF mask. The photonic crystal and the access waveguide are well functionally work.

3.5 Electron-beam physical vapour deposition and lift-off process

3.5.1 Electron-beam physical vapour deposition

Electron-beam physical vapour deposition (EBPVD) is a form of physical vapor deposition method used to deposited thin films by bombarding a source material (known as target material) with an electron beam. The electron beam is given off by a charged tungsten filament under high vacuum, through thermionic emission, field electron emission or the anodic arc method. The electron beam makes atoms from the target material to transform into the gaseous phase, then precipitate into solid form, coating any surface in the vacuum chamber. The target material is usually in the form of crystals, flakes, wires or ingots, and is placed in a water-cooled crucible.

To prevent chemical interaction between the filament and the target material, the filament is kept out of sight of the crucible, as shown in Fig 3.7. A magnetic field is applied to direct from the source to the target crucible, and an additional electric field is employed to steer the beam over the crucible's surface, which keeps uniform heating. The sample is fastened on the substrate holder and rotates at a particular speed to achieve a uniform deposition of the film over the surface of the sample.

An Edwards AUTO306 EBPVD system is used in the thesis presented here. An acoustic crystal monitor is employed to the system as shown in Fig 3.7 and connected to an Edwards film thickness monitor to controll the thickness of deposited material. The working base pressure of the chamber is typically pumped to below 10^{-6} mBar, before each deposition process. The deposition rate for the system used is between 0.1 and 0.3 nm/sec, corresponding with different target material at the average filament current.

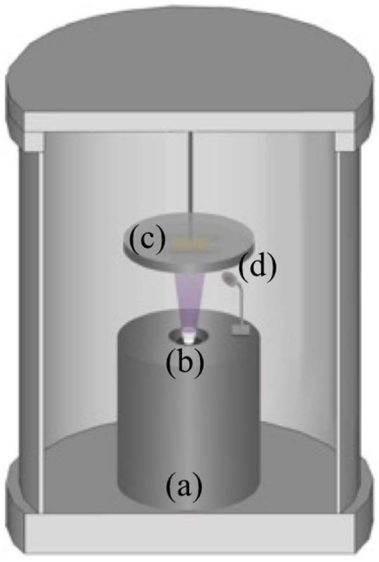

Fig 3.7 Schematic of EBPVD chamber. (a) a metal holder, which consist clamps and a cooling system. (b) Target crucible (c) Sample holder and substrate (d) crystal monitor

3.5.2 Lift-off process

The lift-off process is a simple technique to produce patterned layers of material on a substrate. It is an alternative to etching and is therefore useful in process steps where etching is difficult or not feasible. The primary use of lift-off in this work is the patterning of ohmic contacts for mirco-heater devices. During my work, to realize the lift-off process, the substrate was spun with a 500 nm thick layer of PMMA (positive resist) and was baked at 180 ^{0}C for 10 minutes. The PMMA recipe is presented in Table 3.1. The desired evaporation window was patterned on the resist using e-beam lithography and then developing in a mixture of DI water and IPA (DI water: IPA=3:7). The desired material was then deposited on the substrate using EBPVD. After the evaporation, the sample is put in Acetone, which dissolves PMMA and the deposited metal remains on the structure. Then the resist was stripped, removing with it the deposited material from the undesired parts. A quick (30 s) Piranha (3:1 H_2SO_4, H_2O_2) cleaning is considered if necessary. The flow of the lift-off process is shown in Fig 3.8.

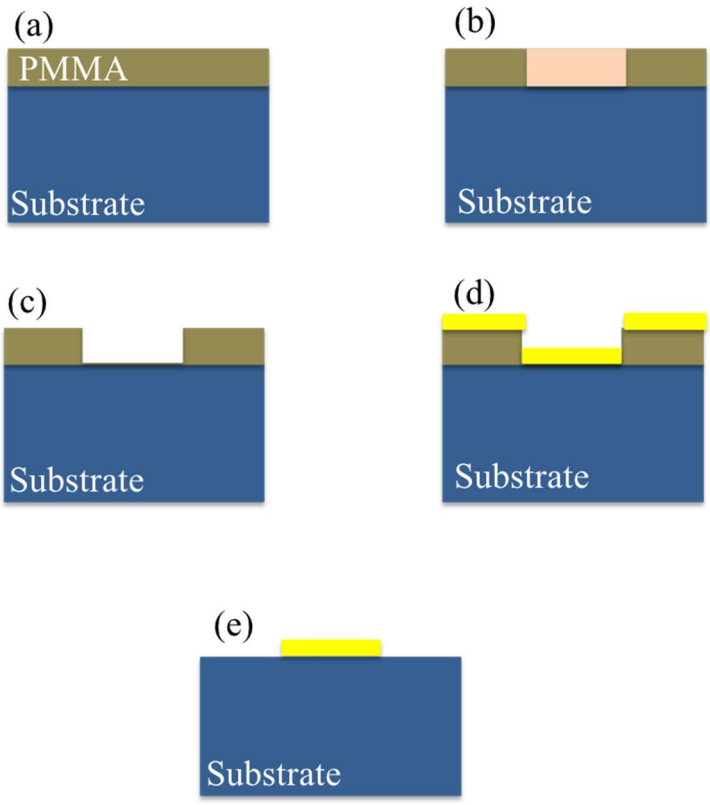

Fig 3.8 Lift-off process flow. (a) Substrate with PMMA resist on it. (b) The desired design is exposed on the resist via photolithography or e-beam lithography. (c) Substrate after development in a 3:7 mixture of DI water and IPA. The exposed areas have been removed. (b) A film of the desired material is deposited on the entire surface of the substrate. (e) The substrate is immersed in Acetone, which strips it from the resistand the deposited material from the undesired areas.

3.6 Fabrication induced disorder

As mentioned before, a photonic crystal mode below the light line is intrinsically lossless. However, in real structures, propagation loss is mainly caused by disorder created during the fabrication process. In this section, I will study different types of the origin disorder present in my photonic crystal fabrication steps. Furthermore, I will discuss several standard procedures aimed at minimizing the disorder introduced during the fabrication process. The main origin disorders are caused by the RIE and e-beam lithography fabrication steps (in Section 3.3 and

Section 3.2.2, respectively). A poor etching recipe leads to a sidewall roughness and silicon etching completeness. Additionally, during the electron beam exposure, or subsequent resist spin and development, the exposure pattern will be transferred into the silicon slab after the RIE process. Any of these disorders contribute to the extrinsic scattering loss and a low intrinsic quality factor of a photonic crystal cavity.

3.6.1 Disorder in reactive ion etch

As already mentions in Section 3.3, the RIE process contain two components, one chemical and one physical component. It is important to balance these two components through an appropriate etching recipe. The majority of disorders in reactive ion etch are an underetch of the resist mask, a widening of the bottom photonic crystal holes and curved sidewalls. This effect is mainly caused by chemical loss directionally. If the disorder caused by physical component dominates the etching, the silicon is effectively sputtered and not removed from the sample. Therefore, it can redeposit at the bottom of the hole, leading to an angled sidewall or redeposit on the sidewalls themselves. Additionally, in the dispersion adapted cavity fabrication [105], the completeness of etching through the silicon (above the buried oxide layer) can also affect the intrinsic quality factor of the cavity and coupling coefficient to the bus waveguide. Thus, using a suitable etching time is a key factor to optimize the etching fabrication. In conclusion, both of them cause deviations of our samples from the ideal photonic crystal design and introduced scattering losses. Additionally, the angled sidewalls destroy the symmetry of the structure and can lead to TE-TM conversion.

SEM images of etching result during the fabrication are shown in Fig 3.9. In Fig 3.9 (a), the etch resulted in sidewalls in the bottom, and in Fig 3.9 (b) shows the roughness on the sidewall due to redisposition of other previously etched material. In Fig 3.9 (c), the sidewalls caused by

using wrong RF voltage can be observed. Fig 3.9 (d) shows a photonic crystal structure under appropriate etching recipe. The sidewall is vertical and low roughness in the holes.

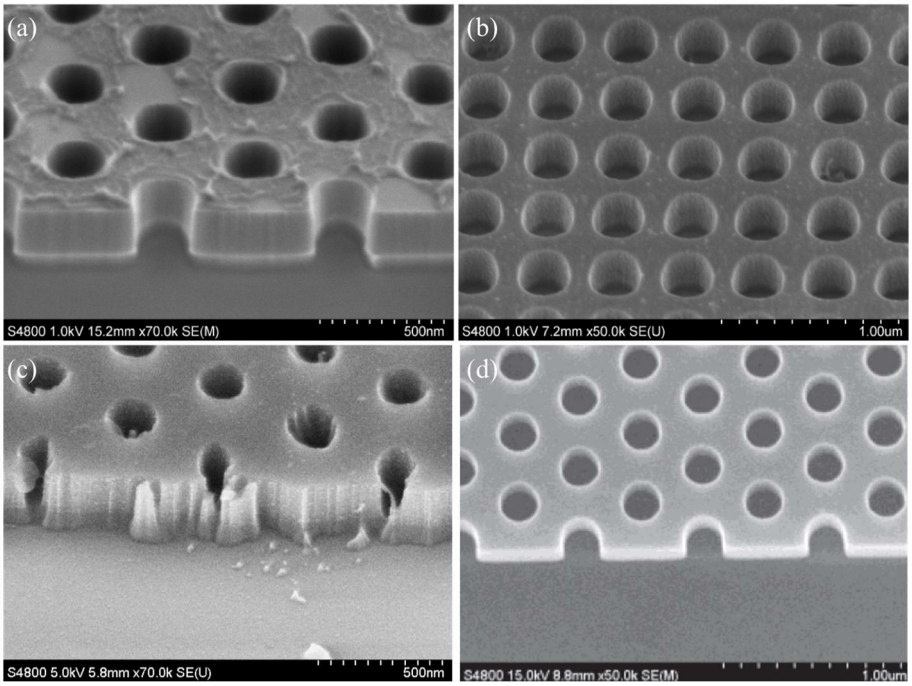

Fig 3.9 SEM images showing (a) etch with angled sidewalls (a thin resist layer was remaining on the top surface) (b) sidewall roughness caused by redeposited material. (c) etch with angled sidewall and roughness. (d) A good etch with low sidewall roughness and straight sidewalls.

3.6.2 Disorder in electron beam lithography

The disorder introduced during in e-beam lithography can generally be classified into three configurations, deviations of the hole shape, the hole radius and the position error, relative to the ideal photonic crystal design. Sketches of three configurations are shown in Fig 3.10 (a)-(c), respectively. In the following, I will explain different physical origins for those three configurations.

The deviations of the hole shape are mainly related to the polymer resist used and/or noise during the e-beam exposure. The noise in the e-beam writer is due to the electron source and the beam control units. During the e-beam exposure, the polymer chain broke into smaller components when the incident electrons reaches the bond energy. Those components affect the shape of the exposed line or circle. Additionally, a variation in the hole shape will also happen when there is much noise in the e-beam writing. These irregularities in the mask will transfer into the silicon layer after the etching as shown in Fig 3.10 (d) and (e). Thus, I choose ZEP-520A as the e-beam resist for the photonic crystal fabrication. ZEP-520A has a small chain size and a good mixture of etch resistance, resulting to a high resolution and low disorder devices.

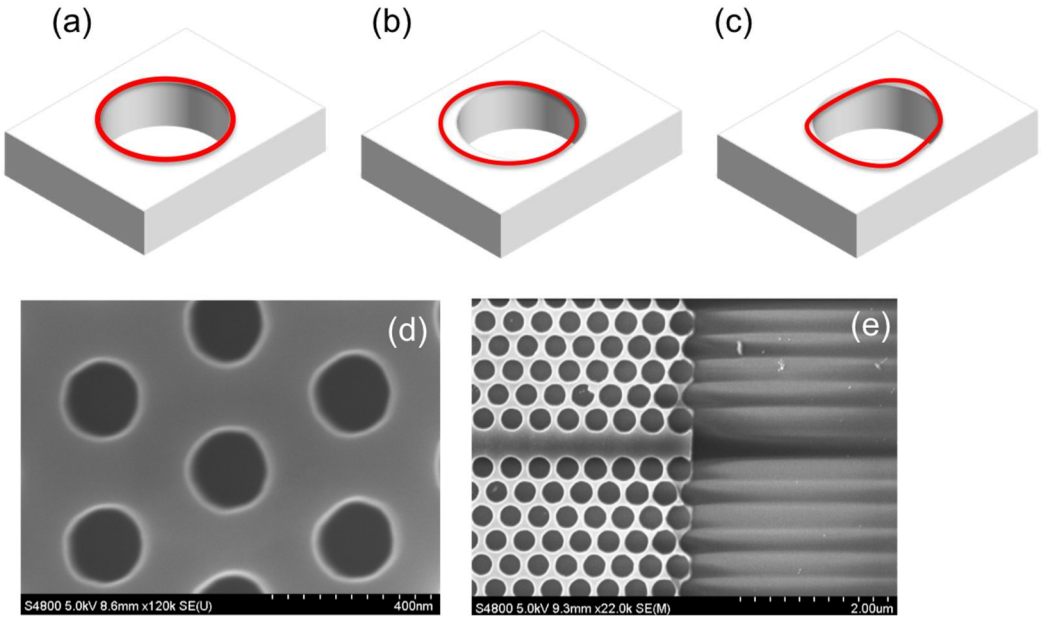

Fig 3.10 Schematic of three different configurations of disorder deviations happen in photonic crystal fabrication in (a)-(c). Red curves present varies changings of the real fabricated photonic crystal, compared with white area (the ideal photonic crystal design). (a) shows an increased radius of the photonic crystal hole. (b) represents the position error of a photonic crystal hole. (c) shows a random variation of the photonic crystal hole boundary. (d) and (e) represents with a distorted shape and an increasing radius of the photonic crystal hole, compared to the origin photonic crystal design, respectively.

The disorder in hole radius is mainly caused by a wrong dose exposed in the resist from the ideal exposure dose. As we known, the resist thickness become thicker and gradient at the edges of the sample, which can be called as resist break down. Therefore, the e-beam exposure becomes inhomogeneous and uncontrollable. In this case, slightly larger than necessary samples and a uniform spun resist layer are required in the e-beam lithography. All devices should be placed in the centre of the sample, where the resist is more uniform, compared to the edge beads. Besides, inaccuracies during the proximity effect can also lead to the variation in the hole radius.

In our photonic crystal design, each circle cannot be divided into smaller parts during the proximity correction. Thus, the complete circle will be exposed at the same electron dose. The second origin of the radius disorder is the statistical fluctuation of the beam current during the exposure process.

The majority of disorder of the position error comes from two origins. As known in the e-beam writing, the exposure positioning of each photonic hole is achieved by deflecting the electron beam by using magnetic coils. However, it has a limited accuracy [164]. During the exposure, the hole position is locked onto the e-beam grid, this finite accuracy leads to a variation noise of the sample. Additionally, there is a random variation in the hole position due to a noise on the magnetic coils used to defect the electron beam. The shift will become dramatic when the holes are closer to the edge of the write field, as shown in Fig 3.11

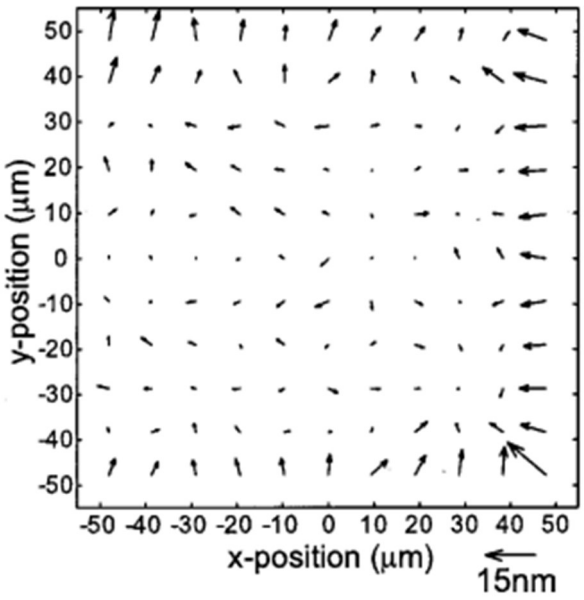

Fig 3.11 the pattern positioning error within a 100 μm write field is shown. Figure taken from the reference [9].

Another origin, which can also lead to variation in the hole shape of some hole and the position error, is well known as stitching error. When exposing a large areas design, the e-beam system will divide the design patterns into multiple segments, known as write field. Each writing field is exposed separately and controlled by the software program. The new writing field start to write once the previous one has been finished and the sample stage moved to the desired position. In this case, the stitching error might happen and lead to the position error at the boundary between two writing field (as shown in Fig 3.12), due to the accurate and vibrate of the sample stage movements.

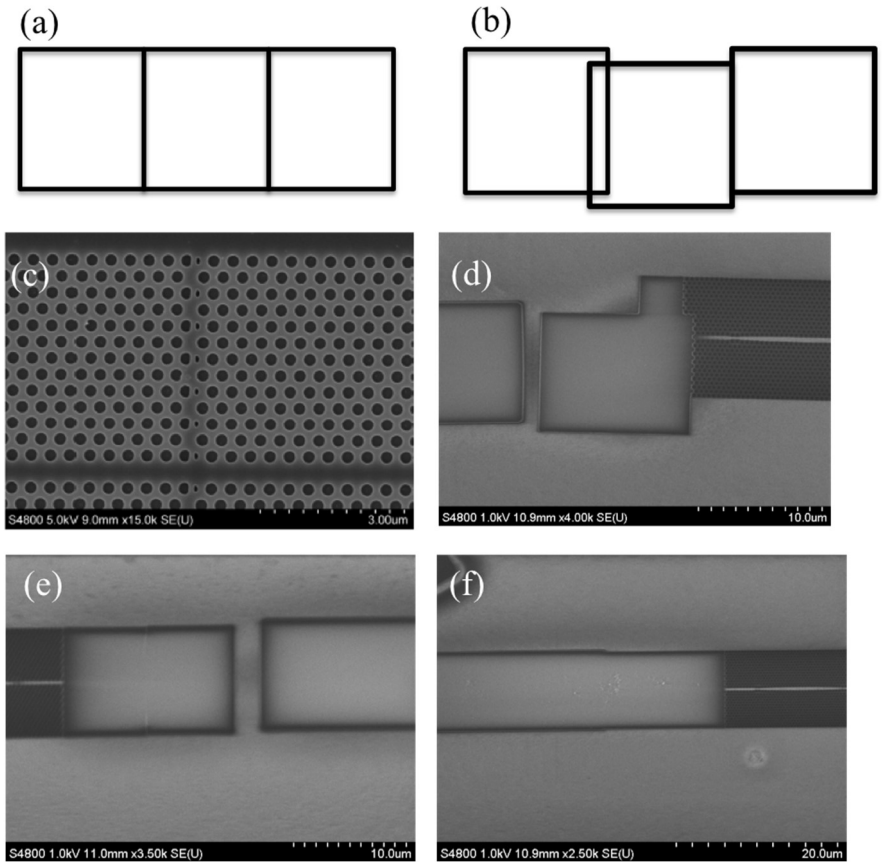

Fig 3.12 (a) shows relative positions of the writing fields with no stitching error. (b) represents overlapping and shifts in the writing fields. (c) SEM image of a stitching error leading to hole re-formation, due to a small gap between two writing fields. (d) and (e) SEM image of a stitching error in the trenching area, leading to the position shift and photonic crystal region broken. (f) SEM image of an optimize design of a long adjacent trench area. In this case, the stitching error can be avoided in the long trench exposure.

The stitching error can be minimized through an optimized design. In this work, the size of the photonic crystal used is $20\,\mu m \times 10\,\mu m$. Therefore, I am using the smallest writing field ($50\,\mu m \times 50\,\mu m^2$) to achieve the best resolution without stitching error happening. For writing the mm-long bus waveguide, the largest writing field ($200\,\mu m \times 200\,\mu m$) is used to minimize the number of stitching errors. In the trench exposure, I can use an appropriate design to avoid the stitching error, as shown in Fig 3.12 (f). A slight larger trench and a small overlap between the adjacent writing field for trench have been designed. The slight variations between

two trenches do not affect the device's performance, as the trench is covered with an oxide layer and no propagation mode is supported between the bus waveguide and the trench area [105].

3.7 Fabrication process

In previous sections, I have discussed the main fabrication tools and technique are used in this thesis. Oxide cladding technique and an engineered dispersion adapted photonic crystal cavity have been designed and applied to achieve a high quality factor in vertical coupling system. Specific fabrication process to an desired coupled cavities system is introduced in the following.

3.7.1 Coupled cavities system fabrication process

In order to study coupled resonators system, the device is fabricated based on silicon photonic crystal system. The device is fabricated on a silicon-on-insulator platform with 220 nm silicon layer on a 2 μm buried oxide layer. The fabrication steps are introduced as Fig. 3.13. The sample is spin coated with 300 nm thick e-beam photoresist ZEP-520A layer (Fig. 3.13 (b)). Using e-beam lithography, the photonic crystal cavities are defined in the ZEP-520A layer (Fig. 3.13 (c)) and the pattern is transferred into the silicon layer by reactive ion etching (RIE) (Fig. 3.13 (d)). the sample is cleaned with Piranha (3:1 H2SO4, H2O2) and then Acetone and IPA to remove the photoresist. The entire device is then covered with spin-on-glass (FO_x 14, Dow Corning) (Fig. 3.13 (e)). The oxide layer thickness is then reduced to 110 nm by RIE as shown in Fig. 3.13 (g). Then, the sample is spin coated with photoresist SU8 and then annealed for 1 minute at 100 °C (Fig. 3.13(h)). Therefore, the waveguide is defined on top of all cavities by

e-beam lithography. (Fig 3.13 (i)). Finally, the sample is cleaved to form optical facets for measurement using the end-fire technique.

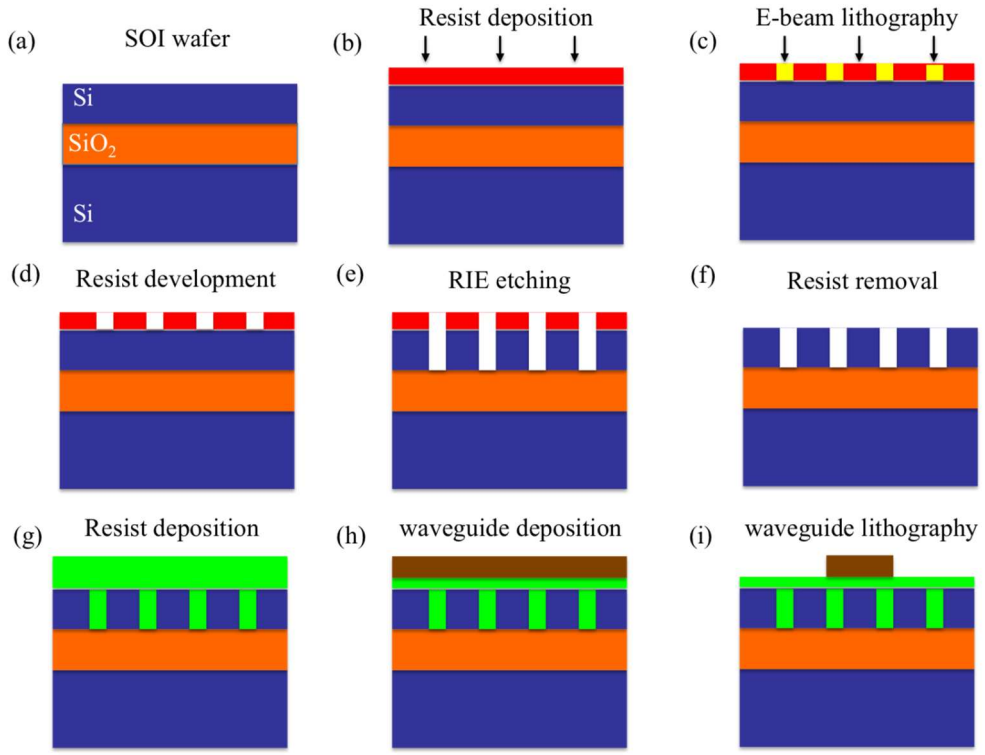

Fig. 3.13 Fabrication process: (a) A sample of SOI is cleaved from the wafer. (b) the sample is spin by photoresist. (c) and (d) Using e-beam lithography and dry etching, photonic crystal cavities are transferred to the silicon layer. (f) and (g) the sample is cleaned and spin by FO_x. (h) and (i) SU8 waveguide are fabricated by using e-beam lithography.

3.7.2 Coupled cavities system with thermal tuning patterns fabrication process

In order to tune the resonances wavelength of photonic crystal cavity, ohmic heat patterns have been applied into the fabrications. The fabrication process of the device shares the same as the section 3.7.1 before the ohmic heat pattern fabrication. The fabrication process presents in Fig 3.14. After the oxide layer has been deposited, I use lift-off procedure to fabricate metal pattern.

The substrate is spun with a 500 nm thick PMMA for the lithography to open metal evaporation window in Fig 3.14 (e). After the e-beam lithography, the sample is developed with a mixture of de-ionized H_2O and IPA (de-ionized H_2O : IPA= 3:7). The metal is then deposited on the substrate using EBPVD (Fig. 3.14 (f)). After the evaporation, the device is immersed in the acetone. PMMA is dissolved and the deposited materials from the undesired parts are removed (Fig 3.14 (g)). After cleaning with acetone and IPA, the sample is spin coated with photoresist SU8 and then annealed for 1 minute at 100 °C (Fig. 3.14 (h)). Therefore, the waveguide is defined on top of all cavities by e-beam lithography and finalized after a hard baking. (Fig 3.14 (i)). Finally, the sample is cleaved to form optical facets for measurement using the end-fire technique.

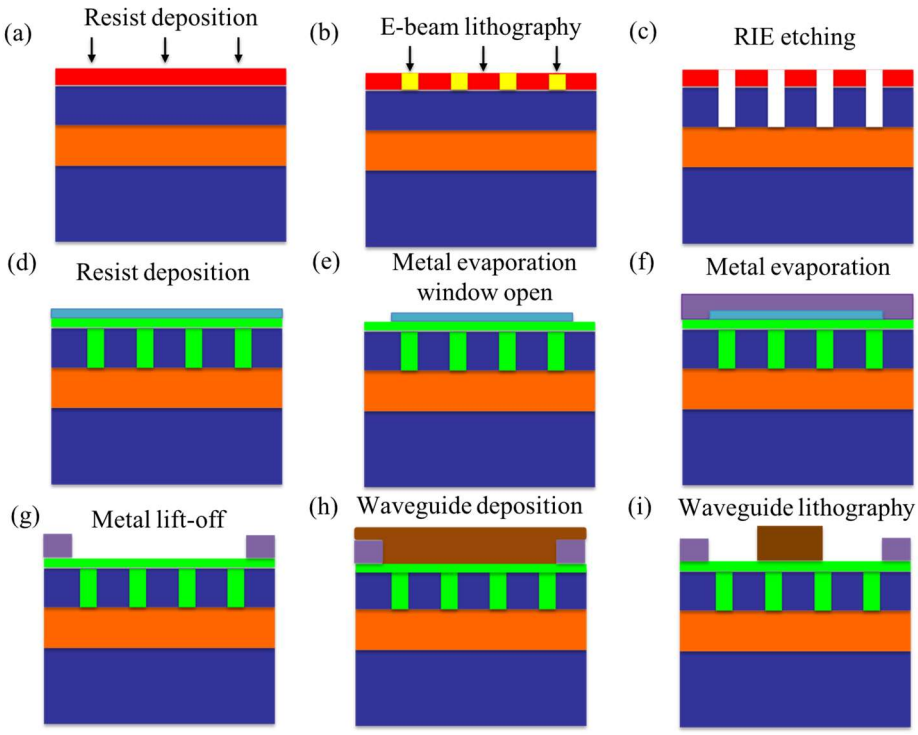

Fig 3.14 Fabrication process: A sample of SOI is cleaved from the wafer. (a) the sample is spin by photoresist. (b) and (c) photonic crystal cavities are transferred to the silicon layer using the e-beam lithography and dry etching. (d) the sample is cleaned and spin by FO_x and another resist layer (PMMA). (e)-(g) the lift-off procedures are processed to deposit thermal-heating pattern. (h) and (i) SU8 waveguide has been defined using e-beam lithography.

A SEM image of oxide cladding photonic crystal with a polymer bus waveguide has shown in Fig. 3.15 (a) and coupled cavities with thermal heating patternsare shown in Fig. 3.15 (b).

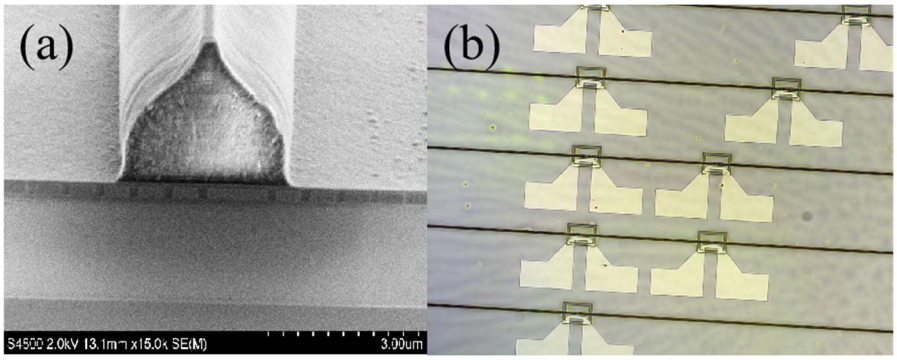

Fig 3.15 (a) SEM of a cross section of the vertical coupling system based on photonic crystal cavities. (b) Microscope image of thermal heating patterns in coupled cavities system.

3.8 Summary

In this chapter, I have introduced several fabrications technique and tools used in this thesis. Fabrication disorders have also been discussed from the state-of-art view. To accomplish a high quality factor cavity based on silicon photonic crystal structure has always been my goal in my PhD study. Besides, combining with oxide cladding technique, reducing our prorogation loss and keeping high integrated with CMOS can be achieved. Thus, a new platform for optical communication and applications has been realized. In the next chapter, I will theoretical discuss how to achieve EIT-like in coupled cavities system

Chapter 4 Theoretical approach: the optical analog to electromagnetically induced transparency in coupled resonators system

4.1 Introduction

In chapter 2, localized cavity modes achieved by defect effects in the photonic band gap region have been discussed. By lithographically tuning the geometric parameters, such as shifting the position, size of the hole and the lattice constant, high Q-modes can be achieved to allow controllable store and release light pulses in localized and standing wave modes, giving a slow light system. The inspiration for this work comes from previous research on stopped light in atomic gases using electromagnetically induced transparency (EIT) [21], in which light is captured in dark states of the atomic system via adiabatic tuning [22]. A common characteristic of a coupled quantum system is that the system's dynamics are determined by the competition between the joint coupling rate and the rate at which the coupled system decohere into the environment. Only "strong coupling" can overcome and indicate the effect of decoherence. Strong coupling occurs when the joint coupling rate becomes much faster than the rate of any competing dissipative process. One characteristic feature of strong coupling is energy level splitting. In strong coupling the extent of the resulting level splitting is known as vacuum Rabi splitting [22]. Classical analogs of EIT have already been demonstrated in systems of mechanical or electrical oscillators, where the quantum destructive interference is realized between excitation pathways to the upper level in three-level systems. However, the disadvantage of such atomic systems is that the narrow operating bandwidth and the operating

wavelengths are limited by the atomic resonances available. Since the EIT phenomenon results from resonant pathways, it has been recently theoretical and experimental realized in static optical resonators. For example, resonant tuning through a photonic crystal via the localized defect mode has been numerically analyzed [98], and experimental observed [99]. Additionally, a channel add-drop filter based on multiple coupled resonator systems in a photonic crystal was proposed [100, 104]. Under specific symmetry and degeneracy phase conditions, optical signals can be completely transferred from one waveguide to another one as a time reversal system. In the following, I will discuss different configurations of coupled resonators system to control slow light and the general condition to achieve the EIT analog. In this thesis, all configuration is weak coupling system.

4.2 Optical properties of coupled resonators system

4.2.1 General coupled mode theory formalism

In this project, a new coupling technique will be used to design to realise a new family of coupled optical resonators with a wide range of potential applications. Designs to slow light will be studied and the fundamental limits on the storage of light studied. By coupling many resonators together, better control over the flow of light can be achieved. This approach has the potential to realize low loss optical delay lines, an important functionality required in many photonic integrated circuits. Furthermore, in the following section, three configurations of coupled resonators system for potential slow light systems will be discussed. The interaction between resonators and waveguide will be theoretically studied based on coupled-mode theory (CMT) [101]. This section is organized as follows. Firstly, I briefly introduce CMT. In next, I utilize CMT to study these three generic configurations of coupled resonators system. The

propagation transmission and the corresponding phase shift are considered.

In CMT, an overall oscillating system can be described in terms of a set of weakly coupled components, each of which can be analyzed using general principles [101]. A cavity, for example, is treated as an oscillator in time. The modes of a cavity interact with the forward and backward propagating through the waveguide over a finite length decay equally. In this section, I consider a resonator that only supports a single mode, with amplitude denoted by a at the resonance frequency ω_0. $1/\tau_i$ and $1/\tau_w$ represent decay rates due to intrinsic loss and waveguide coupling, respectively. The intrinsic loss here represents the lowest loss limit which can be achieved, due to the loss in the absence of fabrication imperfections, and material processing. The decay rates are related to the quality factor, which $Q = \omega_0\tau/2$. Q_i and Q_w are corresponding to cavity quality factors of intrinsic loss and waveguide coupling loss. Q_t is total quality factor ($\frac{1}{Q_t} = \frac{1}{Q_w} + \frac{1}{Q_i}$) and S_i, S_r and S_t are given as the incident, reflective, and transmission waveguide amplitudes, which are normalized such that their squared values correspond to the incident, reflected and transmitted power, respectively. I use δ to normalize the frequency ω, which is defined by $\delta = (\omega - \omega_0)/\omega_0$ and $t = S_t/S_i$, $t = S_r/S_i$. Q_i represents the loss due to the leaky mode and the radiations in the cavity.Q_w denotes the cavity-waveguide coupling and is referred to as "waveguide coupling quality factor", whereas Q_c represents the cavity-cavity and is referred to as "cavity coupling quality factor", Note that in this section, I will follow these parameter settings.

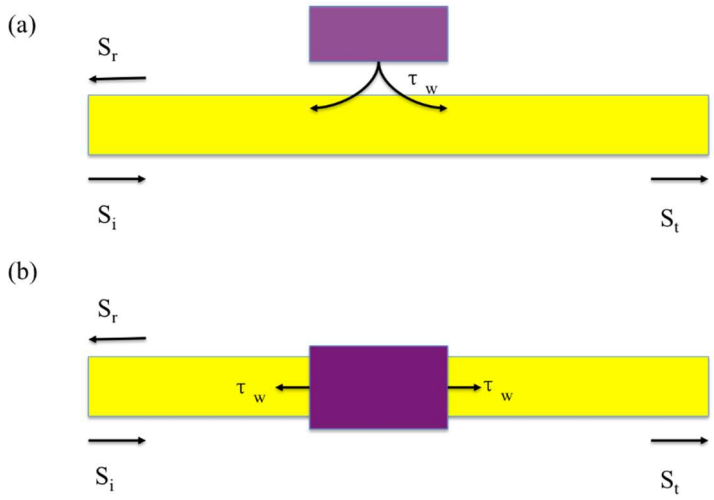

Fig. 4.1 Schematics of two coupled configuration with single cavities. (a) a single cavity with side coupling. (b) a single cavity with in-line coupling.

In Fig. 4.1, two configurations of a single cavity coupling with a waveguide are given. According to CMT, the transfer function can be given as $T = |t|^{2^2}$. Phase shift θ at given frequency is $\theta = \text{Arg}\,(t)$. Due to power conservation, the squared magnitudes are equal to the respective decay rates into the waveguide. Considering the lossless case, the equation for the evolution of the resonator mode in time is given by [101]

$$\frac{da}{dt} = \left(j\omega_0 - \frac{1}{\tau_i} - \frac{1}{\tau_w}\right) a + \sqrt{\frac{1}{\tau_i}} S_i \tag{4.1}$$

Here, j is the imaginary unit. From Eq. 4.1, the transfer function T and phase shift θ at given frequency can be inferred, inside coupling t_s and in-line coupling t_i configurations, respectively.

$$t_s = \frac{\frac{1}{Q_w}}{j2\delta + \frac{1}{Q_i} + \frac{1}{Q_w}} \tag{4.2}$$

$$t_i = \frac{j2\delta + \frac{1}{Q_i}}{j2\delta + \frac{1}{Q_i} + \frac{1}{Q_w}} \tag{4.3}$$

I assume the resonance wavelength is 1550 nm, and the corresponding quality factor is $Q_i = 10^5$, and $Q_w = 5 \times 10^4$. The assumed values are estimated from fabricated samples. According to Eq. 4.2 and 4.3, the transmission spectrum and the phase shift are plotted in Fig. 4.2. The red and blue curve represents the side and in-line coupling configurations, respectively. From Eq. 4.2 and 4.3 when $Q_i \gg Q_w$, the transmission is able to approach zero or unity respectively, corresponding with side coupling and in-line coupling. As a conclusion, a single resonator can realize a typical filter to storage and slow light pulse at the resonance frequency.

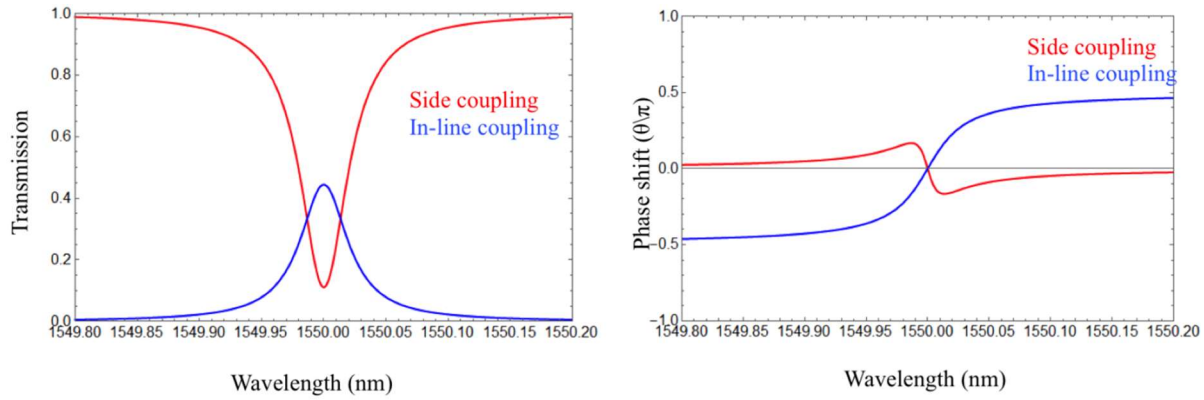

Fig. 4.2 Transmission and phase shift of a single cavity with side coupling and in-line coupling, respectively.

In the following section, I study three generic coupled resonators configurations as illustrated in Fig. 4.3. The cavities can be indirectly or directly coupled to one another depending on the configuration. In Fig. 4.3 (a) and (b), two resonators are directly coupled with waveguides, respectively. In Fig. 4.3 (c), since the resonators are indirectly coupled together through the propagating modes in the waveguide, I term the cavities as "one-side indirectly coupling", Similarly, the configuration of Fig 4.3 (a) is "one-side directly coupled" and Fig 4.3 (b) is "two-side directly coupled", In the following, I will discuss the three types of coupled resonators system in detail in terms of performance and practicality.

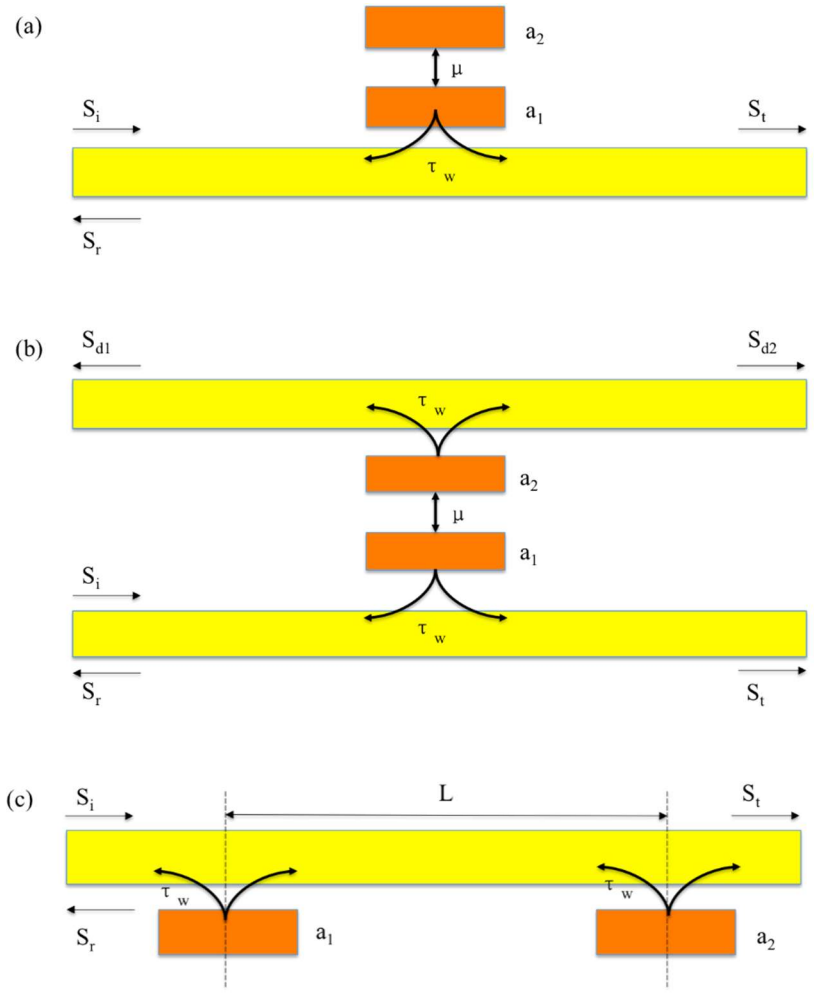

Fig. 4.3 Schematics of three generic coupled resonators coupling configurations. (a) one-side two resonators directly coupling with a waveguide; (b) two-side two resonators indirectly coupling with two waveguides; (c) one-side two cavities indirectly coupling with a waveguide

4.2.2 One-side directly coupled resonators system

As shown in Fig. 4.3 (a), the two resonators are directly coupled to one another, with the resonant frequency of each resonator a_1 and a_2 is ω_0 and the intrinsic quality factor is Q_{i1} and Q_{i2}. The coupling coefficient between two cavities modes is denoted by μ and is related to coupling quality factor by $Q_c = \omega_0/(2\mu)$. Assuming the waveguide-coupling occurs only for mode a_1, the equations for the evolution of the cavity mode with time are given by [7]:

$$\frac{d}{dt}a_1 = \left(j\omega_0 - \frac{1}{\tau_{i1}} - \frac{1}{\tau_w}\right)a_1 + \sqrt{\frac{1}{\tau_w}}S_i - j\mu a_2 \quad 4.4$$

$$\frac{d}{dt}a_2 = \left(j\omega_0 - \frac{1}{\tau_{i2}}\right)a_2 - j\mu a_1 \quad 4.5$$

Therefore, the transfer coefficient can be obtained as follows:

$$t = 1 - \frac{1}{Q_w}\frac{j2\delta + \frac{1}{Q_{i2}}}{\left(j2\delta + \frac{1}{2Q_{i1}} + \frac{1}{2Q_{i2}} + \frac{1}{2Q_w}\right)^2 + \left(\frac{1}{Q_c}\right)^2 - \left(\frac{1}{2Q_{i1}} - \frac{1}{2Q_{i2}} + \frac{1}{2Q_w}\right)^2} \quad 4.6$$

Based on Eq. 4.6, the mode splitting characteristics have been studied for different coupling coefficients in Table 1. Here $(\frac{1}{Q_0})^2 = |\left(\frac{1}{Q_c}\right)^2 - [\frac{1}{2Q_{i1}} - \frac{1}{2Q_{i2}} + \frac{1}{2Q_w}]^2|$.

Coupling condition	Resonant frequency	Intrinsic quality factor	Waveguide coupling quality factor
$\frac{1}{Q_c} > \frac{1}{2Q_{i1}} - \frac{1}{2Q_{i2}} + \frac{1}{2Q_w}$	$\omega_0 \pm \frac{\omega_0}{2Q_0}$	$\frac{2Q_{i1}Q_{i2}}{Q_{i1}+Q_{i2}}$	$2Q_w$
$\frac{1}{Q_c} < \frac{1}{2Q_{i1}} - \frac{1}{2Q_{i2}} + \frac{1}{2Q_w}$	ω_0	$\frac{2Q_{i1}Q_{i2}}{Q_{i1}+Q_{i2}}$	$\frac{2Q_wQ_0}{Q_0 \pm 2Q_w}$
$\frac{1}{Q_c} = \frac{1}{2Q_{i1}} - \frac{1}{2Q_{i2}} + \frac{1}{2Q_w}$	ω_0	$\frac{2Q_{i1}Q_{i2}}{Q_{i1}+Q_{i2}}$	$2Q_w$

Table 4.1. Mode-splitting characteristic for different coupling strengths

The mode-splitting depends greatly on the coupling strength can be observed. When $\frac{1}{Q_c} > \frac{1}{2Q_{i1}} - \frac{1}{2Q_{i2}} + \frac{1}{2Q_w}$, the mode a_1 and a_2 split into $\omega_0 \pm \frac{\omega_0}{2Q_0}$, while the intrinsic quality factor and the waveguide coupling quality factor are the same. When $\frac{1}{Q_c} < \frac{1}{2Q_{i1}} - \frac{1}{2Q_{i2}} + \frac{1}{2Q_w}$, the

resonant frequency of the two split modes are still ω_0, but the waveguide coupling quality factor is $\frac{2Q_wQ_0}{Q_0 \pm 2Q_w}$. When $\frac{1}{Q_c} = \frac{1}{2Q_{i1}} - \frac{1}{2Q_{i2}} + \frac{1}{2Q_w}$, the two split mode are degenerate, with the same resonance frequency, intrinsic quality factor and waveguide coupling quality factor.

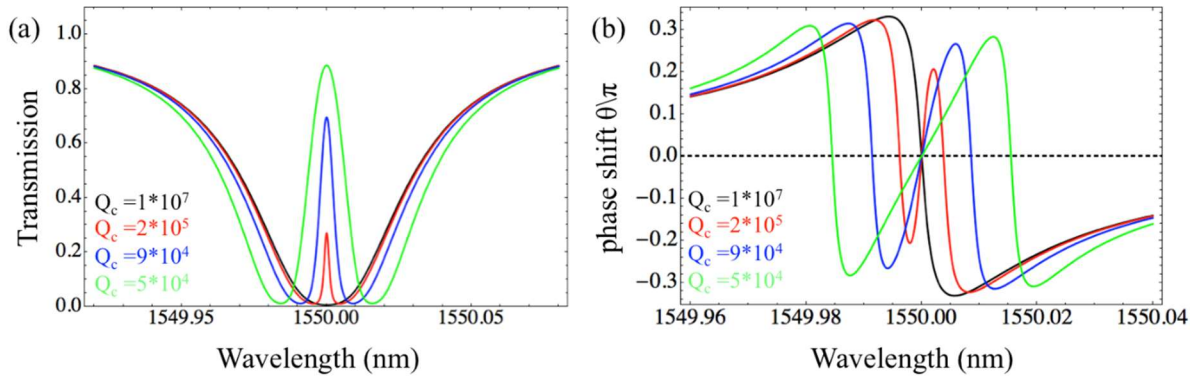

Fig 4.4 Illustrations of the transmission (a) and phase shift (b) for one-side directly coupling configuration. Q_{i1} is 5×10^5, Q_{i1} is 10^6, and Q_w is 4×10^4. Four recipes of Q_c (10^7, 2×10^5, 9×10^4, 5×10^4) are represented as black, red, blue, and green curves, respectively.

The resulting theoretical transmission spectra and phase shifts are plotted in Fig. 4.4. Fig 4.4 (a) presents the EIT-like transmission appears. Recalling the EIT equation from Ref [101], $T_{ab} = \Omega_1^2 \Gamma \Delta^2 / [\Delta^2 \Gamma^2 + 4(\Delta^2 - {\Omega_2^2}/{4})^2]$, where Ω_1 and Ω_2 are respective Rabi frequencies of probe field and pump field, Γ is decay rate and Δ is detuning of probe field from atomic resonance. It can be seen that Eq 4.6 is identical to the EIT equation if considering $\omega_0 \delta \to \Delta$, $\omega_0/Q_{i1} + \omega_0/Q_w \to \Gamma$, $\omega_0/Q_c \to \Omega_2$. Therefore, the EIT-like transmission is a special case of mode-splitting due to the coupling between cavity modes. When the cavity coupling coefficient is increased, the EIT-like resonance becomes obvious and the transmission at ω_0

approaches 1. No complete transparency is achieved due to the loss of mode a_2 here.

4.2.3 Two-side directly coupled resonators system

In this section, the two-side directly coupling resonators system will be discussed as illustrated in Fig. 4.3 (b). The waveguide is positioned symmetrically between the two resonators (a_1 and a_2). I assume that the light firstly propagates through the bottom bus waveguide, then coupled into the cavity a_1. Considering two cavity modes with the same intrinsic Q_i coupled to the waveguide, the equation of fields a_1 and a_2 can be described from the CMT:

$$\frac{d}{dt}a_1 = \left(j\omega_0 - \frac{1}{\tau_{i1}} - \frac{1}{\tau_w}\right)a_1 + \sqrt{\frac{1}{\tau_w}}S_i - j\mu a_2 \tag{4.7}$$

$$\frac{d}{dt}a_2 = \left(j\omega_0 - \frac{1}{\tau_{i2}} - \frac{1}{\tau_w}\right)a_2 - j\mu a_1 \tag{4.8}$$

Therefore, the transfer functions of each port are represented as, including port t, port d_1, port d_2, respectively:

$$t = 1 - \frac{1}{2Q_w}\left(\frac{1}{j\left(2\delta + \frac{1}{Q_c}\right) + \frac{1}{Q_i} + \frac{1}{Q_w}} + \frac{1}{j\left(2\delta - \frac{1}{Q_c}\right) + \frac{1}{Q_i} + \frac{1}{Q_w}}\right) \tag{4.9}$$

$$r = \frac{1}{2Q_w}\left(\frac{1}{j\left(2\delta + \frac{1}{Q_c}\right) + \frac{1}{Q_i} + \frac{1}{Q_w}} + \frac{1}{j\left(2\delta - \frac{1}{Q_c}\right) + \frac{1}{Q_i} + \frac{1}{Q_w}}\right) \tag{4.10}$$

$$t_{d1} = t_{d2} = -\frac{1}{2Q_w}\left(\frac{1}{j\left(2\delta + \frac{1}{Q_c}\right) + \frac{1}{Q_i} + \frac{1}{Q_w}} - \frac{1}{j\left(2\delta - \frac{1}{Q_c}\right) + \frac{1}{Q_i} + \frac{1}{Q_w}}\right) \tag{4.11}$$

where the cavity coupling coefficient Q_c is equal to $\omega_0/(2\mu)$. Based on Eq. 4.9, the two modes with ω_0 are split into two modes, which is $\omega_0 \pm \frac{\omega_0}{2Q_c}$. The waveguide coupling quality factor for the two split modes remains Q_w. The separation of the two split modes is only determined by Q_c for a fixed ω_0. The transfer functions and phase shift for each port are plotted in Fig. 4.5,

respectively. The transmission spectrums of S_t and S_{d1} (S_{d2}) present in Fig. 4.5 (a) and (d), respectively. In Fig. 4.5 (b), the phase shift shows the dispersion at the two splitting modes in the transmission. From Fig. 4.5 (a), decreasing Q_c reduces the depth of resonance notch and further lifts the mode-splitting can be seen. The splitting in the transmission can be seen clearly as Q_c decreases, however the two mode-splitting in the transmission still keeps anomalous as shown in Fig 4.5 (c).

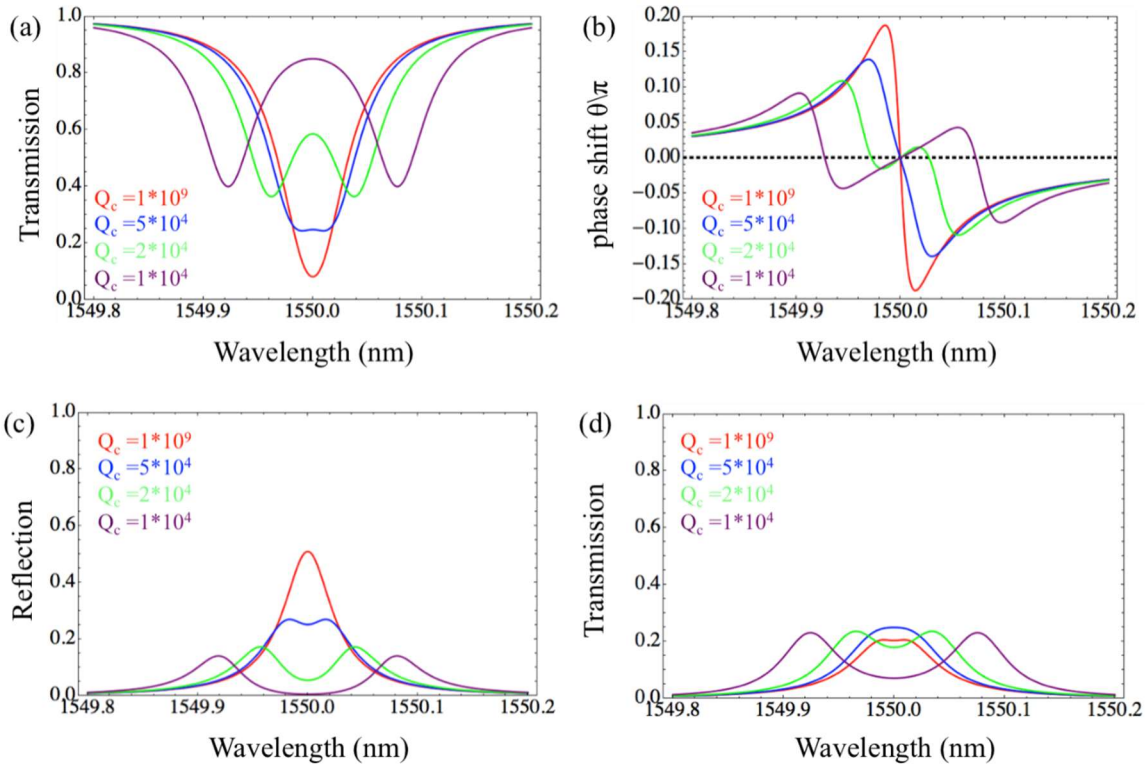

Fig. 4.5 The transmission spectrum of S_t, phase shift of S_t, the reflection spectrum of S_r, and the transmission spectrum of S_{d1} (S_{d2}) for different Q_c, with $Q_i = 10^5$ and $Q_w = 4 \times 10^4$ are shown in (a), (b), (c) and (d).

The mode splitting occurs as long as coupling exists, however the mode-splitting in the transmission spectrum is not always visible. This is because that the overall transmission is determined by the superposition of the two split modes with different amplitudes and phases.

Here the two splitting can be seen in the transmission only when the coupling is large enough.

4.2.4 One-side indirectly coupled resonators system

In this section, I analyze two cavity modes coupled through the waveguide. The large inter-cavity distance, L, which allows us to ignore the direct coupling between the resonators as in Fig. 4.3 (c). Assuming two degenerate cavities with amplitude a_1 and a_2 and the intrinsic resonance frequency are both ω_0. The corresponding intrinsic quality factors and waveguide quality factor are $Q_i$and Q_w. Assuming a phase shift ϕ between two resonators, the equations for the evolution of the cavity mode with time can be given as:

$$\frac{d}{dt}a_1 = \left(j\omega_0 - \frac{1}{\tau_i} - \frac{1}{\tau_w}\right)a_1 + \sqrt{\frac{1}{\tau_w}}S_i + \sqrt{\frac{1}{\tau_w}}(-e^{j\phi}\sqrt{\frac{1}{\tau_w}}a_2) \quad 4.12$$

$$\frac{d}{dt}a_2 = \left(j\omega_0 - \frac{1}{\tau_i} - \frac{1}{\tau_w}\right)a_2 + \sqrt{\frac{1}{\tau_w}}S_i + \sqrt{\frac{1}{\tau_w}}(-e^{j\phi}\sqrt{\frac{1}{\tau_w}}a_1) \quad 4.13$$

where $S_i = e^{-j\emptyset}(S_r - \sqrt{\frac{1}{\tau_w}}a)$, based on the power conservation. Thus, the transfer coefficient can be expressed as:

$$t = e^{j\phi}\frac{(1-\gamma_0)^2}{1-\gamma_0^2 e^{2j}} \quad 4.14$$

$$r = \frac{-\gamma_0 - \gamma_0 e^{2j\phi} + 2\gamma_0^2 e^{2j\phi}}{1-\gamma_0^2 e^{2j\phi}} \quad 4.15$$

where $\gamma_0 = -1/[2Q_w(j\delta + \frac{1}{2Q_i} + \frac{1)}{2Q_w})]$. δ is a normalized frequency, which is $\frac{\omega-\omega_0}{\omega_0}$. γ is the transfer function of the reflection port for a single indirectly coupling cavity. Therefore, the Fabry-Perot resonance exists between two cavities through the propagating mode in the waveguide. When $\phi = m\pi$ (m is an integer), the two modes a_1 and $a_2$can be regarded as one

mode with the waveguide coupling quality factor $Q_w/2$; when $\phi = (m + \frac{1}{2})\pi$, the indirectly coupling a waveguide leads to mode splitting and the frequencies of the two split modes are $\omega_0 \pm \frac{\omega_0 sin\phi}{2Q_w}$, and meanwhile the waveguide coupling quality factors for the two modes are still remains as Q_w; when $\phi \neq m\frac{\pi}{2}$, the waveguide coupling quality factor of two resonators changes to $\frac{Q_w}{1 \pm cos\phi}$, with corresponding splitting mode frequencies $\omega_0 \mp \frac{\omega_0 sin\phi}{2Q_w}$, respectively. The mode-splitting is asymmetric, due to different waveguide coupling factors and resonator frequencies of the two split modes. According to Eq. 4.14, the corresponding transmission spectrum is plotted in Fig. 4.6. The transmission spectrum shows an Fano-like transmission spectrum, when $\phi \neq m\pi$.

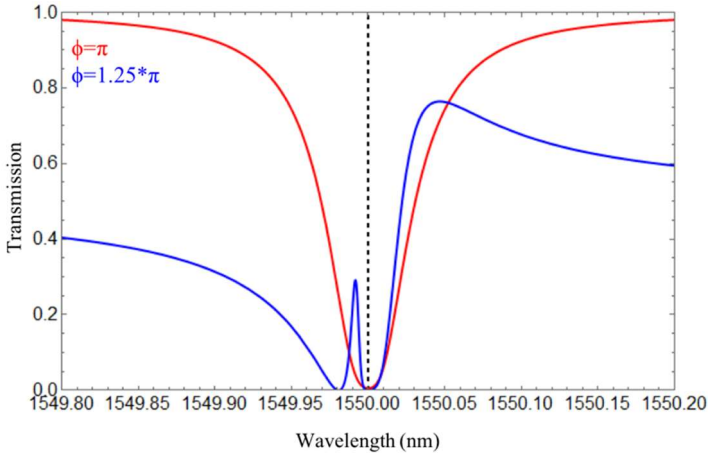

Fig. 4.6 Transmission spectrum for one-side directly coupled resonators system S_t port, which ω_0 = 1550 nm, Q_i is 5×10^5 and Q_w is 8×10^4. The different phase shift $\phi = n\pi$ with n=1 (Red curve), 1.25 (Blue curve) are shown.

If the two modes are at ω_1 and ω_2, an EIT-like spectrum can also be obtained, which will be discussed in detail in the following section. And this has been demonstrated in both ring resonators [103] and PhC cavities [104] in the previous sections. Here, I compared this kind of

EIT-like transmission with the EIT-like transmission between two degenerate modes shown in the section 4.2.2. When $\frac{1}{\tau_i} \ll |\omega_1 - \omega_2| \ll \frac{1}{\tau_w}$ and $\phi = -m\pi$, the transmission $T = |t|^2$ is given as $T = 1 - \frac{\delta^2/Q_w^2}{\delta^2/Q_w^2 + (\delta^2 - (\Delta\omega/(2\omega_0))^2)^2}$, where $\omega_0 = \frac{\omega_1 + \omega_2}{2}$, $\Delta\omega = (\omega_1 - \omega_2)$ and $Q_i \to \infty$ is assumed. Regarding $\omega_0\delta \to \Delta$, $\frac{\omega_0}{Q_w} \to \Gamma$ and $\Delta\omega \to \Omega$, comparing with EIT equation in the section 4.2.2, the EIT identify resonance is at ω_0. When $\omega = \omega_0$, the transmission of EIT peak reaches a maximum. In conclusion, I have analyzed three configurations of coupled resonators system based on the temporal CMT. Both the direct coupling and indirect coupling through waveguide can lead to EIT-like transmission appears. For two directly coupled resonators configurations, the two split modes can be controlled by cavities coupling quality factor and waveguide coupling quality factor. For the indirectly coupled resonators configuration, the separation between the two split modes is controlled by the phase shift introduced by the waveguide. This research will be useful for the design of cavity-based devices for integration in nanophotonics, either to mitigate the crosstalk due to the coupling between cavities in densely packed photonics chips or to optimize the coupling between cavities for designing new functional photonics devices. In the next, I will explore further the coupled cavities system, which can achieve analogue to EIT-like system. Due to the greater ease of fabrication, I will focus on the configuration shown in Fig. 4.3 (c) and explore how light can be slowed in the system. In the following section, I will use transfer matrix method to study the band structure in coupled resonator system.

4.3 Slow light in coupled resonators system

4.3.1 The delay-bandwidth product filter

The fundamental limitation in optical resonator systems is the delay bandwidth product, which means that the group delay is inversely proportional to the bandwidth. Thus, for a given resonance, the total phase shift ϕ across the resonance frequency is $m\pi$, and m is the order of the resonance. Therefore, I have the following constraint regarding the group delay $\delta t = \frac{d\phi}{d\omega}$:

$$\int d\omega \delta t = \int d\omega \frac{d\phi}{d\omega} = m\pi \tag{4.16}$$

Thus, the minimum group velocity through a resonator is:

$$v_g \approx \frac{L}{\delta\tau} = \frac{L\delta\omega}{m\pi} \tag{4.17}$$

Where L is the physical length of a resonator, and τ is the decay time of the resonator. The group velocity that can be achieved in a static system scales linearly with the system bandwidth and the physical dimensions of the resonators. Thus, the group velocity cannot reach to zero for the entire signal bandwidth unless the signal bandwidth is zero.

In order to study the bandwidth of the coupled resonators system, the transfer matrix method is used. Here I consider a waveguide is coupled to two side resonators in each unit cell, as shown in Fig. 4.7. The resonators have resonance frequency ω_a and ω_b, respectively.

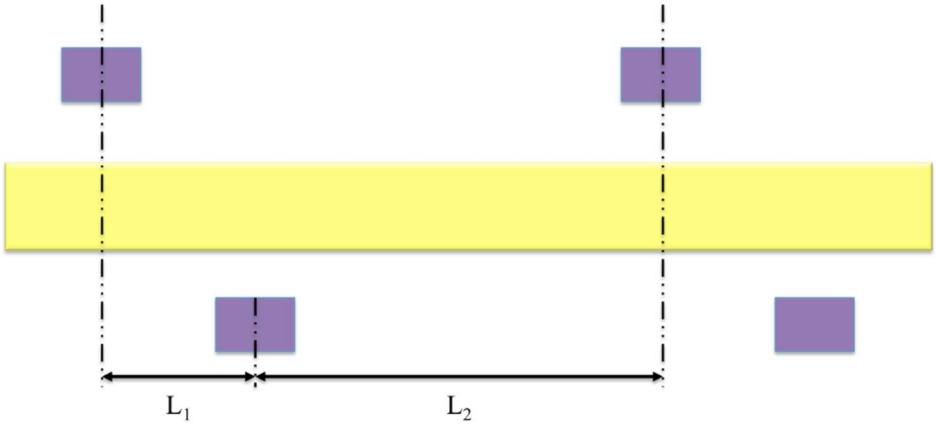

Fig 4.7 Schematic of the coupled resonators system used to slow light. The smaller rectangles represent the cavities, others correspond to the waveguide. The distance between the nearest neighbor side cavities is l_1, and the length of the unit cell is $l = l_1 + l_2$

Using the transfer matrix method [165], I can calculate matrices for each layer, and therefore obtain a total transmission for the matrix method. Thus, the transmission coefficient at an angular frequency ω for a single resonator can be calculated as,

$$T_{C_i} = \begin{pmatrix} 1 + j/(\omega - \omega_i)\tau & j/(\omega - \omega_i)\tau \\ -j/(\omega - \omega_i)\tau & 1 - j/(\omega - \omega_i)\tau \end{pmatrix} \quad 4.18$$

where the cavities couple to the waveguide efficiency is $1/\tau$, and the resonance frequency is ω_i. And the transfer matrix of a waveguide section is

$$T_l = \begin{pmatrix} e^{-j\beta l} & 0 \\ 0 & e^{j\beta l} \end{pmatrix} \quad 4.19$$

Where l is the physical length of a waveguide unit between two coupled resonators and β is the wavevector of the waveguide at a given frequency ω. Thus, The transfer matrix of an entire unit cell in Fig 4.7 can be described a s

$$T = T_{C_1} T_{l_1} T_{C_2} T_{l_2} \quad 4.20$$

Since $det(T) = 1$, the eigenvalues of T can be represented as e^{-ikl}, e^{ikl}, l is the length of the

unit cell, which is equal to l_1+l_2, and $\boldsymbol{k}$ corresponds to the Bloch wavevector of the entire system. Therefore, requiring the determinant to vanish for non-trivial solutions, we get the band diagram of the system can be obtained [165] as

$$\frac{1}{2}Tr[T] = \cos(kl) = f(\omega) \equiv \cos(\beta l) + \frac{C_+}{(\omega-\omega_a)} + \frac{C_-}{(\omega-\omega_b)} \qquad 4.21$$

where $C_\pm = \frac{2Sin(\beta l_1)Sin(\beta l_2)}{(\omega_a-\omega_b)\tau^2} \pm \frac{Sin(\beta l)}{\tau}$. In the frequency range, where $|f(\omega)| < 1$, the system supports a propagating mode, while $|f(\omega)| > 1$ corresponds to the frequency range of the photonics band gaps. For frequency separation $\Delta = |\omega_a - \omega_b|\tau$, the band diagram is shown in Fig 4.8. For a large frequency separation as shown in Fig. 4.8 (a), in the vicinity of the resonances, the system supports three photonic bands, with two gaps occurring around ω_a and ω_b, which is similar to the band diagram of an EIT system. The width of the middle band depends on the coupling different frequency separation $\Delta = |\omega_a - \omega_b|\tau$. When the resonance frequencies satisfy the following conditions, the width of the middle band approaches at zero as shown in Fig. 4.8 (b), with the frequency of the entire band pinned at ω_a:

$$C_+(\omega_a) = \frac{2Sin[\beta(\omega_a)l_1]Sin[\beta(\omega_a)l_2]}{(\omega_a-\omega_b)\tau^2} + \frac{Sin[\beta(\omega_a)l]}{\tau} \to 0 \qquad 4.22$$

$$\left|\cos[\beta(\omega_a)l] + \frac{C_-(\omega_a)}{(\omega_a-\omega_b)}\right| > 1 \qquad 4.23$$

Alternatively, the band can be pinned at ω_b with a similar condition. To demonstrate these conditions, I note that in Eq. 4.21 has a singularity at $\omega = \omega_a$. The frequency width of this singularity is controlled by $C_+(\omega_a)$, and approaches zero when Eq. 4.22 is satisfied. Satisfying Eq.4.23, the solution to $|f(\omega)| \leq 1$ in the vicinity of ω_a occurs on the same branch of the singularity $1/(\omega - \omega_a)$ and therefore forms a continuous band. When both conditions are satisfied, as the width of the singularity approaches zero, the middle band in Fig 4.8 (b) are always exists in the vicinity of ω_a, and the width of the middle band reduces. When

decreasing Δ, the group velocity changes sign. Using the second band can be applied to slow a light pulse. Therefore, the sign of the group velocity for the middle band can be designed by choosing l_1, l_2.

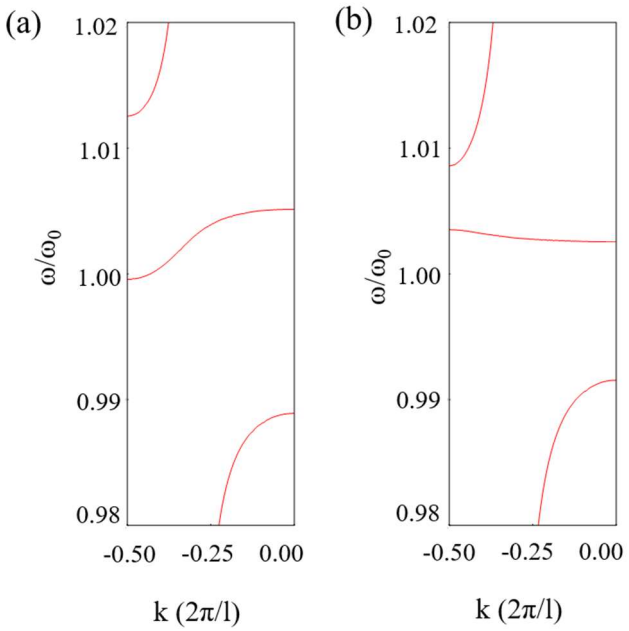

Fig 4.8 The band diagram of coupled resonators system for two different Δ= $|\omega - \omega_A|\tau$. (a) Δ= 3 The bandwidth of the middle band is large. (b) Δ= 0.3 The bandwidth of the middle band is reduced, and light has been slowed down

Furthermore, using the transfer matrix method [165], the transmission spectra can be calculated to better explain the system's properties. The transmission spectrum can be written as,

$$|T(\lambda)|^2 = \left(\frac{|t_a t_b|}{1-|r_a r_b|}\right)^2 \frac{1}{1+4\left(\frac{\sqrt{|t_a t_b|}}{1-|r_a r_b|}\right)^2 Sin^2(\theta)} \qquad 4.24$$

Where t_a and t_b are transmission matrix coefficients for two resonators, respectively, given by

$$t_{A,B} = \frac{j(\omega-\omega_{A,B})+\gamma}{j(\omega-\omega_{A,B})+\gamma_c+\gamma} \qquad 4.25$$

Where γ is the amplitude radiative-loss rate, related to the radiate quality factor as $\gamma = \frac{\pi c}{Q_{rad}\lambda_0}$. γ_c is the total waveguide-resonator coupling rate due to decay into both two sides cavities as $\gamma_c = \frac{\pi c}{Q_{rad}\lambda_0}$, and θ is one half the round-trip phase accumulated in the waveguides: $\theta = \frac{1}{2}Arg\left[r_a r_b e^{-2j\beta(\omega)L_1}\right]$, where $\beta(\omega)$ is the waveguide dispersion equation. Given the specific parameters of the system, the transmission spectrum is presented in Fig 4.9. The width of the middle peak (EIT peak) depends on the distance l between two resonators, which is the phase spacing between the resonances. When the condition $2\beta(\omega_0)l = 2n\pi$ is satisfied, the EIT peak is located at ω_0. Similar to a Fabry-Perot cavity, when the round-trip phase is 2π, the resulting EIT transmission exhibits a narrow, symmetric peak and bring a larger group delay with a narrower bandwidth, as presents in Fig 4.9. As the two cavities shift away from each other, a broadened, asymmetric peak appears. Thus, changing l makes the EIT peak gradually decay. If the resonator is lossless, the EIT peak can be tuned to an arbitrarily narrow bandwidth. Thus, the two sides coupled cavities can be designed to a tunable bandwidth filter, and moreover, can be adjusted by an order of magnitude with small refractive index modulation.

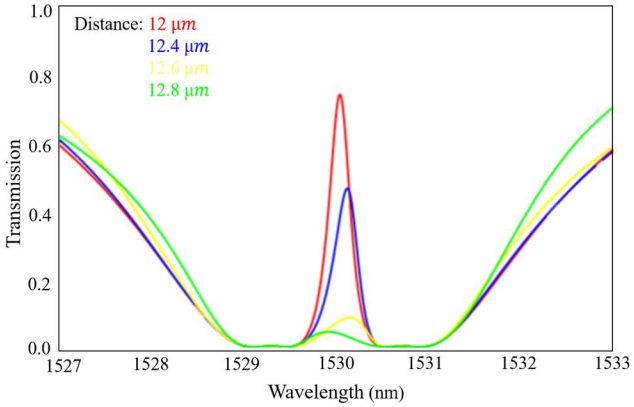

Fig 4.9 Theoretical calculated EIT-like transmission spectrums are plotted. Varied separations of L1 are presented, respectively, which correspond to Red 12 μm (32.5 π), Blue 12.4 μm (32.7 π), Yellow 12.6 μm (32.8 π), Green 12.8 μm (32.9π).

4.3.2 Finite Element Method demonstrations of the EIT analog

After studying the band diagram and the EIT-like transmission properties of the coupled resonators system, an all-optical analogue to EIT in coupled cavities system have been demonstrated. To study further how light can be trapped in a coupled resonators system, two-dimensional triangular-lattice photonic crystal structures were simulated as illustrated in Fig 4.10. According to the previous discussion about the defect mode on photonic crystal in Chapter 2 [105], I choose the L3 cavity and the cavity has been optimized to obtain a high-quality factor reaching at 60000. The period of photonic crystal region is 420 nm, and the radius is 0.29*Period. The cavity regions have been engineered to characterized at two resonator frequencies ω_a (194.730 THz) and ω_b (194.677 THz) with different periods of cavities regions at 420 nm and 420.05 nm, respectively. Silicon's refractive index sets as 3.47. the coupled photonic crystal cavities are coupling into a W1 PhC waveguide. The perfect matched layer (PML) and scattering boundary condition are applied to absorb unnecessary reflections. Due to the limited computing performance of the simulation workstation, numbers of photonic crystal arrays have been reduced, and mesh of the simulation structures set to coarse to shorten the simulation time. Thus, the intrinsic quality factor is much lower compared with the theoretical result. Therefore, the total transmission intensity is much lower than the theoretical calculation result, and the EIT-like transmission spectrum cannot achieve total transparency, as shown in Fig 4.11

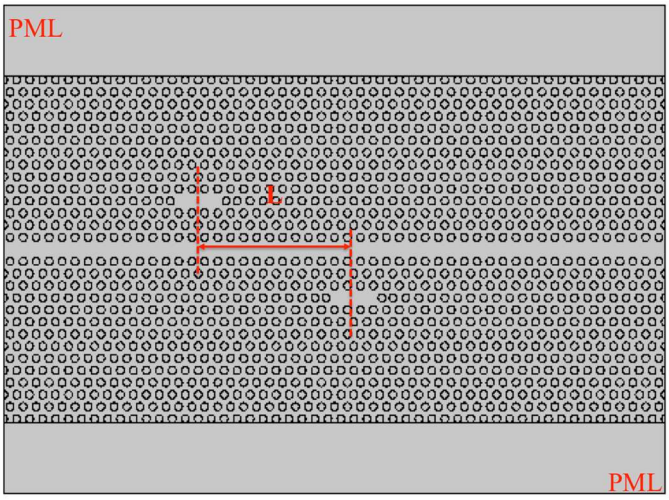

Fig 4.10 Schematics of two resonators indirectly coupling simulation geometry structures. The distance between two-side L3 cavities is defined as *L*.

As has been noted in section 4.2.4 and 4.3.1, when the phase shift difference between two resonators is $m\pi$, the EIT-like transmission peak appears. The EIT-like transmission peak decay with changing phase shift and vanish when the phase shift difference between two resonators is $(m+\frac{1}{2})\pi$, as shown in Fig 4.11. By changing the distance between two resonators leads to the phase shift difference changing between two resonators.

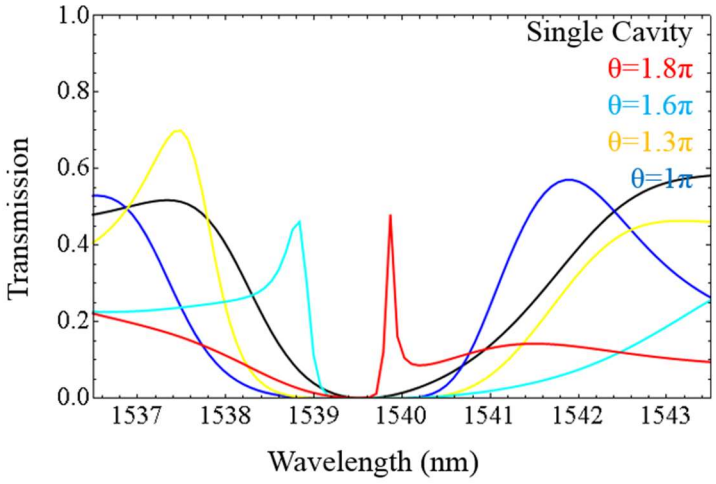

Fig 4.11 Transmission spectrums of in-plane L3 cavities indirectly coupled

One example of the electric field profiles $|E_y|$ of EIT like transmission configurations is shown in Fig. 4.12. The resonance frequency of the upper cavity and the lower cavity is ω_a and ω_b, respectively. In Fig. 4.12 (a), the upper cavity has been excited when the input pulse source frequency sets as ω_a. Consequently, the light has been mainly stored in the upper cavity, and only a small amount of light pass through the system. The system presents a low transmission. When the frequency of the input pulse source is tuned to the EIT resonance frequency range in Fig. 4.12 (b) and (c), the light is strongly confined between two coupled cavities and the waveguide. Thus, the system shows a high transmission property between those EIT frequencies ranges. Continuing to change the frequency of the input pulse source reaches at the resonance frequency ω_b of the lower cavity, the light passes through the upper cavity and the waveguide, then couples into the lower cavity and ends to store in the lower cavity, as shown in Fig 4.12 (d). Thus, the system changes to a low transmission property. Through those simulations, the changing of an EIT-like transmission process has been presented. The light has been mainly stored between two coupled cavities and the waveguide when EIT-like transmission property happens. Thus, a high quality factor cavity and a low propagation loss waveguide are both desired to achieve a good optical delay system.

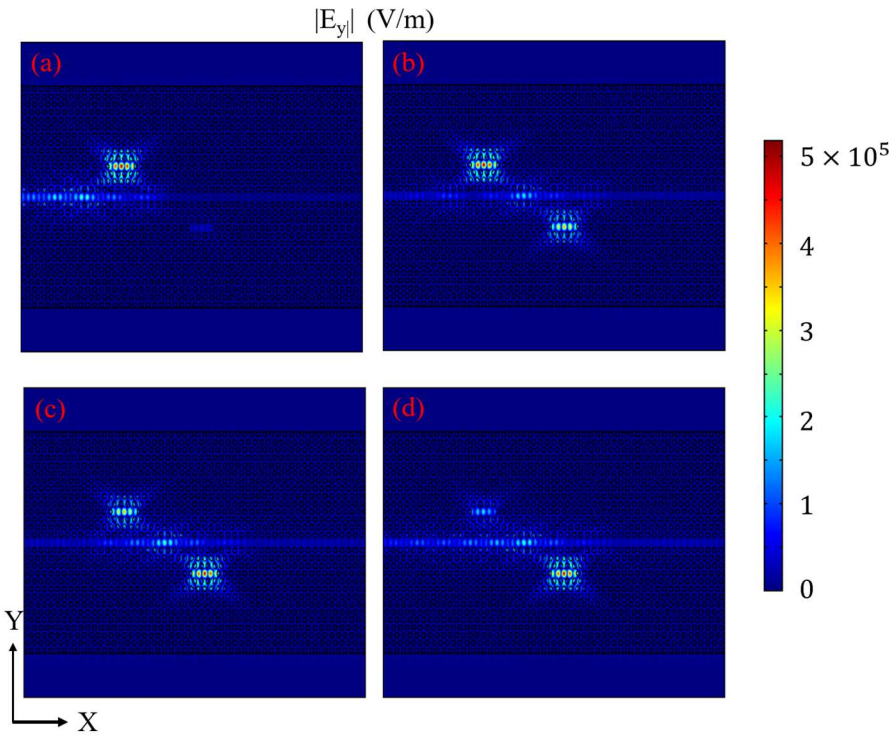

Fig 4.12 (a) Electric field $|E_y|$ profiles of the uppercavity at ω_a (194.730 THz); the upper cavity has been excited (b) and (c) EIT-like peak resonance at 194.697 THz and 194.687 THz, respectively; The light stores between two coupled cavities and the waveguide. (d) Electric field $|E_y|$ profiles of the lowercavity at ω_b (194.677 THz); the light stores at the lower cavity

4.4 Conclusion

In conclusion, the mode-splitting in three configurations of coupled resonators system are numerically analyzed based on CMT and also demonstrated by FEM. Both indirect and direct coupling between resonators and the waveguide can achieve EIT-like resonance. This study is useful for the design of in-plane cavities and vertical coupling cavities devices for integrated photonics communication. It gives a broaden potential area to nonlinear light applications, such as optical bistability, four waves mixing, and harmonic generation. In the following, I will experimentally study two resonators indirectly coupling configurations.

Chapter 5 Tunable optical buffer through an optical analog to EIT in coupled photonic crystal cavities

5.1 Introduction

As I described in the Chapter 4, the coupled resonators system is capable of achieving the analog to EIT when the phase shift and resonance frequency difference between the coupled resonators are satisfied with certain conditions. In this chapter, I present a novel approach to an optical analog to EIT with phase shift controlling and tuning of group delay using two coupled cavities. Here, I combine low loss polymer waveguides with photonic crystal dispersion adapted (DA) cavities [105] and results in large and dynamically controllable optical delay, similar to Xu et al [103]. Our system has the important difference in that the light spends a significant percentage of the time traveling in T polymer waveguide, which has lower propagation loss relative to silicon nanowires, resulting in reduced total loss compared to other on-chip optical delay lines. The use of polymer waveguides also increases the coupling efficiency to optical fibers, and the fiber to fiber loss of our system can be less than 3 dB. Specifically, I demonstrate delays as large as 300 ps, delay tuning exceeding 120 ps and record low optical losses of approximately 15 dB/ns. Thus, I divide this chapter into two parts. The first part introduces all optical analog to EIT in two coupled photonic crystal cavities with phase shift controlling. The other part will introduce controllable tuning in optical analog to EIT in coupled photonic crystal cavities by using thermal-optical tuning.

5.2 All optical analog to EIT in coupled photonic crystal cavities with Phase shift controlling

5.2.1 Devices design

As described in Chapter 4.3.1, The properties of EIT-like transmission in coupled cavities system is strongly controlled by the phased shift of two coupled cavities, which is determined by the distance between two coupled cavities. Therefore, I design three different inter cavity distances, as shown in Fig. 5.1 (a). The photonic crystal is embedded into a thin oxide layer and a SU8 polymer waveguide is placed vertically on the top of the cavity. The cavity design considered here is the DA cavity [105], as shown in Fig. 5.1 (b). Although this kind of the cavity does not offer a high FSR, I use it here because of its large fabrication tolerance, better mode overlap with the polymer waveguides, and easier integrated with ohmic thermal heat pattern, in order to tune the resonance frequency of the cavity. The two cavities are designed to have the same resonance frequency, however, due to the fabrication disorder, the resonance frequency of each cavity presents slight difference, and give us the potential to tuning the slowing light in coupled cavities system, which will be discussed in the section 5.3. The dimension of the SU8 waveguide in Fig. 5.1(c) is 3.1 μm wide and 2 μm high. The width is chosen to increase the coupling efficiency between the waveguide mode and the cavity via a large k-space overlap, while the waveguide still operates in a single mode. The oxide layer thickness is set to 110 nm as presented in Fig. 5.1 (d). This process improves the CMOS compatibility of the final device and increases heat transport and allows us to control the coupling coefficient to the polymer bus waveguide.

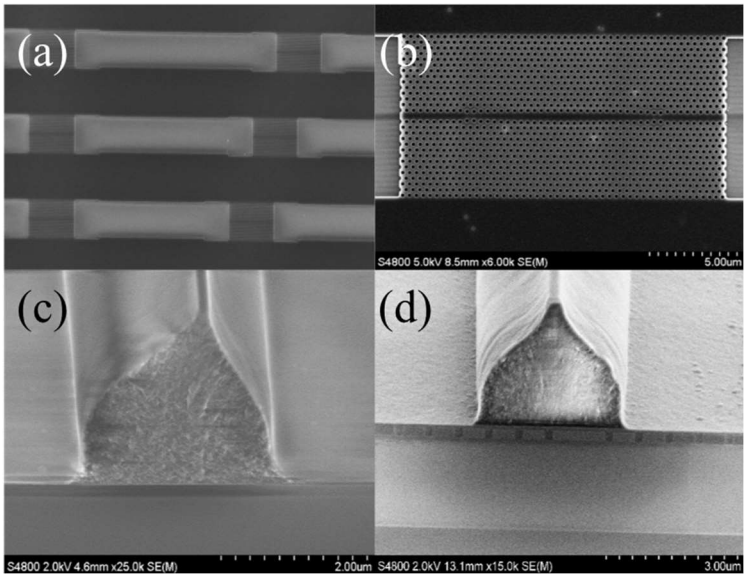

Fig 5.1 SEM schematic images of three different intracavity distances of two coupled DA cavities without an oxide layer covering in (a). Top view of one single DA cavity in (b). A cross-section of SU8 waveguide is shown in (c). A cross-section of SU8 waveguide cleaved above the cavity region is presented in (d). A thin FO_x layer can be seen between the SU8 waveguide and the cavity in (d).

5.2.2 Characterization setup

Here, I provide a brief summary of the optical setups, including optical transmission and group velocity characterization of the system

5.2.2.1 Optical transmission characterization setup

A schematic of the optical transmission characterization setup is shown in Fig. 5.2. An end-fire technique is used to couple light in and out of the device. The equipment used for the passive optical measurement are a computer operated tunable laser and detector, polarization maintaining fibers, collimators, a quarter wave plate, a cube beam splitter, nano positioners, infrared cameras. The setup was designed in such a way that for further active device measurements, complementary components can easily be appended to the setup.

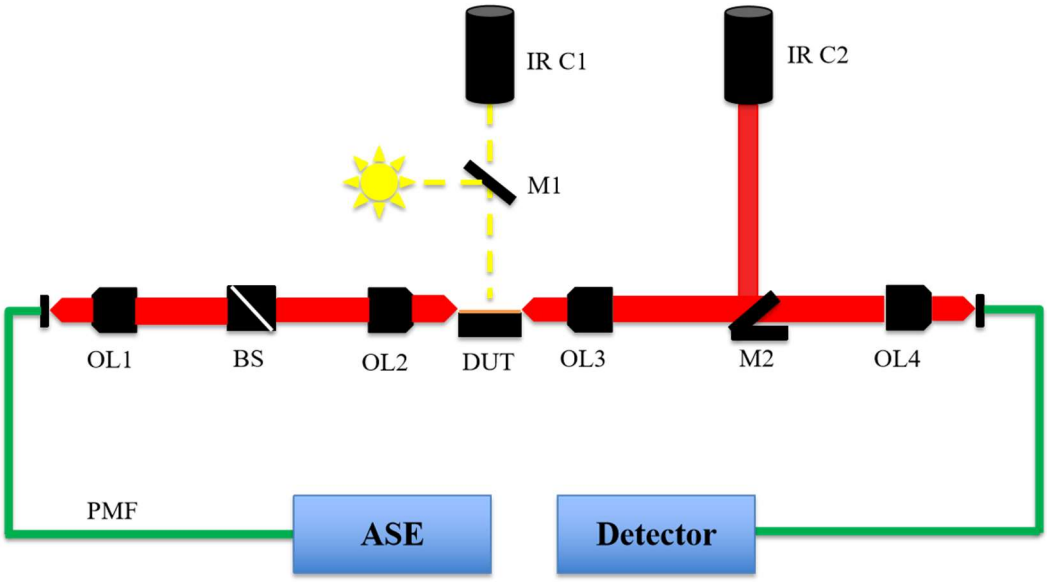

Fig 5.2 Experimental setup for optical transmission measurements. OL: Objective lens, BS: polarization beam splitter, DUT: device under test, M: mirror, IR C: infrared camera, PMF: Polarization maintaining fiber, ASE: amplified spontaneous emission broadband source

In the optical transmission measurement, light from the tunable laser is fed to an objective lens (OL1) through a polarization maintaining fiber (PMF). The collimated output is mainly TM polarized. The polarization of the beam is rotated to TE and any residual TM polarized light is filtered out with a polarization beam splitter (BS). The incoming free space TE polarized light is then focused onto the cleaved facet of one of the waveguides using an objective lens (OL2) and the transmitted light is collected from the other facet of the waveguide with objective lens 3. When the mirror 2 (M2) is flat, the collected light goes straight to the objective lens 4 (OL4) and is collected and measured.

The two infrared cameras are mainly used to facilitate alignment of the collimating lenses with the waveguides on the device. Both cameras have a broad sensitivity range, ranging from the visible to the infrared. This allows us to see both the chip and the infrared light propagating

through the device. The output infrared camera (IR C2) is used to align the output objective lens to the waveguide on the chip (by rotating mirror 2) and to monitor the output beam shape of the waveguide. The tunable laser has a wavelength range from 1520 nm to 1640 nm, with a scanning resolution of 1pm. There are two scanning techniques available, stepped scan and sweep scan. The stepped scan is more accurate but consumes a significant amount of time (up to 12 hours for a full scan); during this time, the mechanical alignment of the setup will drift, resulting in an uncontrolled power variation. In contrast, the sweep scan only takes few minutes with a wavelength resolution of 4 pm. The resolution is sufficient for the measurement and also the fast scanning time avoids any power variation due to mechanical misalignment. Thus, I used the sweep scan for the passive optical characterization.

5.2.2.2 Group delay measurement setup

In this measurement, the optical delay of coupled cavities system has been characterized. There are several different approaches to this measurement, but generally they can be broken up into two basic types. In the first measurement type, an optical pulse is transmitted through the slow light sample and the time delay is measured [166,167]. The other basic principle is to measure the interference of light transmitted through the slow light sample with a reference signal [168-171]. The interference pattern is dependent on the phase difference between the two signals, which in turn depends on the delay between the two signals. Several different interferometer geometries can be used for this measurement. The setup used during this project was an external Mach-Zehnder (MZ) interferometer [171], as shown in Fig. 5.3.

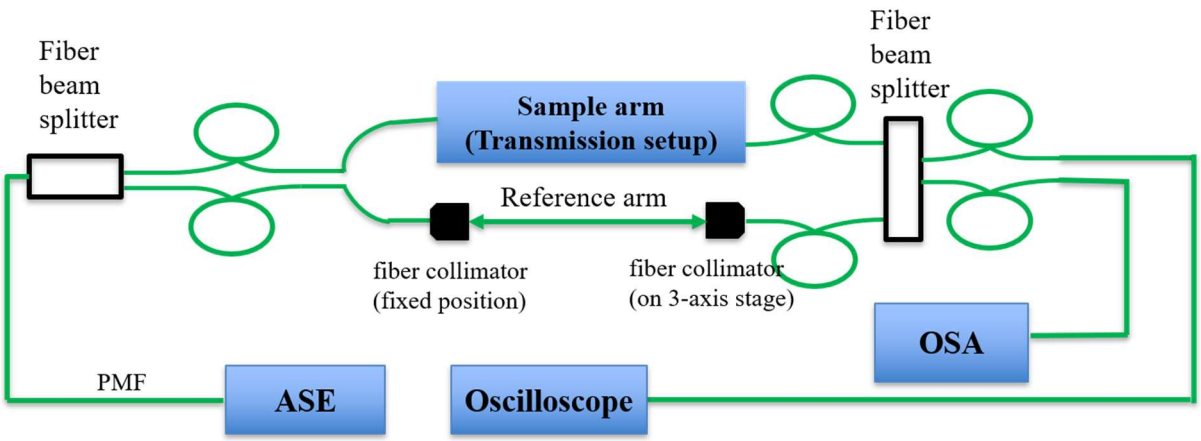

Fig. 5.3 Sketch of the fiber based MZ interferometer used for slow light measurements. The sample arm consists of the same free space optics used for the transmission measurement (Fig 5.3). One of the fiber collimators is mounted on a 3-axis stage for alignment purpose and to allow fine control over the reference arm length. Coarse control off the reference arm length is achieved by shifting the 3-axis stage with the fiber collimator. OSA: optical spectrum analyzer, ASE: amplified spontaneous emission broadband source

In this setup, the optical signal from the source, which can be both CW or pulsed, is separated into two, using 3 dB fiber splitters. The sample is included in one arm (the sample arm) of the MZ interferometer, while an optical delay is included in the other arm (the reference arm). In our implementation, the optical delay is a free space transmission of variable length.

The signals are recombined using a second 3db fiber splitter and the optical signal is then detected by OSA. Before taking the measurement, the delay of the reference arm is adjusted such that its optical length is just shorter than the sample arm. Therefore, after introducing slow light device, the phase difference between the two signals increases, with the sign of the phase difference remaining constant, simplify the calculation of the group velocity. For each device three spectra are measured, one for each arm of the MZ individually and one of the interference patterns. Those three spectra are corresponding to the optical path difference due to the coupled cavities slow light effect, the optical path difference due to the access waveguides and the

physical length of the free space region in two arms. In order to separate the first component from the other two, the measurement is also performed on a photonic wire on the same chip and the delay extracted from this measurement is subtracted from the total delay for the PhC measurement. The resultant optical path difference is due the photonic crystal waveguide. Then, I can get the expression of the interferogarm [171],

$$I(\omega) = S(\omega) + R(\omega) + \sqrt{S(\omega)R(\omega)}\{exp[\, i\Phi(\omega) - i\omega\tau] + c.c\} \qquad 5.1$$

Where S(ω) and R(ω) are the spectral amplitude of the sample arm and the reference arm, respectively. The delay line of τ is chosen to increase the contrast of the delay between the sample arm and reference arm, and thus decrease the fringe spacing. The information of propagation properties is entirely contained in the phase difference term $\Phi = \emptyset_s - \emptyset_R$. The latter is extracted by calculating the Fourier transform of the interferogram with the corresponding frequency. Thus, the difference group delay between the two arms in the MZI is obtained by differentiating $\Phi(\omega) - \omega\tau$. By subtracting other optical components' (including the delay line) contribution, I can get the group delay of the sample arm. An example of measurements result is shown in Fig 5.4.

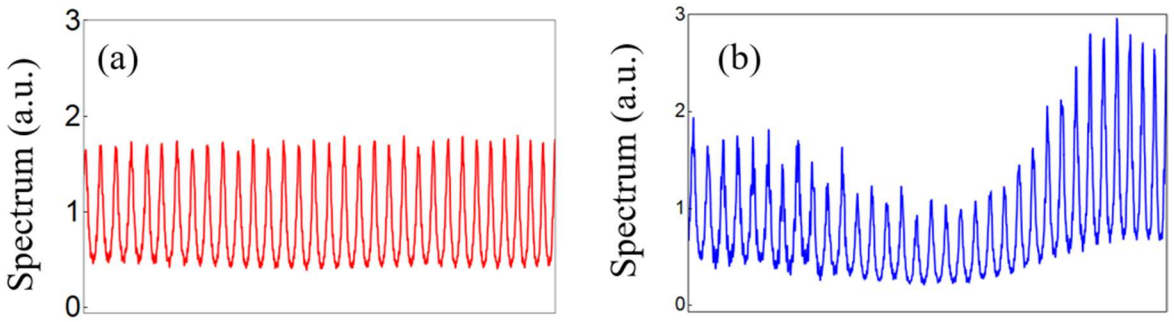

Fig 5.4 Spectra of the MZI output measured for (a) the reference arm (a blank ridge waveguide), and (b) the sample arm (a PhC waveguide).

5.2.3 Optical characterization

The normalized transmission spectrums of three different separations coupled cavities configuration have been presented in Fig 5.5. As been discussed in Section 4.3.1, the different propagation length leads to different phase shift between two coupled cavities. Thus, three different round trip phases are presented respectively, corresponding to three different separation, varying from 20 μm, 50 μm to 75 μm. In the case of Fig 5.5 (a), the phase difference between two coupled cavities is $n\pi$ (n is an integer) and indicates a strong EIT-like transmission peak appears. Then when the phase difference between two coupled cavities is tuned, the EIT-like transmission peak decay and vanish in Fig 5.5 (b) and Fig 5.5 (c), respectively.

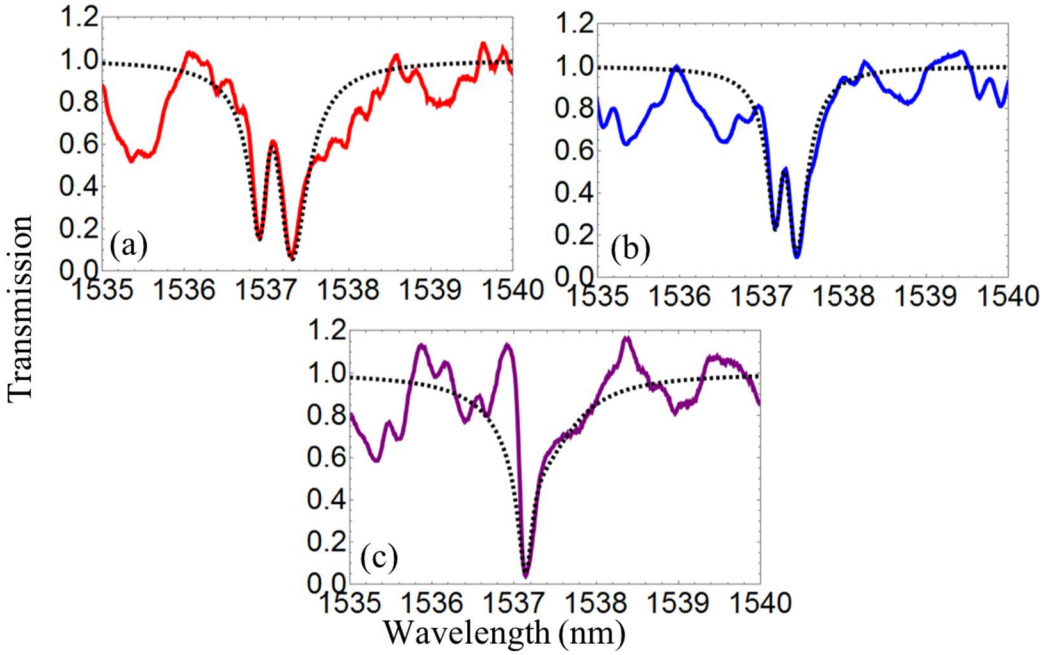

Fig 5.5 Experimental transmission spectra (solid lines) and theoretical fits (dashed lines), for varying separations (from 25 μm, 50 μm to 75 μm) between the two coupled cavities in (a)−(c), respectively.

Based on Eq. 4.24 in the Chapter 4, all figures are theoretical fitted using the same set of Q-factors with cavities A and B displaying an intrinsic Q-factor of 14000 and 16000, respectively, and the Q-factor of the cavity coupling with the waveguide is 6500 and 7600, respectively, as dashed lines shown in Fig 5.4. The resonance wavelength of each cavity is shown in Table 5.1

The separations between two cavities (μm)	λ_a (nm)	λ_b (nm)	$\delta = \lvert\lambda_a - \lambda_b\rvert$ (nm)	Phase difference ($n * \pi$)
25	1536.92	1537.31	0.39	1.8
50	1537.17	1537.42	0.25	2
75	1537.12	1537.31	0.19	1.2

Table 5.1 Cavities properties and phase difference between two coupled cavities

In Fig 5.6, Experimental group delay spectra with theoretical fitting result are presented, corresponding to the three different separations between the two coupled photonic crystal cavities, respectively. Fig 5.6 (a) shows a dramatic group delay of 175 ps at the EIT-like transmission peak. Due to fabrication deviations, the resonance of each cavities cannot match exactly the designed values. Thus, it gives different resonance difference (δ) in those different propagation length configurations, as shown in Table 5.1. However, it offers us to check the relationship between the delay and the resonance difference. As has been discussed in the section 4.3.1, when resonance difference between two coupled cavities become smaller, the bandwidth of the middle band reduces, which leads a bigger group delay in the system. Thus, Fig 5.6 (b) shows bigger group delay of 200 ps at the EIT-like transmission peak with a smaller difference of the resonance frequency between two coupled cavities, compared with the 25 μm

propagation length configuration. In Fig 5.6 (c), the EIT analog has not been realized between two coupled cavities, resulting low group delay of 40 ps in the system.

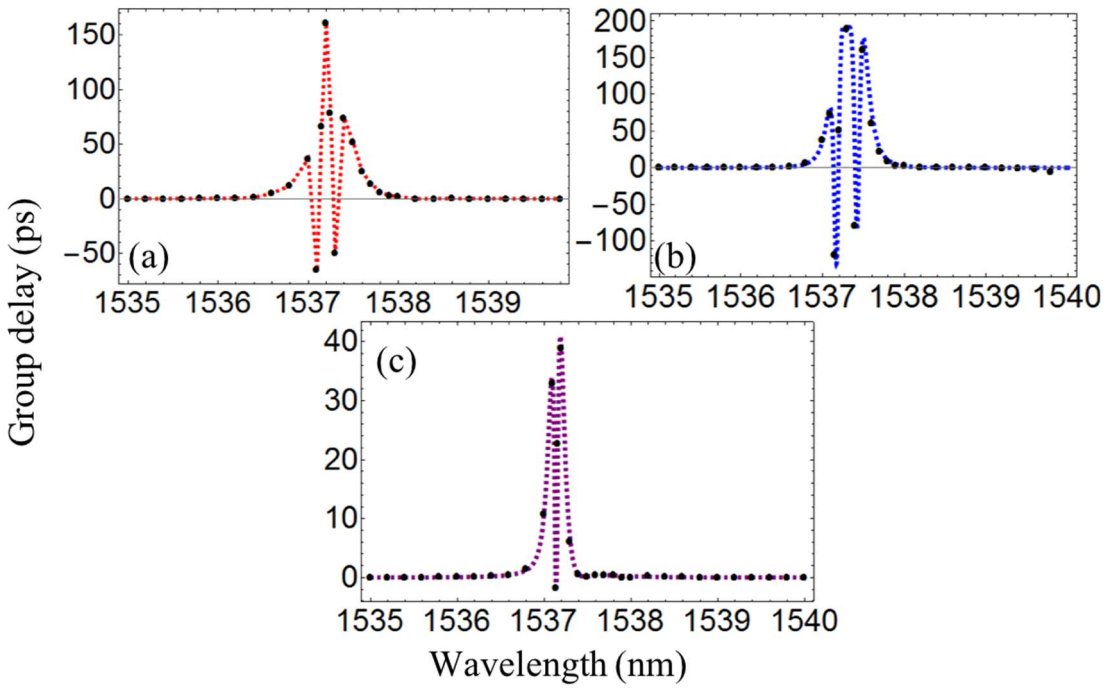

Fig 5.6 Experimental group delay spectra (solid lines) and theoretical fits (dashed lines), for varying separations (from left to right: 25 μm, 50 μm, and 75 μm) between the two coupled cavities in (a)−(c)

When the optical analog of EIT occurs in the two coupled cavities system, images of the light emitted from the coupled cavities regions have been collected by the infrared camera looking from above and presented in Fig 5.7. When the frequency of the input laser pulse set as ω_a as shown in Fig. 5.7 (a), the cavity A has been excited, and the light has been mainly storage in the cavity, indicates there is low transmittance in the system. When the frequency of the input laser pulse tuned is to the EIT resonance in Fig 5.7 (b) and (c), the light is strongly confined between two coupled cavities and the waveguide. The system shows a high transmission at

those frequency regions, similar to EIT system. By changing the frequency of the input laser to the resonance of the cavity B, the light is stored in the cavity as shown in Fig 5.7 (d).

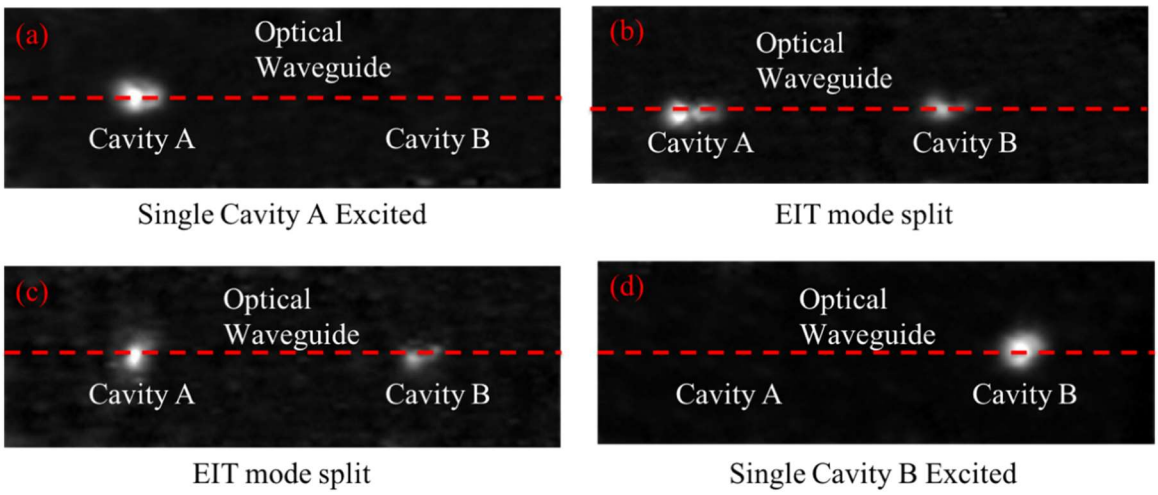

Fig 5.7 Top-collected radiation images of the light emitted from the cavity region have been illustrated in (a)-(d).

In conclusion, the group delay of the two coupled cavities exceed the single pass delay of the waveguide sections and the cavities by a factor of 10, indicating that the resonators interfere, producing a strong EIT-analog effect. The system exhibiting a 200 ps delay has an on-EIT-peak transmission of 0.5, corresponding to a 3 dB loss for 200 ps delay and, hence, an optical loss of only 15 dB/ns. the round-trip phase is detuned from 2 $n\pi$ (370 π in this case), resulting in a much weaker EIT peak and, consequently, a reduced group delay of only 40 ps.

5.3 Dynamic delay tuning through all optical analog to EIT in coupled photonic crystal cavities

In this section, I use thermal-optical tuning to achieve ideal resonance frequency separation of two coupled photonics crystal cavities to reach maximum group delay of optical analog EIT system.

5.3.1 Design and fabrication

5.3.1.1 Design considerations

Due to the fabrication disorder, I cannot achieve two exactly same photonic crystal cavities. Thus, in this section, I will study resonance modulation to achieve dynamically tuning of the delay in the optical analog to EIT based on coupled photonic crystal cavities. Here, I will discuss serval general ways to realize the resonance modulation of a photonics crystal cavity. For a perturbation of sufficiently small magnitude, the amount of red-shift or blue-shift is proportional to the change in refractive index:

$$\frac{\Delta\lambda}{\lambda_0} = \frac{\Delta n}{n}$$

Where n is the average refractive index experienced by the optical mode and λ_0 is the resonance wavelength of the cavity. $\Delta\lambda$ is the change in resonance wavelength due to a refractive index change of Δn. There are serval ways to achieve modulation in the refractive index of silicon structure. One is by applying an electric field to the material to either change the real part of the refractive index [172, 173], which is called electro-refraction, or changing the imaginary part of the refractive index, which is electro-absorption. Another way of achieving refractive index modulation is the free carrier plasma dispersion effect [174-179].

This effect arises from the change in absorption caused by the change in free carrier concentration. The change in absorption alters the imaginary part of the refractive index of the material and, as a result, it affects the real part of the refractive index, according to the Kramers-Kronig relationship. Conventionally, the free carrier plasma effect is employed in silicon by adding pn or pin junctions into the device. For applying the voltage, either excess carriers are depleted (in reverse bias condition) from the junction or injected into the junction (in forward bias condition), which causes an increase or decrease in the refractive index of the silicon in the junction. Refractive index modulation in silicon can also be achieved by the thermal-optic effect, where the refractive index of the material changes with the temperature [180-182]. With the thermal-optic coefficient ($dn/dt = 1.86 \times 10^{-4}/\mathrm{K}$) and high thermal conductivity (156 W/mK) of silicon makes the case that silicon is suited to moderate speed, low power modulation [183, 184]. Thus, in order to realise thermal-optical modulation is a coupled cavities system with thermal-optical tuning patterns is designed based on photonic crystal cavities vertical coupling to a SU8 waveguide. The SEM images of coupled photonic crystal cavities with thermal-heating patterns are shown in Fig 5.8. The two photonics crystal cavities are designed the same as the photonics crystal cavities in Section 5.2. To achieve a good thermal conductivity between the PhC cavity region and thermal heating area, the gap between those two regions is chosen to be 1 μm and the area of thermal heating pattern is set as 300 μm $\times$ 200 μm. I use Chromium and Nickel as the materials of the thermal heat pattern. Both of them have a good thermal conductivity at 90 $W/(m \cdot K)$ and are easily integrated with semiconductor. The thickness of chromium is set to 20 nm as a transit layer between the oxide layer and the metal. The thickness of nickel is set to 250 nm, which can provide a good thermal conductivity and measurement tolerance.

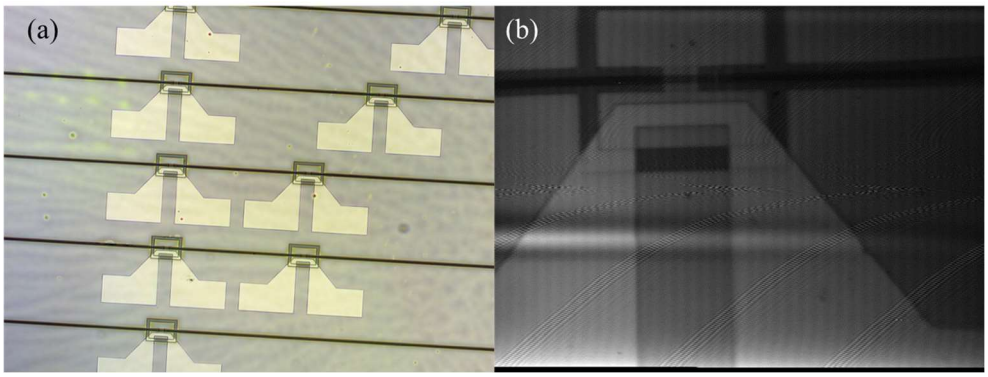

Fig 5.8 Scanning electron microscope images of the fabricated structures. (a) Plan-view of different distance between two coupled DA photonic crystal cavities with ohmic-heat pattern. The two cavities are named as Cavity A and Cavity B, in the order from left. (b) Close look of ohmic heat pattern next to a DA photonic crystal cavity.

5.3.2 Characterization setup

For the resonance modulation setup, I have added a power source meter and a pair of needle probes on SUSS Microtes PH100 probe positioners to the existing optical setups in the section 5.2.2. The schematic of the setup for the resonance modulation measurement is shown in Fig 5.9. When the voltage is applied, a current flow passes through in the ohmic pattern and an amount of heat is generated around the metal pattern. Thus, the temperature around the photonic crystal cavities region is changed leading to the refractive index changing. The phase of the tuned cavity will be changed due to the temperature changing. The phase of the propagation light in the polymer waveguide is not changed, due to the large distance gap between the ohmic pattern and the polymer bus waveguide.

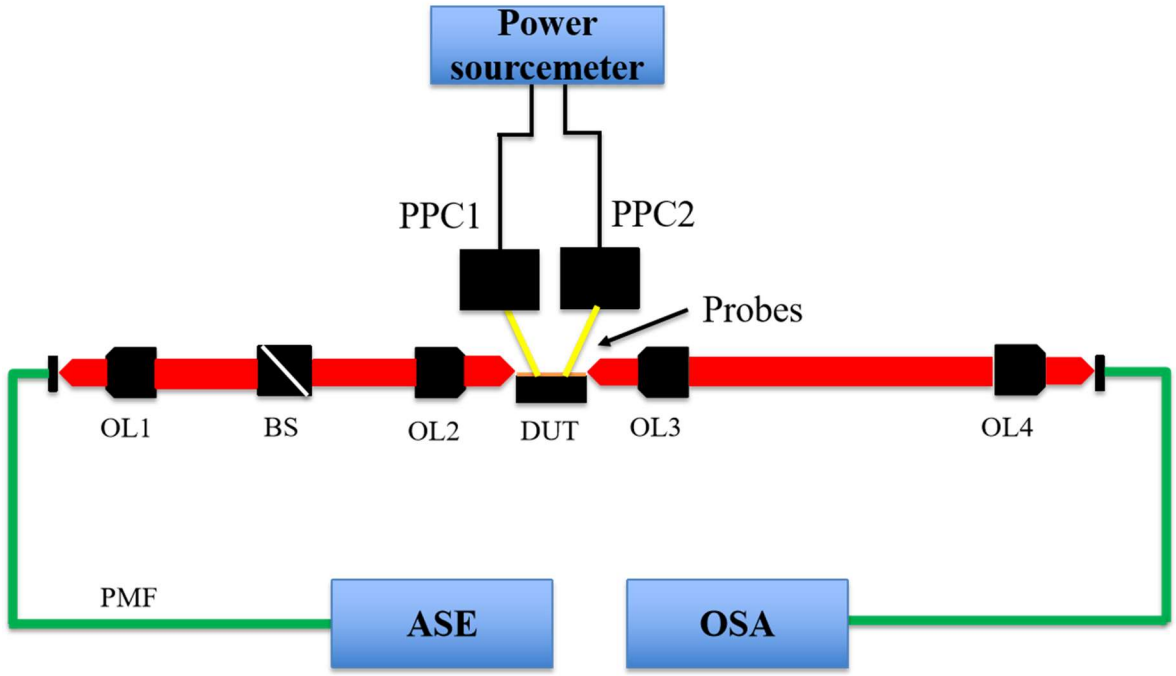

Fig 5.9 Experimental setup for the characterization of the tunable resonant reflector devices. OL: Objective lens, BS: polarization beam splitter, DUT: device under test, PMF: Polarization maintaining fiber, OSA: optical spectrum analyzer, PPC 1-2: power position controllers, ASE: amplified spontaneous emission broadband source.

5.3.3 Optical characterization

The normalized transmission spectrum with resonance tuning is presented in Fig 5.10. The EIT-like transmission spectrum at the initial state (0 mw power) is presented in Fig 5.10(a). The resonance of the cavity B is slightly blue shift away from the ideal detuning. Due to the positive thermos-optic coefficient of silicon, I can just red shift the cavity's resonance. Thus, I tune the cavity B and keep the cavity A constant. The cavities' parameters are listed in Table 5.2. As the electrical power is applied the resonance of the cavity B is red-shifted, the EIT-like peak narrows as shown in Fig 5.10 (b). As the resonance of the cavity B is increased further, leading to an increasing frequency detuning away from the ideal position, the EIT-peak broadens again, and the delay is reduced.

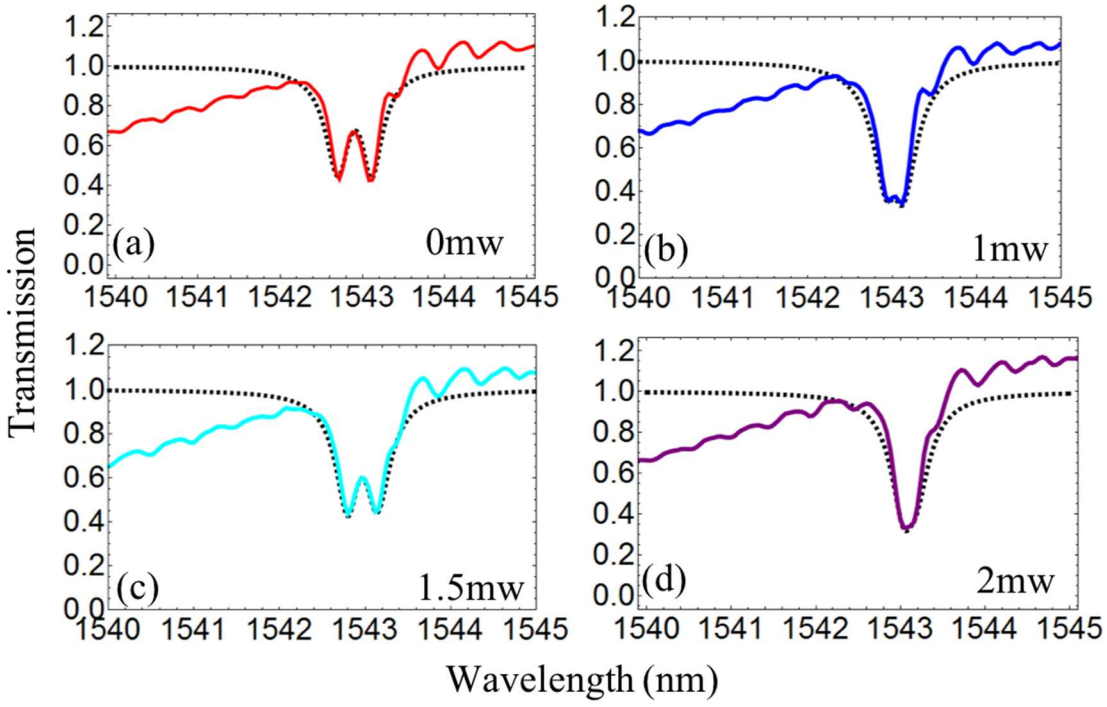

Fig 5.10 Experimental transmission spectra (solid lines) and theoretical fits (dashed lines) for different tuning power at 0 mw, 1 mw, 1.5 mw and 2 mw in the two coupled photonics crystal cavities system in (a)−(d), respectively.

Heat Power (mw)	Cavity A λ_a (nm)	Cavity A λ_b (nm)	Resonance shift of Cavity A δ_a (nm)	Resonance shift of Cavity B δ_b (nm)
0	1542.825	1543.108	0	0
1	1542.830	1543.128	0.005	0.01
1.5	1542.829	1543.160	0.004	0.052
2	1542.827	1543.235	0.002	0.127

Table 5.2 Cavity resonance frequencies at thermal heating tuning

All figures are theoretical fitted using the same set of Q-factors (with cavities A and B displaying an intrinsic Q-factor of 14000 and 16000, respectively, and a coupling Q-factor to

the waveguide of 6500 and 7600, respectively), based on Eq. 4.24 in the Chapter 4. Because thermo-optic tuning does not introduce optical loss and the frequency shift is relatively small, tuning therefore does not alter the characteristics of the transmission line shape of an individual cavity by itself. Therefore, the change in the line shape (and group delay) of the coupled cavities system comes almost entirely from the changing phase shift experienced upon reflection from the tuned cavity. In the case at the initial state (0 mw), the system shows a relatively broad transmission window, with a moderate group delay (100~150 ps), as shown in Fig. 5.11 (a). By applying thermal tuning of cavity B with 1 mw power, as shown in Fig 5.11 (b), the coupled cavities reach the ideal frequency separation giving a large group delay of around 300 ps. The resonance wavelength of Cavity B has shifted 0.01 nm, and Cavity A has shifted 0.005 nm, as shown in Table 5.2. Due to the finite thermal conductivity of the whole device, the total temperature of the device has been raised. So, the resonance of the Cavity A has slightly shifted, does not keep as the original resonance wavelength. By further increasing the applied power to 1.5 mw and 2 mw of the thermal tuner, the resonance of the cavity B has been detuned away from the ideal resonance wavelength, leading a change of EIT-like peak and a low group delay in the system as in Fig 5.11 (c) and (d).

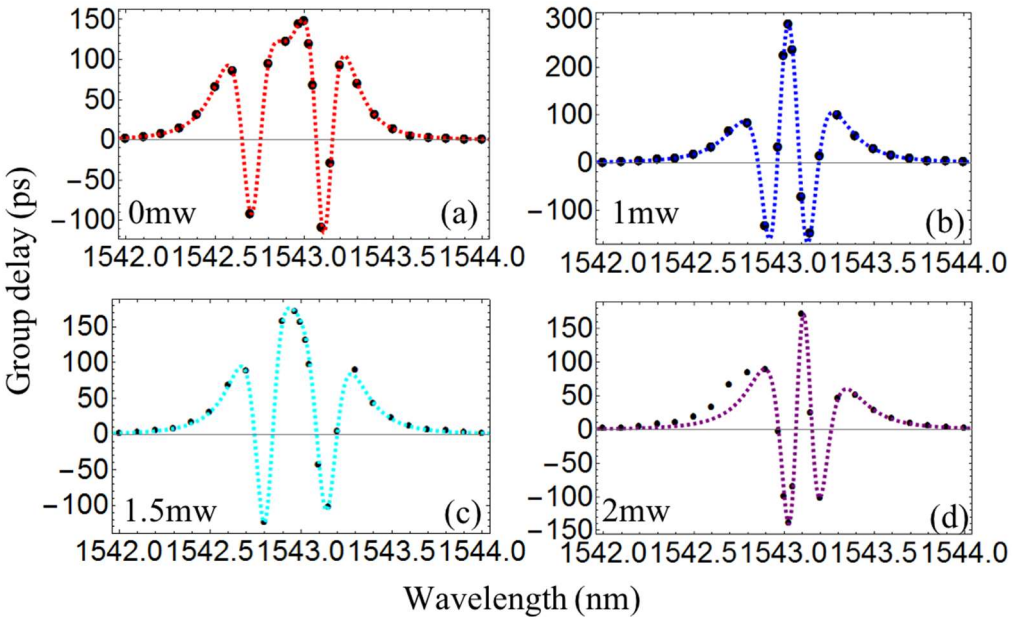

Fig 5.11 (a)−(d) Experimental group delay spectra (solid lines) and theoretical fits (dashed lines), for different tuning power at 0 mw, 1 mw, 1.5 mw and 2 mw applying in the two coupled photonics crystal cavities system.

Thus, I have demonstrated to tune of the EIT-like transmission window and the corresponding group delay. By applying low power tuning, I can achieve a tuning of the delay from 160 ps to 300 ps as shown in Fig. 5.12. After applying thermal tuning to Cavity B, the resonance difference between two coupled cavities decreases, leading to a more ideal analog EIT-transmission. Thus, larger optical delay of the system achieves to 300 ps. Furthermore, when I continue tune the Cavity B, a worse analog EIT-transmission system is presented, and the optical delay of the system reduces to 160 ps. Besides, through the use of a low index polymer waveguide connecting the silicon PhC cavities, I can dramatically outperform pure silicon photonics devices in respect to the propagation loss, while maintaining a large delay and useful delay bandwidth product to reach 15 dB/ns.

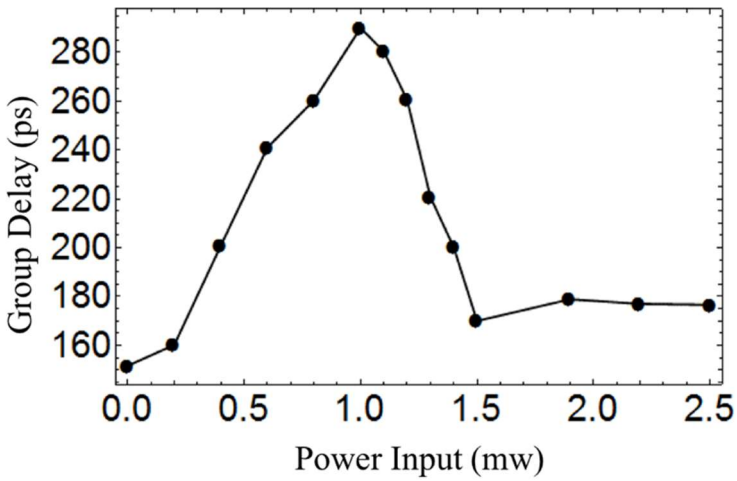

Fig 5.12 Change in group delay vs heater power for the device from Figure 5.12

Finally, a comparison with other delay-bandwidth devices is listed in Table 5.3. Based on the mechanism of slow light effect, I divide slow light products into three major configurations, photonic crystal structure based on optical analog to EIT system, photonic crystal waveguide and ring resonators. As shown in Table 5.3, I have achieved group delay at 350 ps, which is surpassed only by the EIT effect in ultracold atom gas. However, as mentioned in section 2.5.2, the slow light effect in ultracold atom gas [22] needs a large experimental setup and low temperature operation to maintain the atom gas in a quantum condensation state, which is not suitable to practical applications. In addition, by introducing DA oxide cladding cavity into my design, I can achieve a high quality factor photonic crystal cavity used for the vertical coupling system. It provides a high quality factor to 16000, which leads to better optical confine and larger optical delay. Thus, our device has a higher delay-bandwidth and smallest footprint to realize on-chip slow light optical communication, as compared with optical analog EIT system, such as photonic crystal LX cavities system [104], and ring resonators [103]. By using vertical coupling system with a polymer inserting waveguide, I have a lower refractive index contrast compared with in-plane photonic crystal cavities [104], photonic crystal waveguide structures

[185] and coupled ring resonators [69, 103]. Thus, a low propagation loss to 15 dB/ns has been achieved.

Device Type	Optical loss (dB/ns)	Delay (ps)	Bandwidth (GHz)	Delay-bandwidth
Our	15	350	19	6.650
EIT (Atom scale) [22]		$5.3*10^{4}$	$3*10^{-4}$	0.0159
Optical analog EIT (Silicon photonics crystal LX cavities) [104]	85	17	9.55	0.162
Optical analog EIT (Ring resonators) [103]	65	30	32	0.96
Silicon line defect photonics waveguide [185]	40	216.7	12.5	2.7
CROW (ring resonators) [69]	104.54	220	201	44.22

Table 5.3 a comparison of different configurations of delay-bandwidth products.

5.4 Conclusion

In this chapter, I have demonstrated an optical analog EIT-like system by using coupled photonic crystal cavities through a vertical coupling system. By lithograph designing coupled photonic crystal cavities, I can control the coupling coefficients between coupled photonic crystal cavities to reach an ideal analog EIT-like system. By achieving analog EIT-like system, I have observed a larger optical delay to 350 ps. In addition, by adding thermal heating patterns, it provides me to a tuneable optical delay system. By fully detuning from the operating wavelength of coupled photonic crystal cavities, it can obtain the minimum delay of the system, which is the single pass delay through the waveguide. In our design, the distance between two coupled cavities is 350 μm. This length of the waveguide corresponds to a delay of approximately 2 ps. Thus, a full control of two cavities would allow me to obtain a tuning

range from 2 ps to 300 ps. By introducing a polymer inserting waveguide into the vertical coupling system, light is transmitted through the system before undergoing significant scattering which leads to a reduced optical loss to 15 dB/ns. And The use of polymer waveguides also increases the coupling efficiency to optical fibers for the further design. The fiber to fiber loss could be less than 3 dB. As the optical analog EIT-like system is based on a resonant effect (and is linear, reciprocal and time-invariant), it follows that all such coupled resonators systems the device is constrained by the delay-bandwidth limit, which has a maximum value of $\Delta\tau\Delta\omega = 2\pi$. An examination of the experimental data gives a delay-bandwidth product of approximately 6.65, which is close to the theoretical maximum. Thus, this design solves the challenge of optical delay line that can be tuned with low power consumption and gives a large delay with a broad bandwidth in a low propagation loss.

Chapter 6 Conclusion

6.1 Thesis summary

In this thesis, I have introduced and demonstrated a new architecture for optical analog EIT system on a simple and facilitate silicon photonics platform for on-chip optical communication, which can be used in a wide range of applications, ranging from on chip networks or to optical beam steering. The dispersion adapted (DA) photonic crystal cavities have been introduced to achieve a better light confinement and efficient vertical coupling. Additionally, it gives a smaller footprint, lower power consumption and larger free spectral range (FSR), compared with other couplie cavities systems. The core idea for using DA photonic crystal design is to achieve the optical analog to EIT by vertical coupling with a low index polymer waveguide. Therefore, lower propagation losses and coupling loss is realised, compared with other optical analog to EIT systems. Through new vertical coupling technique, I have demonstrated that an extinction ratio of more than 15 dB can be achieved. Different configurations of coupled cavities have been discussed in theoretical and suitable experimental designs have been proposed. Through different thickness of oxide buffer layer between DA photonic crystal cavities and the bus waveguide, precise controlling of the coupling coefficient between the bus waveguide and coupled cavities can be realised. Ultimately, two promising approaches has been proposed and demonstrated to realize the optical analog to EIT in coupled photonic crystal cavities. By lithographic different distances between two coupled photonic crystal cavities, the phase mismatch between two coupled photonic crystal cavities is designed to realize an EIT-like transmission. And, a strong interference between two cavities and the bus waveguide has been directly observed, corresponding with the simulation result in Chapter 4. On the other hand, by adding thermal-optical tuning, the resonance wavelength of two photonic crystal cavities can be modified and a tuning of optical analog to EIT transmission line is demonstrated.

Thermal tuning optical delay is presented which achieves tuning from 160 ps to 300 ps by applying milliwatt power.

6.2 Future directions

In chapter 4, I have theoretically demonstrated different configurations of coupled resonators to achieve slow light. Based on those promising approaches, I have identified potential designs to realize the slow light effect for further practical applications in information communications. In addition, even initial demonstration of optical analog to EIT system in vertical coupled have been present, the scalability and integration with other optical communication components still need to be explored, such as modulators and laser. In this section, I list some of the research plans that will be undertaken in the further.

6.2.1 Optimization of tuning performance

In this thesis, I use thermal-optical tuning pattern to control the resonance wavelength of two coupled resonators to control EIT-like transmission in the system. As we known, the thermal-optical tuning is determined by the heat transfer from ohmic pattern to the silicon. However, ohmic pattern thermal-optical tuning slower processing time, compared with P-N junction tuning. Hence, in future designs, I will add different configurations of P-N junction to realize fast switch tuning, as shown in Fig 6.1. Two diode configurations of P-N junction have been design. In Fig 6.1 (a), a simple P-N diode has been presented, which the depletion region is designed to the cavity axis. In this case, the optical mode overlap with the depletion region is small. An advanced interleaved junction design is show in Fig 6.1 (b). As the interleaved P-N

junctions are crossing the cavity region, a better overlap is achieved between the optical mode and the depletion region. Meanwhile, P-N junctions has been separated with the interleaved region, which allows us to obtain a higher fabrication tolerance and a faster tuning speed, compared with the structure in Fig 6.1 (a). By employing P-N junction in our structure, it allows us to apply a faster switching between different group delay states to realize on-chip all optical information processing. Both red- and blue-shift of the resonance of cavities would provide additional freedom in tuning. A sample with P-N junction design has already been fabricated and measured in Cork institute of Technology. Some initial experiments have already been done, such as measuring the transmission spectra.

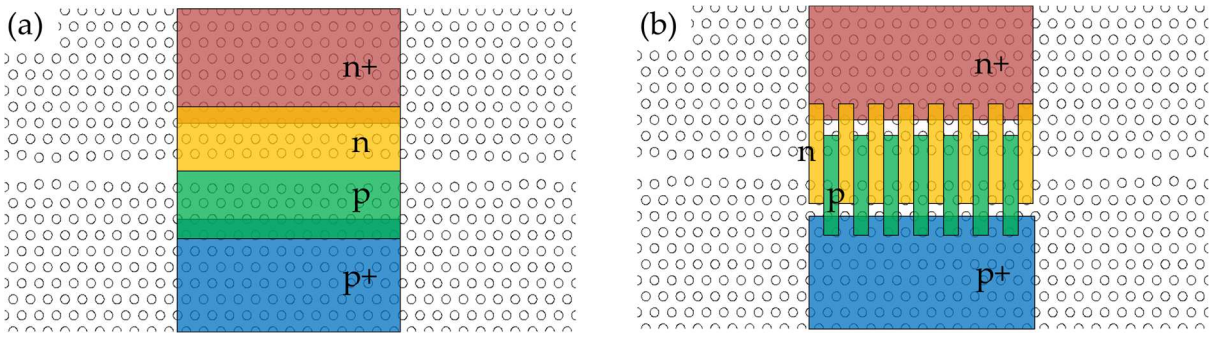

Fig 6.1 Schematic of P-N junctions design for electrical-tuning (a) traditional P-N junction and (b) interleaved P-N junction, respectively

I have demonstrated to lithograph tuning the phase difference to achieve EIT-like transmission spectrum through several different spatial distances between two coupled cavities to. In the next step, I will use thermal tuning on polymer waveguide to achieve the different phase propagation length between two coupled cavities. In this case, I can achieve a direct phase different controlling in a single device. A functional device has already been fabricated.

6.2.2 On-chip all optical processing

Another promising application is to build an optical processing chips combined with a nano-laser [186]. This new architecture of nano-laser, based on photonic crystal cavities, has been demonstrated to achieve external cavity laser, which shares the same fabrication frame in our slow light products, as shown in Fig 6.2. The reflective semiconductor optical amplifier (RSOA) and the photonic crystal cavity acts as a Fabry-Perot cavity and are connected via bus waveguide.

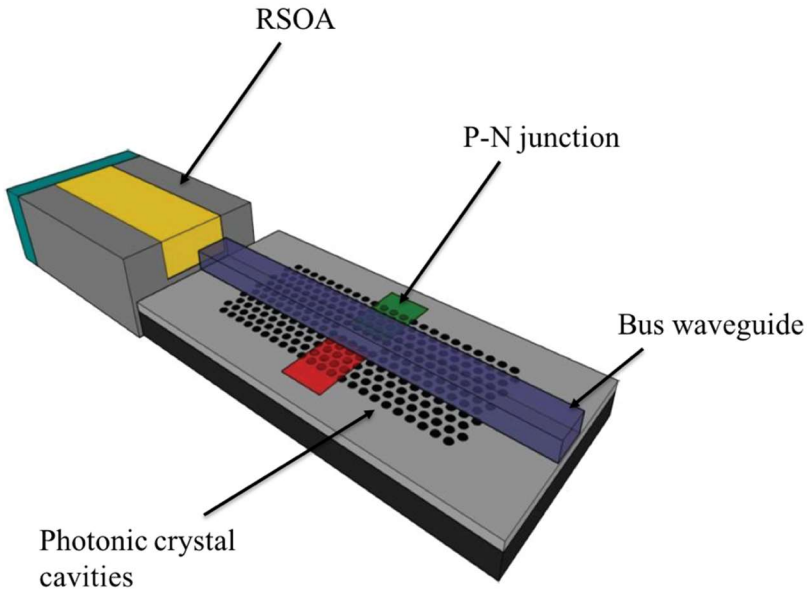

Fig 6.2 Figure reproduced from Ref [186] Schematic of an External cavity laser combining an III-V RSOA and a silicon photonic reflector, which is based on a photonic crystal cavity coupling with a bus waveguide. P-N junction has been applied to achieve electrical tuning for the resonance wavelength.

This device provides milliwatt-level output powers and a side-mode suppression of more than 40 dB. Meanwhile, the output wavelength of the laser can be lithographically controlled through the design of the photonic crystal cavity's resonance wavelength or wavelength tuning by adding thermal or electrical tuning pattern. By engineering designing the output wavelength

of the laser, I can easily match with the wavelength of EIT-like transparency window. By introducing coupled cavities, I can achieve a huge group delay at the EIT-like transmission peak in the system. Thus, it allows us to store the light and address it into different signal states, in which is similar to on and off to signify “0” and “1” states. In this system, I have many flexible parameters to adjust, such as the output wavelength of the laser, and the tuneable group delay of the system. By combining those two components, I can achieve totally on-chip optical information process and open a potential design for quantum electrodynamics applications

Reference

1. Brattain WH. Genesis of the transistor. The Physics Teacher. 1968 Mar;6(3):109-114.

2. Shockley W. The theory of p-n junctions in semiconductors and p-n junction transistors. Bell System Technical Journal. 1949 Jul;28(3):435-489.

3. Moore GE. Cramming more components onto integrated circuits. Proceedings of the IEEE. 1998 Jan;86(1):82-85.

4. Krishnamoorthy AV, Ho R, Zheng X, Schwetman H, Lexau J, Koka P, Li G, Shubin I, Cunningham JE. Computer systems based on silicon photonic interconnects. Proceedings of the IEEE. 2009 Jun 10;97(7):1337-1361.

5. Soref R. The past, present, and future of silicon photonics. IEEE Journal of Selected Topics in Quantum Electronics. 2006 Nov;12(6):1678-1687.

6. Kimerling LC, Ahn D, Apsel AB, Beals M, Carothers D, Chen YK, Conway T, Gill DM, Grove M, Hong CY, Lipson M. Electronic-photonic integrated circuits on the CMOS platform. InSilicon photonics 2006 Mar 1 (Vol. 6125, p. 612502). International Society for Optics and Photonics.

7. Arakawa Y, Nakamura T, Urino Y, Fujita T. Silicon photonics for next generation system integration platform. IEEE Communications Magazine. 2013 Mar 14;51(3):72-77.

8. Charbonnier B, Menezo S, O'Brien P, Lebreton A, Fedeli JM, Bakir BB. Silicon photonics for next generation FDM/FDMA PON. Journal of Optical Communications and Networking. 2012 Sep 1;4(9):A29-37.

9. Soref RA, Lorenzo JP. Single-crystal silicon: a new material for 1.3 and 1.6 μm integrated-optical components. Electronics Letters. 1985 Oct 10;21(21):953-954.

10. Soref RI, Bennett BR. Electrooptical effects in silicon. IEEE Journal of Quantum Electronics. 1987 Jan;23(1):123-129.

11. Liu A, Jones R, Liao L, Samara-Rubio D, Rubin D, Cohen O, Nicolaescu R, Paniccia M. A high-speed silicon optical modulator based on a metal–oxide–semiconductor capacitor. Nature. 2004 Feb;427(6975):615-618.

12. Rong H, Jones R, Liu A, Cohen O, Hak D, Fang A, Paniccia M. A continuous-wave Raman silicon laser. Nature. 2005 Feb;433(7027):725-728.

13. Koch BR, Fang AW, Chang HH, Park H, Kuo YH, Jones R, Cohen O, Radayc O, Paniccia MJ, Bowers JE. A 40 GHz mode locked silicon evanescent laser. In2007 4th IEEE International Conference on Group IV Photonics 2007 Sep 19 (pp. 1-3). IEEE.

14. Liao L, Liu A, Rubin D, Basak JA, Chetrit YA, Nguyen HA, Cohen RA, Izhaky NA, Paniccia MA. 40 Gbit/s silicon optical modulator for high-speed applications. Electronics Letters. 2007 Oct 25;43(22):1196-1197.

15. Narasimha A, Analui B, Liang Y, Sleboda TJ, Gunn C. A Fully Integrated 4× 10Gb/s DWDM Optoelectronic Transceiver in a standard 0.13/spl mu/m CMOS SOI. In2007 IEEE International Solid-State Circuits Conference. Digest of Technical Papers 2007 Feb 11 (pp. 42-586). IEEE.

16. Doerr CR, Buhl LL, Baeyens Y, Aroca R, Chandrasekhar S, Liu X, Chen L, Chen YK. Packaged monolithic silicon 112-Gb/s coherent receiver. IEEE Photonics Technology Letters. 2011 Apr 7;23(12):762-764.

17. Dong P, Xie C, Chen L, Buhl LL, Chen YK. 112-Gb/s monolithic PDM-QPSK modulator in silicon. Optics Express. 2012 Dec 10;20(26):B624-9.

18. Assefa S, Shank S, Green W, Khater M, Kiewra E, Reinholm C, Kamlapurkar S, Rylyakov A, Schow C, Horst F, Pan H. A 90nm CMOS integrated nano-photonics technology for 25Gbps WDM optical communications applications. In2012 International Electron Devices Meeting 2012 Dec 10 (pp. 33-38). IEEE.

19. Willner AE, Zhang B, Zhang L. Slow light, science and applications. CRC Press; 2009; ch.16:321–346.

20. Tucker RS, Ku PC, Chang-Hasnain CJ. Slow-light optical buffers: capabilities and fundamental limitations. Journal of Lightwave Technology. 2005 Dec;23(12):4046-4066.

21. Xia H, Sharpe SJ, Merriam AJ, Harris SE. Electromagnetically induced transparency in atoms with hyperfine structure. Physical Review A. 1997 Nov 1;56(5):R3362.

22. Hau LV, Harris SE, Dutton Z, Behroozi CH. Light speed reduction to 17 metres per second in an ultracold atomic gas. Nature. 1999 Feb;397(6720):594-598.

23. Patnaik AK, Liang JQ, Hakuta K. Slow light propagation in a thin optical fiber via electromagnetically induced transparency. Physical Review A. 2002 Dec 26;66(6):063808.

24. Gonzalez-Herraez M, Song KY, Thévenaz L. Optically controlled slow and fast light in optical fibers using stimulated Brillouin scattering. Applied Physics Letters. 2005 Aug 22;87(8):081113.

25. McMillan JF, Yang X, Panoiu NC, Osgood RM, Wong CW. Enhanced stimulated Raman scattering in slow-light photonic crystal waveguides. Optics Letters. 2006 May 1;31(9):1235-1237.

26. Corcoran B, Monat C, Grillet C, Moss DJ, Eggleton BJ, White TP, O'Faolain L, Krauss TF. Green light emission in silicon through slow-light enhanced third-harmonic generation in photonic-crystal waveguides. Nature Photonics. 2009 Apr;3(4):206.

27. Monat C, Ebnali-Heidari M, Grillet C, Corcoran B, Eggleton BJ, White TP, O'Faolain L, Li J, Krauss TF. Four-wave mixing in slow light engineered silicon photonic crystal waveguides. Optics Express. 2010 Oct 25;18(22):22915-22927.

28. Debnath K, Welna K, Ferrera M, Deasy K, Lidzey DG, O'Faolain L. Highly efficient optical filter based on vertically coupled photonic crystal cavity and bus waveguide. Optics Letters. 2013 Jan 15;38(2):154-156.

29. Ginsberg NS, Garner SR, Hau LV. Coherent control of optical information with matter wave dynamics. Nature. 2007 Feb;445(7128):623-626.

30. Krauss TF. Why do we need slow light?. Nature Photonics. 2008 Aug 1;2(8):448.

31. Baba T. Slow light in photonic crystals. Nature Photonics. 2008 Aug;2(8):465.

32. Sakoda K. Optical properties of photonic crystals. Springer Science & Business Media; 2004 Oct 27.

33. Tucker RS, Ku PC, Chang-Hasnain CJ. Slow-light optical buffers: capabilities and fundamental limitations. Journal of Lightwave Technology. 2005 Dec;23(12):4046-4066.

34. Little BE, Foresi JS, Steinmeyer G, Thoen ER, Chu ST, Haus HA, Ippen EP, Kimerling LC, Greene W. Ultra-compact Si-SiO 2 microring resonator optical channel dropping filters. IEEE Photonics Technology Letters. 1998 Apr;10(4):549-51.

35. Bowden CM, Dowling JP, Everitt HO. Special issue on development and applications of materials exhibiting photonic band gaps. Journal of the Optical Society of America B. 1993;10(2):280-413.

36. Meade RD, Winn JN, Joannopoulos JD. Photonic crystals: Molding the flow of light. Princeton University Press; 1995.

37. Soukoulis CM, editor. Photonic band gap materials. Springer Science & Business Media; 2012 Dec 6.

38. Scherer A, Doll T, Yablonovitch E, Everitt HO, Higgins JA. Guest Editorial: Electromagnetic crystal structures, design, synthesis, and applications. Journal of Lightwave Technology. 1999;17(11):1928-1930.

39. Krauss TF, Baba T. Feature section on photonic crystal structures and applications. IEEE Journal of Quantum Electronics. 2002; 38:724–956.

40. Little BE, Foresi JS, Steinmeyer G, Thoen ER, Chu ST, Haus HA, Ippen EP, Kimerling LC, Greene W. Ultra-compact Si-SiO 2 microring resonator optical channel dropping filters. IEEE Photonics Technology Letters. 1998 Apr;10(4):549-551.

41. Akahane Y, Asano T, Song BS, Noda S. High-Q photonic nanocavity in a two-dimensional photonic crystal. Nature. 2003 Oct;425(6961):944-947.

42. Akahane Y, Asano T, Song BS, Noda S. Fine-tuned high-Q photonic-crystal nanocavity. Optics Express. 2005 Feb 21;13(4):1202-1214.

43. Asano T, Song BS, Noda S. Analysis of the experimental Q factors (~ 1 million) of photonic crystal nanocavities. Optics Express. 2006 Mar 6;14(5):1996-2002.

44. Song BS, Noda S, Asano T, Akahane Y. Ultra-high-Q photonic double-heterostructure nanocavity. Nature Materials. 2005 Mar;4(3):207-210.

45. Tanabe T, Notomi M, Kuramochi E, Shinya A, Taniyama H. Trapping and delaying photons for one nanosecond in an ultrasmall high-Q photonic-crystal nanocavity. Nature Photonics. 2007 Jan;1(1):49-52.

46. Kim GH, Lee YH, Shinya A, Notomi M. Coupling of small, low-loss hexapole mode with photonic crystal slab waveguide mode. Optics Express. 2004 Dec 27;12(26):6624-6631.

47. Coccioli R, Boroditsky M, Kim KW, Rahmat-Samii Y, Yablonovitch E. Smallest possible electromagnetic mode volume in a dielectric cavity. IEE Proceedings-Optoelectronics. 1998 Dec 1;145(6):391-397.

48. Zhang Z, Qiu M. Small-volume waveguide-section high Q microcavities in 2D photonic crystal slabs. Optics Express. 2004 Aug 23;12(17):3988-3995.

49. Baba T, Fukaya N, Yonekura J. Observation of light propagation in photonic crystal optical waveguides with bends. Electronics Letters. 1999 Apr 15;35(8):654-655.

50. Lončar M, Nedeljković D, Doll T, Vučković J, Scherer A, Pearsall TP. Waveguiding in planar photonic crystals. Applied Physics Letters. 2000 Sept 25;77(13):1937-1939.

51. Smith CJ, Benisty H, Olivier S, Rattier M, Weisbuch C, Krauss TF, De La Rue RM, Houdré R, Oesterle U. Low-loss channel waveguides with two-dimensional photonic crystal boundaries. Applied Physics Letters. 2000 Oct 30;77(18):2813-2815.

52. Noda S, Chutinan A, Imada M. Trapping and emission of photons by a single defect in a photonic bandgap structure. Nature. 2000 Oct;407(6804):608-610.

53. Notomi M, Shinya A, Yamada K, Takahashi J, Takahashi C, Yokohama I. Singlemode transmission within photonic bandgap of width-varied single-line-defect photonic crystal waveguides on SOI substrates. Electronics Letters. 2001 Mar 1;37(5):293-295.

54. Baba T, Motegi A, Iwai T, Fukaya N, Watanabe Y, Sakai A. Light propagation characteristics of straight single-line-defect waveguides in photonic crystal slabs fabricated into a silicon-on-insulator substrate. IEEE Journal of Quantum Electronics. 2002 Aug 7;38(7):743-752.

55. Sugimoto Y, Tanaka Y, Ikeda N, Nakamura Y, Asakawa K, Inoue K. Low propagation loss of 0.76 dB/mm in GaAs-based single-line-defect two-dimensional photonic crystal slab waveguides up to 1 cm in length. Optics Express. 2004 Mar 22;12(6):1090-1096.

56. Notomi M, Shinya A, Mitsugi S, Kuramochi E, Ryu HY. Waveguides, resonators and their coupled elements in photonic crystal slabs. Optics Express. 2004 Apr 19;12(8):1551-1561.

57. Bogaerts W, Baets R, Dumon P, Wiaux V, Beckx S, Taillaert D, Luyssaert B, Van Campenhout J, Bienstman P, Van Thourhout D. Nanophotonic waveguides in silicon-on-insulator fabricated with CMOS technology. Journal of Lightwave Technology. 2005 Jan 10;23(1):401-412.

58. Dulkeith E, McNab SJ, Vlasov YA. Mapping the optical properties of slab-type two-dimensional photonic crystal waveguides. Physical Review B. 2005 Sep 1;72(11):115102.

59 Kuramochi E, Notomi M, Hughes S, Shinya A, Watanabe T, Ramunno L. Disorder-induced scattering loss of line-defect waveguides in photonic crystal slabs. Physical Review B. 2005 Oct 31;72(16):161318.

60. Hamachi Y, Kubo S, Baba T. Low dispersion slow light and nonlinearity enhancement in lattice-shifted photonic crystal waveguide. In2008 Conference on Lasers and Electro-Optics and 2008 Conference on Quantum Electronics and Laser Science 2008 May 4 (pp. 1-2). IEEE.

61. Yariv A, Xu Y, Lee RK, Scherer A. Coupled-resonator optical waveguide:? a proposal and analysis. Optics Letters. 1999 Jun 1;24(11):711-713.

62. Olivier S, Smith C, Rattier M, Benisty H, Weisbuch C, Krauss T, Houdre R, Oesterle U. Miniband transmission in a photonic crystal coupled-resonator optical waveguide. Optics Letters. 2001 Jul 1;26(13):1019-1021.

63. Hosomi K, Katsuyama T. A dispersion compensator using coupled defects in a photonic crystal. IEEE journal of Quantum Electronics. 2002 Aug 7;38(7):825-829.

64. Martínez A, García A, Sanchis P, Martí J. Group velocity and dispersion model of coupled-cavity waveguides in photonic crystals. Journal of the Optical Society of America A. 2003 Jan 1;20(1):147-50.

65. Notomi M, Kuramochi E, Tanabe T. Large-scale arrays of ultrahigh-Q coupled nanocavities. Nature Photonics. 2008 Dec;2(12):741.

66. Fukamachi T, Hosomi K, Katsuyama T, Arakawa Y. Group-delay properties of coupled-defect structures in photonic crystals. Japanese Journal of Applied Physics. 2004 Mar 12;43(4A):L449.

67. Khurgin JB. Expanding the bandwidth of slow-light photonic devices based on coupled resonators. Optics Letters. 2005 Mar 1;30(5):513-515.

68. Poon JK, Zhu L, DeRose GA, Yariv A. Transmission and group delay of microring coupled-resonator optical waveguides. Optics Letters. 2006 Feb 15;31(4):456-458.

69. Xia F, Sekaric L, Vlasov Y. Ultracompact optical buffers on a silicon chip. Nature Photonics. 2007 Jan;1(1):65.

70. Kuramochi E, Tanabe T, Taniyama H, Kato M, Notomi M. Observation of heavy photon state in ultrahigh-Q photonic crystal coupled resonator chain. In2007 Quantum Electronics and Laser Science Conference 2007 May 6 (pp. 1-2). IEEE.

71. Letartre X, Seassal C, Grillet C, Rojo-Romeo P, Viktorovitch P, Le Vassor d'Yerville M, Cassagne D, Jouanin C. Group velocity and propagation losses measurement in a single-line photonic-crystal waveguide on InP membranes. Applied Physics Letters. 2001 Oct 8;79(15):2312-2314.

72. Notomi M, Yamada K, Shinya A, Takahashi J, Takahashi C, Yokohama I. Extremely large group-velocity dispersion of line-defect waveguides in photonic crystal slabs. Physical Review Letters. 2001 Nov 30;87(25):253902.

73. Inoue K, Kawai N, Sugimoto Y, Carlsson N, Ikeda N, Asakawa K. Observation of small group velocity in two-dimensional AlGaAs-based photonic crystal slabs. Physical Review B. 2002 Mar 12;65(12):121308.

74. Asano T, Kiyota K, Kumamoto D, Song BS, Noda S. Time-domain measurement of picosecond light-pulse propagation in a two-dimensional photonic crystal-slab waveguide. Applied Physics Letters. 2004 Jun 7;84(23):4690-4692.

75. Baba T. Light localization in line defect photonic crystal waveguides. IEEE Journal of Selected Topics in Quantum Electronics. 2004;10(3):484-491.

76. Vlasov YA, O'boyle M, Hamann HF, McNab SJ. Active control of slow light on a chip with photonic crystal waveguides. Nature. 2005 Nov;438(7064):65-69.

77. Gersen H, Karle TJ, Engelen RJ, Bogaerts W, Korterik JP, Van Hulst NF, Krauss TF, Kuipers L. Real-space observation of ultraslow light in photonic crystal waveguides. Physical Review Letters. 2005 Feb 25;94(7):073903.

78. Finlayson CE, Cattaneo F, Perney NM, Baumberg JJ, Netti MC, Zoorob ME, Charlton MD, Parker GJ. Slow light and chromatic temporal dispersion in photonic crystal waveguides using femtosecond time of flight. Physical Review E. 2006 Jan 30;73(1):016619.

79. Engelen RJ, Sugimoto Y, Watanabe Y, Korterik JP, Ikeda N, van Hulst NF, Asakawa K, Kuipers L. The effect of higher-order dispersion on slow light propagation in photonic crystal waveguides. Optics Express. 2006 Feb 20;14(4):1658-1672.

80. Tanaka Y, Kuwatsuka H, Kawashima H, Ikeda N, Sugimoto Y, Hasama T, Ishikawa H. Effect of third-order dispersion on subpicosecond pulse propagation in photonic-crystal waveguides. Applied Physics Letters. 2006 Sept 25;89(13):131101.

81. Baba T, Mori D. Slow light engineering in photonic crystals. Journal of Physics D: Applied Physics. 2007 Apr 19;40(9):2659.

82. Krauss TF. Slow light in photonic crystal waveguides. Journal of Physics D: Applied Physics. 2007 Apr 19;40(9):2666.

83. Mori D, Baba T. Dispersion-controlled optical group delay device by chirped photonic crystal waveguides. Applied Physics Letters. 2004 Aug 16;85(7):1101-1103.

84. Tucker RS, Ku PC, Chang-Hasnain CJ. Slow-light optical buffers: capabilities and fundamental limitations. Journal of Lightwave Technology. 2005 Dec;23(12):4046-4066.

85. Beggs DM, Rey IH, Kampfrath T, Rotenberg N, Kuipers L, Krauss TF. Ultrafast tunable optical delay line based on indirect photonic transitions. Physical Review Letters. 2012 May 21;108(21):213901.

86. Adachi J, Ishikura N, Sasaki H, Baba T. Wide range tuning of slow light pulse in SOI photonic crystal coupled waveguide via folded chirping. IEEE Journal of Selected Topics in Quantum Electronics. 2009 Oct 13;16(1):192-199.

87. O'Faolain L, Beggs DM, White TP, Kampfrath T, Kuipers K, Krauss TF. Compact optical switches and modulators based on dispersion engineered photonic crystals. IEEE Photonics Journal. 2010 Apr 12;2(3):404-414.

88. Tanabe T, Notomi M, Mitsugi S, Shinya A, Kuramochi E. Fast bistable all-optical switch and memory on a silicon photonic crystal on-chip. Optics Letters. 2005 Oct 1;30(19):2575-2577.

89. Monat C, Corcoran B, Ebnali-Heidari M, Grillet C, Eggleton BJ, White TP, O'Faolain L, Krauss TF. Slow light enhancement of nonlinear effects in silicon engineered photonic crystal waveguides. Optics Express. 2009 Feb 16;17(4):2944-2953.

90. Monat C, De Sterke M, Eggleton BJ. Slow light enhanced nonlinear optics in periodic structures. Journal of Optics. 2010 Sep 24;12(10):104003.

91. Rey IH, Lefevre Y, Schulz SA, Vermeulen N, Krauss TF. Scaling of Raman amplification in realistic slow-light photonic crystal waveguides. Physical Review B. 2011 Jul 20;84(3):035306.

92. Li J, White TP, O'Faolain L, Gomez-Iglesias A, Krauss TF. Systematic design of flat band slow light in photonic crystal waveguides. Optics Express. 2008 Apr 28;16(9):6227-6232.

93. Mori D, Kubo S, Sasaki H, Baba T. Experimental demonstration of wideband dispersion-compensated slow light by a chirped photonic crystal directional coupler. Optics Express. 2007 Apr 30;15(9):5264-5270.

94. Petrov AY, Eich M. Zero dispersion at small group velocities in photonic crystal waveguides. Applied Physics Letters. 2004 Nov 22;85(21):4866-4868.

95. Settle MD, Engelen RJ, Salib M, Michaeli A, Kuipers L, Krauss TF. Flatband slow light in photonic crystals featuring spatial pulse compression and terahertz bandwidth. Optics Express. 2007 Jan 8;15(1):219-226.

96. Frandsen LH, Lavrinenko AV, Fage-Pedersen J, Borel PI. Photonic crystal waveguides with semi-slow light and tailored dispersion properties. Optics Express. 2006 Oct 2;14(20):9444-9450.

97. O'Faolain L, Schulz SA, Beggs DM, White TP, Spasenović M, Kuipers L, Morichetti F, Melloni A, Mazoyer S, Hugonin JP, Lalanne P. Loss engineered slow light waveguides. Optics Express. 2010 Dec 20;18(26):27627-27638.

98. Yanik MF, Fan S. Stopping light all optically. Physical Review Letters. 2004 Feb 25;92(8):083901.

99. Yanik MF, Fan S. Stopping and storing light coherently. Physical Review A. 2005 Jan 5;71(1):013803.

100. Sandhu S, Povinelli ML, Yanik MF, Fan S. Dynamically tuned coupled-resonator delay lines can be nearly dispersion free. Optics Letters. 2006 Jul 1;31(13):1985-1987.

101. Manolatou C, Khan MJ, Fan S, Villeneuve PR, Haus HA, Joannopoulos JD. Coupling of modes analysis of resonant channel add-drop filters. IEEE Journal of Quantum Electronics. 1999 Sept;35(9):1322-1331.

102. Huo Y, Sandhu S, Pan J, Stuhrmann N, Povinelli ML, Kahn JM, Harris JS, Fejer MM, Fan S. Experimental demonstration of two methods for controlling the group delay in a system with photonic-crystal resonators coupled to a waveguide. Optics Letters. 2011 Apr 15;36(8):1482-1484.

103. Xu Q, Sandhu S, Povinelli ML, Shakya J, Fan S, Lipson M. Experimental realization of an on-chip all-optical analogue to electromagnetically induced transparency. Physical Review Letters. 2006 Mar 27;96(12):123901.

104. Yang X, Yu M, Kwong DL, Wong CW. All-optical analog to electromagnetically induced transparency in multiple coupled photonic crystal cavities. Physical Review Letters. 2009 Apr 30;102(17):173902.

105. Welna K, Portalupi SL, Galli M, O'Faolain L, Krauss TF. Novel dispersion-adapted photonic crystal cavity with improved disorder stability. IEEE Journal of Quantum Electronics. 2012 Jun 15;48(9):1177-1183.

106. Debnath K, O'Faolain L, Gardes FY, Steffan AG, Reed GT, Krauss TF. Cascaded modulator architecture for WDM applications. Optics Express. 2012 Dec 3;20(25):27420-27428.

107. Debnath K, Welna K, Ferrera M, Deasy K, Lidzey DG, O'Faolain L. Highly efficient optical filter based on vertically coupled photonic crystal cavity and bus waveguide. Optics Letters. 2013 Jan 15;38(2):154-156.

108. Yablonovitch E. Inhibited spontaneous emission in solid-state physics and electronics. Physical Review Letters. 1987 May 18;58(20):2059-2062.

109. Ohtaka K. Energy band of photons and low-energy photon diffraction. Physical Review B. 1979 May 15;19(10):5057-5067.

110. John S. Strong localization of photons in certain disordered dielectric superlattices. Physical Review Letters. 1987 Jun 8;58(23):2486-2489.

111. Ho KM, Chan CT, Soukoulis CM. Existence of a photonic gap in periodic dielectric structures. Physical Review Letters. 1990 Dec 17;65(25):3152-3155.

112. Krauss TF, Richard M, Brand S. Two-dimensional photonic-bandgap structures operating at near-infrared wavelengths. Nature. 1996 Oct;383(6602):699-702.

113. Lourtioz JM, Benisty H, Berger V, Gerard JM, Maystre D, Tchelnokov A. Photonic Crystals: Towards Nanoscale Photonic Devices. Springer Science & Business Media; 2008 Mar 19.

114. Inoue K, Ohtaka K, editors. Photonic Crystals: Physics, Fabrication and Applications. Springer Science & Business Media; 2004 Jul 20.

115. Shin H, Cox JA, Jarecki R, Starbuck A, Wang Z, Rakich PT. Control of coherent information via on-chip photonic–phononic emitter–receivers. Nature communications. 2015 Mar 5;6:6427.

116. Notomi M. Manipulating light with strongly modulated photonic crystals. Reports on Progress in Physics. 2010 Aug 16;73(9):096501.

117. Miller DA. Device requirements for optical interconnects to silicon chips. Proceedings of the IEEE. 2009 Jun 10;97(7):1166-1185.

118. Bjork G, Yamamoto Y. Analysis of semiconductor microcavity lasers using rate equations. IEEE Journal of Quantum Electronics. 1991 Nov;27(11):2386-2396.

119.Matsuo S, Shinya A, Kakitsuka T, Nozaki K, Segawa T, Sato T, Kawaguchi Y, Notomi M. Ultra-small InGaAsP/InP buried heterostructure photonic crystal laser. In2009 IEEE LEOS Annual Meeting Conference Proceedings 2009 Oct 4 (pp. 453-454). IEEE.

120. Nielsen MA, Chuang IL. Quantum computation and quantum information. Physics Today. 2001 Nov;54:60-62.

121. Englund D, Fattal D, Waks E, Solomon G, Zhang B, Nakaoka T, Arakawa Y, Yamamoto Y, Vučković J. Controlling the spontaneous emission rate of single quantum dots in a two-dimensional photonic crystal. Physical Review Letters. 2005 Jul 1;95(1):013904.

123. Yoshie T, Scherer A, Hendrickson J, Khitrova G, Gibbs HM, Rupper G, Ell C, Shchekin OB, Deppe DG. Vacuum Rabi splitting with a single quantum dot in a photonic crystal nanocavity. Nature. 2004 Nov;432(7014):200-203.

124. Nielsen MA, Chuang IL. Quantum Computation and Quantum Information. Cambridge University Press; 2010 Dec 9.

125. Englund D, Fattal D, Waks E, Solomon G, Zhang B, Nakaoka T, Arakawa Y, Yamamoto Y, Vučković J. Controlling the spontaneous emission rate of single quantum dots in a two-dimensional photonic crystal. Physical Review Letters. 2005 Jul 1;95(1):013904.

126. Chen HJ. Auxiliary-cavity-assisted vacuum Rabi splitting of a semiconductor quantum dot in a photonic crystal nanocavity. Photonics Research. 2018 Dec 1;6(12):1171-1176.

127. Englund D, Faraon A, Fushman I, Stoltz N, Petroff P, Vučković J. Controlling cavity reflectivity with a single quantum dot. Nature. 2007 Dec;450(7171):857-861.

128. Hennessy K, Badolato A, Winger M, Gerace D, Atatüre M, Gulde S, Fält S, Hu EL, Imamoğlu A. Quantum nature of a strongly coupled single quantum dot–cavity system. Nature. 2007 Feb;445(7130):896-899.

[129. Fan S, Villeneuve PR, Joannopoulos JD, Haus HA. Channel drop tunneling through localized states. Physical Review Letters. 1998 Feb 2;80(5):960-963.

130. Takano H, Akahane Y, Asano T, Noda S. In-plane-type channel drop filter in a two-dimensional photonic crystal slab. Applied Physics Letters. 2004 Mar 29;84(13):2226-2228.

131. Shinya A, Mitsugi S, Kuramochi E, Notomi M. Ultrasmall multi-port channel drop filter in two-dimensional photonic crystal on silicon-on-insulator substrate. Optics Express. 2006 Dec 11;14(25):12394-12400.

132. Boyd RW, Gauthier DJ. “Slow” and “fast” light. In: Wolf E editor. Progress in Optics. Elsevier; 2002. 497-530 p.

133. Parra E, Lowell JR. Toward applications of slow light technology. Optics and Photonics News. 2007 Nov 1;18(11):40-45.

134. Ashcroft NW. ND Mermin Solid state physics. Saunders College, Philadelphia. 1976 Jan.

135. Noda S, Chutinan A, Imada M. Trapping and emission of photons by a single defect in a photonic bandgap structure. Nature. 2000 Oct;407(6804):608-610.

136. Song BS, Noda S, Asano T. Photonic devices based on in-plane hetero photonic crystals. Science. 2003 Jun 6;300(5625):1537-1538.

137. Lončar M, Scherer A, Qiu Y. Photonic crystal laser sources for chemical detection. Applied Physics Letters. 2003 Jun 30;82(26):4648-4650.

138. Painter O, Lee RK, Scherer A, Yariv A, O'brien JD, Dapkus PD, Kim I. Two-dimensional photonic band-gap defect mode laser. Science. 1999 Jun 11;284(5421):1819-1821.

139. Michler P, Kiraz A, Becher C, Schoenfeld WV, Petroff PM, Zhang L, Hu E, Imamoglu A. A quantum dot single-photon turnstile device. Science. 2000 Dec 22;290(5500):2282-2285.

140. Johnson SG, Fan S, Mekis A, Joannopoulos JD. Multipole-cancellation mechanism for high-Q cavities in the absence of a complete photonic band gap. Applied Physics Letters. 2001 May 28;78(22):3388-3390.

141. Vučković J, Lončar M, Mabuchi H, Scherer A. Design of photonic crystal microcavities for cavity QED. Physical Review E. 2001 Dec 21;65(1):016608.

142. Vuckovic J, Loncar M, Mabuchi H, Scherer A. Optimization of the Q factor in photonic crystal microcavities. IEEE Journal of Quantum Electronics. 2002 Aug 7;38(7):850-856.

143. Srinivasan K, Painter O. Momentum space design of high-Q photonic crystal optical cavities. Optics Express. 2002 Jul 29;10(15):670-684.

144. Ryu HY, Notomi M, Lee YH. High-quality-factor and small-mode-volume hexapole modes in photonic-crystal-slab nanocavities. Applied Physics Letters. 2003 Nov 24;83(21):4294-4296.

145. Akahane Y, Asano T, Song BS, Noda S. High-Q photonic nanocavity in a two-dimensional photonic crystal. Nature. 2003 Oct;425(6961):944-947.

146. Srinivasan K, Barclay PE, Borselli M, Painter O. Optical-fiber-based measurement of an ultrasmall volume high-Q photonic crystal microcavity. Physical Review B. 2004 Aug 25;70(8):081306.

147. Akahane Y, Asano T, Song BS, Noda S. Fine-tuned high-Q photonic-crystal nanocavity. Optics Express. 2005 Feb 21;13(4):1202-1214.

148. Sauvan C, Lalanne P, Hugonin JP. Slow-wave effect and mode-profile matching in photonic crystal microcavities. Physical Review B. 2005 Apr 27;71(16):165118.

149. Asano T, Noda S. Tuning holes in photonic-crystal nanocavities (reply). Nature. 2004 May;429(6988):1-2.

150. Chutinan A, Noda S. Waveguides and waveguide bends in two-dimensional photonic crystal slabs. Physical Review B. 2000 Aug 15;62(7):4488-4492.

151.Asano T, Song BS, Akahane Y, Noda S. High Q defect cavity using double hetero junction of two-dimensional photonic crystal slab. In 64th Autumn Meeting of the Japan Society of Applied Physics (Fukuoka, Japan). 2004 Sept.

152. Song BS, Noda S, Asano T, Akahane Y. Ultra-high-Q photonic double-heterostructure nanocavity. Nature Materials. 2005 Mar;4(3):207-210.

153. Song BS, Asano T, Akahane Y, Tanaka Y, Noda S. Transmission and reflection characteristics of in-plane hetero-photonic crystals. Applied Physics Letters. 2004 Nov 15;85(20):4591-4593.

154. Tanabe T, Nishiguchi K, Kuramochi E, Notomi M. Low power and fast electro-optic silicon modulator with lateral pin embedded photonic crystal nanocavity. Optics Express. 2009 Dec 7;17(25):22505-22513.

155. Kuramochi E, Notomi M, Mitsugi S, Shinya A, Tanabe T, Watanabe T. Ultrahigh-Q photonic crystal nanocavities realized by the local width modulation of a line defect. Applied physics letters. 2006 Jan 23;88(4):041112.

156. Borselli M, Johnson TJ, Painter O. Measuring the role of surface chemistry in silicon microphotonics. Applied Physics Letters. 2006 Mar 27;88(13):131114.

157. Settle M, Salib M, Michaeli A, Krauss TF. Low loss silicon on insulator photonic crystal waveguides made by 193nm optical lithography. Optics Express. 2006 Mar 20;14(6):2440-2445.

158. White TP, O'Faolain L, Li J, Andreani LC, Krauss TF. Silica-embedded silicon photonic crystal waveguides. Optics Express. 2008 Oct 13;16(21):17076-17081.

159. Jeon SW, Han JK, Song BS, Noda S. Glass-embedded two-dimensional silicon photonic crystal devices with a broad bandwidth waveguide and a high quality nanocavity. Optics Express. 2010 Aug 30;18(18):19361-19366.

160. Song BS, Jeon SW, Noda S. Symmetrically glass-clad photonic crystal nanocavities with ultrahigh quality factors. Optics Letters. 2011 Jan 1;36(1):91-93.

161. Kyser DF, Viswanathan NS. Monte Carlo simulation of spatially distributed beams in electron-beam lithography. Journal of Vacuum Science and Technology. 1975 Nov;12(6):1305-1308.

162. Jansen H, de Boer M, Legtenberg R, Elwenspoek M. The black silicon method: a universal method for determining the parameter setting of a fluorine-based reactive ion etcher in deep silicon trench etching with profile control. Journal of Micromechanics and Microengineering. 1995 Jun;5(2):115-120.

163. Jansen H, Gardeniers H, de Boer M, Elwenspoek M, Fluitman J. A survey on the reactive ion etching of silicon in microtechnology. Journal of Micromechanics and Microengineering. 1996 Mar;6(1):14-28.

164. Goodberlet JG, Hastings JT, Smith HI. Performance of the Raith 150 electron-beam lithography system. Journal of Vacuum Science & Technology B: Microelectronics and Nanometer Structures Processing, Measurement, and Phenomena. 2001 Nov;19(6):2499-503.

165. Li YQ, Xiao M. Observation of quantum interference between dressed states in an electromagnetically induced transparency. Physical Review A. 1995 Jun 1;51(6):4959.

166. Notomi M, Yamada K, Shinya A, Takahashi J, Takahashi C, Yokohama I. Extremely large group-velocity dispersion of line-defect waveguides in photonic crystal slabs. Physical Review Letters. 2001 Nov 30;87(25):253902.

167. Jacobsen RS, Lavrinenko AV, Frandsen LH, Peucheret C, Zsigri B, Moulin G, Fage-Pedersen J, Borel PI. Direct experimental and numerical determination of extremely high group indices in photonic crystal waveguides. Optics Express. 2005 Oct 3;13(20):7861-7871.

168. Tarhan II, Zinkin MP, Watson GH. Interferometric technique for the measurement of photonic band structure in colloidal crystals. Optics Letters. 1995 Jul 15;20(14):1571-1573

169.Galli M, Bajoni D, Marabelli F, Andreani LC, Pavesi L, Pucker G. Photonic bands and group-velocity dispersion in Si/SiO 2 photonic crystals from white-light interferometry. Physical Review B. 2004 Mar 12;69(11):115107.

170. Vlasov YA, O'boyle M, Hamann HF, McNab SJ. Active control of slow light on a chip with photonic crystal waveguides. Nature. 2005 Nov;438(7064):65-69.

171. Gomez-Iglesias A, O'Brien D, O'Faolain L, Miller A, Krauss TF. Direct measurement of the group index of photonic crystal waveguides via Fourier transform spectral interferometry. Applied Physics Letters. 2007 Jun 25;90(26):261107.

172. Soref RA, Bennett BR. Kramers-Kronig analysis of electro-optical switching in silicon. InIntegrated Optical Circuit Engineering IV 1987 Mar 10 (Vol. 704, pp. 32-37). International Society for Optics and Photonics.

173. Soref RI, Bennett BR. Electrooptical effects in silicon. IEEE Journal of Quantum Electronics. 1987 Jan;23(1):123-129.

174. Thomson DJ, Gardes FY, Fedeli JM, Zlatanovic S, Hu Y, Kuo BP, Myslivets E, Alic N, Radic S, Mashanovich GZ, Reed GT. 50-Gb/s silicon optical modulator. IEEE Photonics Technology Letters. 2011 Nov 22;24(4):234-236.

175. Xiao X, Xu H, Li X, Li Z, Chu T, Yu Y, Yu J. High-speed, low-loss silicon Mach–Zehnder modulators with doping optimization. Optics Express. 2013 Feb 25; 21(4): 4116-4125.

176. Tanabe T, Nishiguchi K, Kuramochi E, Notomi M. Low power and fast electro-optic silicon modulator with lateral pin embedded photonic crystal nanocavity. Optics Express. 2009 Dec 7;17(25):22505-22513.

177. Xu Q, Schmidt B, Shakya J, Lipson M. Cascaded silicon micro-ring modulators for WDM optical interconnection. Optics Express. 2006 Oct 2;14(20):9431-94316.

178. Xu H, Xiao X, Li X, Hu Y, Li Z, Chu T, Yu Y, Yu J. High speed silicon Mach-Zehnder modulator based on interleaved PN junctions. Optics Express. 2012 Jul 2;20(14):15093-15099.

179. Xiao X, Xu H, Li X, Hu Y, Xiong K, Li Z, Chu T, Yu Y, Yu J. 25 Gbit/s silicon microring modulator based on misalignment-tolerant interleaved PN junctions. Optics Express. 2012 Jan 30;20(3):2507-2515.

180. Clark SA, Culshaw B, Dawnay EJ, Day IE. Thermo-optic phase modulators in SIMOX material. InIntegrated Optics Devices IV 2000 Mar 24 (Vol. 3936, pp. 16-24). International Society for Optics and Photonics.

181. McLaughlin AJ, Jubber MG, Bonar JR, Aitchison JS, Jacobs-Cook AJ. Design of fast response and low power consumption thermo-optic modulators. In IEE Colloquium on Optoelectronic Integration and Switching (Ref. No: 1997/372) 1997 Nov 13 (pp. 3-1). IET.

182. Moller BA, Jensen L, Laurent-Lund C, Thirstrup C. Silica-waveguide thermooptic phase shifter with low power consumption and low lateral heat diffusion. IEEE Photonics Technology Letters. 1993 Dec;5(12):1415-1418.

183. Cocorullo G, Iodice M, Rendina I. All-silicon Fabry–Perot modulator based on the thermo-optic effect. Optics Letters. 1994 Mar 15;19(6):420-422.

184. Cocorullo G, Iodice M, Rendina I, Sarro PM. Silicon thermooptical micromodulator with 700-kHz-3-dB bandwidth. IEEE Photonics Technology Letters. 1995 Apr;7(4):363-365.

185. Lin CY, Subbaraman H, Hosseini A, Wang AX, Zhu L, Chen RT. Silicon nanomembrane based photonic crystal waveguide array for wavelength-tunable true-time-delay lines. Applied Physics Letters. 2012 Jul 30;101(5):051101.

186. Liles AA, Debnath K, O'Faolain L. Lithographic wavelength control of an external cavity laser with a silicon photonic crystal cavity-based resonant reflector. Optics Letters. 2016 Mar 1;41(5):894-897.